Radio emission of binary stars in the AB Doradus moving group

Memoria presentada para optar al título de Doctor en Física
Rebecca Azulay Romero

Departamento de Astronomía y Astrofísica
Universidad de Valencia

Valencia, 2016

Director:
Dr. José Carlos Guirado Puerta

JOSÉ CARLOS GUIRADO PUERTA, Profesor titular de Astronomía y Astrofísica de la Universidad de Valencia

CERTIFICA:

Que la presente memoria, titulada *Radio emission of binary stars in the AB Doradus moving group*, ha sido realizada en el Departamento de Astronomía y Astrofísica de la Universidad de Valencia por Rebecca Azulay Romero bajo su dirección y constituye su Tesis Doctoral para optar al grado de Doctor en Ciencias Físicas.

Valencia, 7 de abril de 2016

Fdo. José Carlos Guirado Puerta

Acknowledgements

En enero de 2013 empecé el doctorado pocos días después del peor momento de mi vida: el fallecimiento de mi padre. No ha sido un camino fácil, pero la inestimable ayuda de un montón de grandes personas, tanto dentro del ámbito científico como fuera de él, han hecho que esta experiencia haya valido mucho la pena.

En primer lugar, agradecer al grupo de Radioastronomía de la Universidad de Valencia el haberme dado la posibilidad de hacer con ellos esta tesis doctoral. Somos un grupo pequeño, pero muy competente a nivel científico.

Mil gracias a mi director de tesis, José Carlos Guirado, por todo lo que ha hecho por mí, profesionalmente y personalmente, ¡que sé que convivir conmigo día a día no es algo sencillo! Gracias por confiar en mí en todo momento, por guiarme y orientarme cada vez que lo he necesitado, por tu experiencia, por tus consejos y por tu paciencia. Nada de esto hubiese sido posible sin todo lo que me has enseñado y apoyado.

Gracias también a Jon Marcaide, investigador principal del grupo de Radioastronomía, por haberme proporcionado la posibilidad de haber hecho la tesis, así como por sus comentarios y consejos para que las cosas siempre fueran a mejor. Gracias también a aquéllos que estaban cuando yo empecé pero que ya se fueron. Gracias a Eduardo Ros por haberme enseñado tanto sobre Radioastronomía y sobre la vida en general, por haberme abierto las puertas en el Max Planck Institute für Radioastronomie en Bonn, por su eficiencia, por su disponibilidad y por haberme transmitido la idea de que nuestro trabajo puede ser realmente una tarea apasionante. Gracias a Belén Arroyo, por tantas y tantas horas de conversaciones en el despacho, por todas las risas y por haber tenido siempre un momento para escucharme cuando lo he necesitado. Gracias a Iván Martí-Vidal por haberme acogido en el Onsala Space Observatory y por toda su ayuda y colaboración, tanto científica como personal. Y gracias también a Miguel Ángel Pérez-Torres, por su eficacia a la hora de trabajar, por sus consejos y por haberme transmitido una pequeña parte de todo lo que sabe.

Fuera del grupo de Radioastronomía, pero dentro del Departamento de Astronomía y Astrofísica, también quiero agradecer el trabajo y apoyo de muchos compañeros. Aunque más que compañeros, son amigos. Gracias a Álex, Nico Sanchis, Nico De Brie, Jose, Vassili, Tomek, Neus, Héctor y Jesús. Gracias por todas las horas de vuestro tiempo que me habéis dedicado cuando os he buscado toda estresada. Gracias por todas las comidas, las cenas, los cafés, los juegos competitivos y las risas. Todo eso me ha dado fuerzas día tras día para poder continuar. Y gracias también a todos los miembros del Observatorio Astronómico: Fernando, Amelia, Alberto, Juan, Carlos, Lluís, Leo, Lorena, Vicent Martínez, Vicent Peris, Óscar, Miquel, Xusa y Julia. ¡Gracias por tener los descansos del café más divertidos del universo! Y por amar tanto la ciencia, porque gente como vosotros es realmente increíble e imprescindible.

Y qué decir de mis compañeros (y amigos) de la Asociación de Astronomía. Muchísimas gracias a Javi, Ángel, Eva, Susana, Alberto, Roger, Andreu y Kevin por cada salida de observación, por cada ruta de montaña... en definitiva, ¡por cada plan loco y genial a horas intempestivas! Espero que sigan habiendo muchos más. Gracias por haberme hecho pasar ratos inolvidables y por haberme dado la posibilidad de divulgar la astronomía, que es algo sencillamente maravilloso. Gracias también a mis compañeros y amigos del IFIC, David, Fernando, Ramón y Javi por los cafés de cada mañana, necesarios para ponernos al día del mundo y echarnos unas risas. Y gracias también al resto de compañeros con los que cada jueves (cuando las lesiones me lo han permitido) he podido jugar a fútbol ¡y marcar goles!

Las estancias y los congresos a los que he podido asistir durante mi doctorado también me han permitido conocer gente maravillosa que me han transmitido resultados e ideas científicas muy interesantes y me han hecho pasar ratos muy agradables. Muchas gracias a todos ellos y, en especial, a Carolina Mora, Denise Riquelme, Ancor Damas, Luis Esteras, Emilio Romano, Sara Ferrando y a todas las demás grandísimas personas que conocí durante mi estancia en Bonn. Gracias por acogerme desde el principio, por aportarme nuevos conocimientos científicos, por llevarme a escalar, por las barbacoas, por los cumpleaños, por los partidos de fútbol, por los cafés y por los paseos en bici. Gracias a Javier Moldón, Iván Agudo y Gabriele Surcis por asesorarme cuando he ido a ASTRON a reducir mis datos de VLBI y haberme hecho sentir tan cómoda. Gracias a toda la gente del Onsala Space Observatory que hizo que mi estancia allí fuera muy productiva y agradable. Gracias también a Jesús Aceituno por la acogida que me ofreció cuando fui al observatorio de Calar Alto a observar y por su posterior disponibilidad, ¡y no se me olvida que me debes una clase de karate! Y, como no, gracias a Benito Marcote, por toda su ayuda y por todas nuestras conversaciones. Que aunque no trabaje con las estrellas que de verdad importan, le tengo mucho cariño igual.

También quiero agradecer a todas las demás personas que me han acompañado durante todos estos años de doctorado, no a nivel de investigación, pero si a otros niveles que merecen el mismo reconocimiento. Gracias a mis compañeros de voley, a Juanfran (¡el mejor entrenador del universo! y mejor persona), Hada, Claudia, Luca, Darío, Dani, Denis, Diana, Gabi, Mónica, Vanesa y todos los demás. Millones de gracias por cada entrenamiento, por cada partido, por cada cena y por cada abrazo. Uno de los mejores momentos de mi día era, es y seguirá siendo el momento de ir a entrenar. Sois grandísimas personas y os aseguro que me habéis ayudado muchísimo y me habéis hecho pasar ratos realmente increíbles.

Gracias a Sandra y a Cata. Es imposible enumerar aquí todas y cada una de las cosas que habéis hecho por mí. Espero que os quedéis a mi lado siempre. Muchas, muchas, muchas gracias también a Celia y a Iñaki, por su inmensa paciencia, por sus abrazos, por sus consejos, por los juegos frikis, por las cenas y, sobre todo, por ser personas en las que puedo confiar al 100% y por estar siempre ahí las 24 horas del día, los 7 días de la semana. Muchas gracias también a Mar por todos los ratos que hemos pasado juntas y por apoyarme siempre, siempre. Sé que pase lo que pase voy a poder contar contigo y no veas cómo me alegra eso.

Mil millones de gracias a Lorena, la mejor amiga del universo, mi hermanita mayor. Gracias por tu infinita paciencia, por tu eterna comprensión y por tu empatía. Gracias por haberme enseñado tantas cosas, porque a tu lado he ido creciendo mucho como persona. Gracias por todas las noches en tu casa, por todos los gofres y helados, por los paseos por la playa, por los conciertos, por las noches de lluvias de estrellas, por nuestras mil y una conversaciones, por los viajes, por las horas en el despacho, por los consejos, por las sonrisas... Pero, sobre todo, gracias por cuidarme siempre y tener en todo momento un hueco para mí.

Mil millones de gracias también a Miquel, la persona que más me conoce, más incluso que yo misma. Sabes que para nada hubiese yo llegado hasta aquí si no llega a ser por ti. Y sabes lo mucho que me has ayudado en todos y cada uno de los aspectos de mi vida. Gracias por todos los momentos que hemos pasado juntos y por no haberme dejado caer nunca y haberme devuelto las fuerzas cuando yo creía que ya no las tenía. Espero que siempre te mantengas cerca, ¡que así podré seguir copiándome de tus cosas!

E infinitas gracias a Ángel. Infinitas gracias por absolutamente todo. Por estar siempre ahí, por tener tanta paciencia, por cuidarme, por quererme, por comprenderme y por confiar en mí. Gracias por transmitirme tus ganas de luchar y no rendirse nunca, por compartir conmigo tantas cosas y por saber siempre cómo sacarme una sonrisa. Esta recta final a tu lado y con tu ayuda ha sido mucho más bonita, llevadera y sencilla. Muchas gracias de verdad.

Ya acabando, muchas gracias a parte de mi familia. Gracias por haberme dado la estabilidad necesaria para poder seguir adelante. Gracias a mis abuelos, José Luis y Trini, por haberlo hecho absolutamente todo por mí. Gracias por haberme transmitido tanta bondad y cariño. Gracias a mi tía Eva por entenderme y ayudarme en todo momento y por haber sido la persona que me hizo descubrir mi pasión por la astronomía desde muy pequeña. Gracias a mi tía Trini Mari, a mi tío José Luis, a mi tía Marifran, a mi primo Carlos y a Gustavo por haberme apoyado en todo momento. Gracias también a mi tía Marilda, a mi tío Boro y a mis primos Sarah y Ari que, aunque los vea menos, sé que siempre van a estar ahí para apoyarme. Y muchísimas gracias también a mi abuelo Jacob por haberme querido tanto y por haberme enseñado tantas cosas.

Finalmente, gracias a mi madre, Marian Romero, por todo lo que ha hecho y hace por mí. Estos años no han sido nada fáciles, pero he contado con su apoyo incondicional, el cual ha sido fundamental para haber llegado hasta donde estoy ahora. Sé que voy a poder contar con ella en todo momento y que, mientras esté en su mano, nunca me va a faltar absolutamente nada. Y ya para acabar, gracias a mi padre, José Azulay. Ojalá hubiese podido estar aquí para vivir este momento. Sé que estaría muy orgulloso de mí. Sé que yo era lo que él más quería en el mundo. Le echo de menos cada día. Pero él me enseñó que hay que ser fuerte y que hay que tirar para adelante. Una de las últimas cosas que me dijo fue cada vez que mirara una estrella por el telescopio, que me fijara bien, porque él estaría ahí saludándome y mandándome fuerzas para que todo fuera bien. Que no le quepa ni la más mínima duda de que así lo hago.

Abstract

We present a study of the radio emission and kinematics of a sample of stars belonging to the AB Doradus moving group through VLA and VLBI observations. The main aim of our study is to obtain precise estimates of the dynamical mass of young, low-mass stars, which in combination with photometric measurements provide precise benchmarks for calibrating pre-main-sequence (PMS) stellar evolutionary models. Calibration of PMS models appears essential as they are widely used to predict the masses of low mass objects as brown dwarfs and planets. Previous studies show that model predictions are in disagreement with experimental results for masses below 1.2 $M_\odot$. Among the stars included in our study, we emphasize the results obtained in two of them: AB Dor B and HD 160934.

We observed the binary system AB Dor B in three different epochs between 2007 and 2013 with the Australian Long Baseline Array (LBA) at a frequency of 8.4 GHz. We detected, for the first time, compact radio emission from both stars in the binary, AB Dor Ba and AB Dor Bb. This result allowed us to determine the orbital parameters of both the relative and absolute orbits and, consequently, their individual dynamical masses: 0.28±0.05 $M_\odot$ and 0.25±0.05 $M_\odot$, respectively. Comparisons of the dynamical masses with the prediction of PMS evolutionary models show that the models underpredict the dynamical masses of the binary components Ba and Bb by 10−30% and 10−40%, respectively, although they still agree at the 2σ level. Some of the stellar models considered favor an age between 50 and 100 Myr for this system, while others predict older ages. Simultaneously with AB Dor B, we also observed the well-known stellar system AB Dor A, only $9''$ apart and composed by the stars AB Dor A itself and AB Dor C. The new data allowed us to revisit the previously published values of both the orbital parameters and dynamical masses. In particular, we found component masses of 0.894±0.040 $M_\odot$ and 0.090±0.005 $M_\odot$ for AB Dor A and AB Dor C, respectively, that allowed us for comparison with theoretical stellar models. In the case of AB Dor A, the models predict good estimates within the uncertainties, favouring an early age between 35−50 Myr. In the case of AB Dor C, the models derive a mass similar to the dynamical mass and an age between 40 and 120 Myr.

Regarding HD 160934, we observed this system with the European VLBI Network (EVN) at 5 GHz in three different epochs between 2012 and 2014. We showed that the two components of the binary, HD 160934 A and HD 160934 c, display compact radio emission at VLBI scales, providing precise information on the relative and absolute orbits, which were analyzed in combination with previously reported orbital measurements. Revised orbital elements were estimated and individual masses of 0.70±0.07 $M_\odot$ and 0.45±0.04 $M_\odot$ for components A and c, respectively, were determined. Theoretical models predict masses for the component A ~10% lower than our dynamical value; likewise the predictions for the component c are 20−40% lower than our dynamical measurement. The age of the system varies between 40 and 65 Myr depending on models.

Other stars in our sample include EK Dra, LO Peg, and PW And, observed with the EVN at 5 GHz. EK Dra and PW And showed compact radio emission at milliarcsecond scales, meanwhile LO Peg, appeared to be "off" at the time of observations. The scarce number of detections prevented us to obtain estimates of their masses, however, they allowed us to set bounds to their kinematics. Complementary, companion infrared observations of EK Dra has led us to a revision of the orbital parameters of this system.

In summary, our project provides new observational data to calibrate stellar evolutionary models of PMS objects, supporting the evidence that these models tend to underestimate the dynamical masses. The arrival of new, more sensitive telescopes with enormous monitoring capacity will allow a comprehensive study of the radio emission present in the moving groups found so far, definitely increasing the number of PMS stars with masses dynamically determined.

Resumen

En esta tesis, presentamos un estudio de la radioemisión y la cinemática de un conjunto de estrellas pertenecientes al grupo móvil AB Doradus a través de observaciones de VLA y VLBI. El principal objetivo de nuestro estudio es obtener estimados precisos de la masa dinámica de estrellas jóvenes de baja masa que, en combinación con medidas fotométricas, proporcionen puntos de calibración para modelos de evolución estelar de la presecuencia principal (PMS). La calibración de los modelos PMS parece esencial ya que son extensamente usados para predecir las masas de objetos poco masivos, como enanas marrones y planetas. Estudios previos muestran que las predicciones de los modelos están en desacuerdo con los resultados experimentales para masas inferiores a 1.2 $M_{\odot}$. De entre todas las estrellas incluidas en nuestro estudio, enfatizamos los resultados obtenidos en dos de ellas: AB Dor B y HD 160934.

El sistema binario AB Dor B se observó en tres épocas entre 2007 y 2013 con la red australiana de VLBI (Australian Long Baseline Array, LBA) a una frecuencia de 8.4 GHz. Detectamos, por primera vez, radioemisión compacta de las dos estrellas en la binaria, AB Dor Ba y AB Dor Bb. Este resultado nos permitió determinar los parámetros orbitales de la órbita relativa y de las órbitas absolutas y, consecuentemente, las masas dinámicas individuales: 0.28±0.05 $M_{\odot}$ y 0.25±0.05 $M_{\odot}$, respectivamente. Comparaciones de las masas dinámicas con la predicción de los modelos evolutivos PMS muestran que los modelos subestiman las masas dinámicas de las componentes Ba y Bb de la binaria en un 10−30% y un 10−40%, respectivamente, aunque este desacuerdo no supera el nivel de 2σ. Algunos de los modelos estelares consideran favorable una edad de entre 50 y 100 Myr para este sistema, mientras que otros predicen edades más avanzadas. Junto con AB Dor B, observamos también el conocido sistema estelar AB Dor A, situado a tan sólo $9''$ y compuesto por la propia estrella AB Dor A y por AB Dor C. Los nuevos datos nos obligaron a revisar los valores previamente publicados de los parámetros orbitales y de las masas dinámicas. En particular, encontramos que las masas de las componentes AB Dor A y AB Dor C son 0.86±0.09 $M_{\odot}$ y 0.090±0.003 $M_{\odot}$, respectivamente, que nos permitieron comparaciones con los modelos teóricos estelares. En el caso de AB Dor A, los modelos predicen buenos estimados dentro

de las incertidumbres, favoreciendo una edad temprana de entre 35−50 Myr. En el caso de AB Dor C, los modelos derivan una masa similar a la masa dinámica y una edad de entre 40 y 120 Myr.

Respecto a HD 160934, observamos este sistema con la red europea de VLBI (European VLBI Network, EVN) a 5 GHz en tres épocas entre 2012 y 2014. Vimos que las dos componentes de la binaria, HD 160934 A y HD 160934 c, muestran radioemisión compacta a escalas de VLBI, proporcionando una información precisa de la órbita relativa y de las órbitas absolutas, las cuales fueron analizadas en combinación con medidas orbitales previamente publicadas. Hemos obtenido valores revisados de los elementos orbitales así como de las masas individuales, cuyos estimados fueron $0.70\pm0.07\,M_\odot$ y $0.45\pm0.04\,M_\odot$ para las componentes A y c, respectivamente. Los modelos teóricos predicen masas para la componente A un 10% más bajas que nuestro valor dinámico; de la misma manera las predicciones para la componente c son un 20−40% más bajas que nuestra medida dinámica. La edad del sistema varía entre 40 y 65 Myr dependiendo de los modelos.

Otras estrellas de nuestra muestra incluyen a EK Dra, LO Peg y PW And, observadas con el EVN a 5 GHz. EK Dra y PW And mostraron radioemisión compacta a escalas de milisegundos de arco, mientras que LO Peg presentaba ausencia de emisión en el momento de las observaciones. El escaso número de detecciones nos impidió obtener estimados de sus masas, sin embargo, nos permitieron revisar los valores del movimiento propio y paralaje. De manera complementaria, observaciones en infrarrojo de la compañera de EK Dra nos han permitido una revisión de los parámetros orbitales de este sistema.

En resumen, nuestro proyecto proporciona nuevos datos observacionales para calibrar modelos de evolución estelar de objetos PMS, apoyando la evidencia de que estos modelos tienden a subestimar las masas dinámicas. La llegada de telescopios nuevos y más sensibles con una enorme capacidad de monitorización permitirán un estudio exhaustivo de la radioemisión presente en los grupos móviles encontrados hasta ahora, definitivamente incrementando el número de estrellas PMS con masas dinámicas determinadas.

Table of contents

List of figures

List of tables

Chapter 1

Introduction

1.1 Motivation and aim of this thesis

Stellar evolution models allow us to know and to understand the different phases that the stars cross throughout its existence. As a general rule, the predictions that these models provide fit correctly to the observations and, therefore, are a truly reliable source of scientific information. This is particularly useful to estimate fundamental parameters of the stars, as the mass and radius, from theoretical luminosity-based relationships (e.g., Baraffe et al. 1998; Chabrier et al. 2000). The calibration of these stellar evolution models is important, but it is crucial in the case of young, low-mass objects, since these models are deeply used to determine the masses of planets and brown dwarfs. However, in the particular case of pre-main sequence (PMS) stars with masses below $1.2\,\mathrm{M}_{\odot}$, the efficiency of the models is questionable since the contrast with the observational data reveals some discrepancies (Hillenbrand & White 2004).

Therefore, the calibration of the evolutionary models of low-mass PMS stars can be considered an important task, but certainly is not easy, since it requires precise and independent measurements of luminosities and masses to be compared with the theoretical predictions. Several authors have highlighted these facts in previous works but, nevertheless, there is not enough observational data yet that can help to improve the models (Hillenbrand & White 2004; Stassun et al. 2004; Mathieu et al. 2007).

The study of binary stars belonging to young, moving groups (whose main feature is the common age of their members) is a reasonable approach to increase the number of PMS stars with mass dynamically determined (Zuckerman & Song 2004; Torres et al. 2008). In recent years, several of these moving groups have been discovered. Among all of them, the

AB Doradus moving group (AB Dor-MG) is the most suitable to carry out the study, as it is the closest one, the estimated age is relatively accurate, and it contains stars with significant emission at radio wavelengths (Guirado et al. 2006, 2011; Jason et al. 2007; Azulay et al. 2014, 2015). This last feature is essential because it allows the use of radio interferometry techniques to obtain astrometric information. Using these techniques it is possible to achieve angular resolutions in the sub-milliarcsecond (sub-mas) range, which are needed to solve and study in detail the kinematics (proper motion, parallax, and possible orbits) of the stellar systems.

In particular, very-long-baseline interferometry (hereafter VLBI) astrometry has been able to provide the position of celestial bodies with micro-arcsecond precision, enabling a substantial progress in many astronomical fields, ranging from the establishment of a quasi-inertial reference frame based on distant quasars to the study of the dynamics and structure of our Galaxy. Although the stars are not certainly profuse radio emitters, relevant astrometry studies have been carried out on stellar systems dedicated to determine both the size and distance to star forming regions or stellar cluster through the measurement of proper motion and parallax of their individuals. Studies of stellar astrometry with VLBI include the link between the *Hipparcos* and the extragalactic reference frames (Lestrade et al. 1995), the detection of the light deflection by the Jupiter gravitational field (Fomalont & Koepikin 2003; Bartel et al. 2015), or the detection of unseen low-mass companions (Guirado et al. 1997).

Thereby, according to the previous studies, and counting with the increasing sensitivity of interferometer arrays, we initiated a VLA/VLBI program dedicated to monitor known and possible young binary systems hosting low-mass companions (at least below 0.7 $M_\odot$, where the disagreement between mass measurements and model estimates is most significant), and which are likely to present radio emission. We emphasize that the main goal of this astrometric program is to find objects that may serve as calibrators of low-mass PMS evolutionary models. However, we also provide a wealth of information that complements our understanding of these systems, namely: the study of the nature of the detected compact radio emission, estimates/revisions of proper motions and distances (beyond the precision provided by *Hipparcos*), as well as the orbital parameters from which the dynamical masses are derived. In some particular stars, we are able to test different scenarios to explain the high level of radio emission.

Although our project is limited to a handful of stars (limitation imposed by the monitoring capacity of the interferometric arrays), we consider it constitutes a foundation for future studies of the stellar and substellar evolution using the new generation of radio interferometers (e.g., SKA or pathfinders). These new interferometers will achieve higher resolution, better sensitivity, and larger monitoring speed, which will allow the access to a much larger number of stellar objects, and practically to every member of any moving group discovered. This will help us to collect a large amount of observational data to continue improving the calibration of the evolutionary models of young low-mass objects.

1.2 Thesis outline

We expose briefly the organization of this thesis work. In Chapter 2, we describe the early stages of stellar evolution, from the birth of the stars until their arrival to the PMS, emphasizing the importance of calibrating theoretical PMS evolutionary models. In Chapter 3, we present the stellar moving groups discovered so far, introducing the AB Dor-MG and their stellar systems object of our study. In Chapter 4, we expose the fundamental concepts of the VLBI technique and the data reduction and imaging processes. Chapters 5, 6, and 7 are based on articles already published or in preparation, where we present the particular results on each stellar system studied. In Chapter 5, we focus on VLBI observations of the binary star AB Dor B, including the calculation of the orbital parameters and the estimate of dynamical masses, which facilitate the comparisons with the prediction of PMS stellar models. We also review the new observations of the companion pair in AB Dor A. In Chapter 6, we present a similar study of the star HD 160934, using radio and infrared observations. In Chapter 7, we show our results on the rest of our sample of young, active radio stars of the AB Dor-MG, i.e., observations of EK Dra, PW And, and LO Peg, to better understand the kinematics and radio emission of these systems. In Chapter 8, we summarize the results of this thesis and we expose the future work, discussing the relevance that new radio interferometers will have. Finally, we dedicated two appendices to explain basic concepts of the stellar radio emission and the orbital elements of binary systems.

Chapter 2

PMS stars and stellar evolution models

The life and evolution of a star is a cyclic process. Stars are born in regions of dust and gas that are within the interstellar medium. Throughout their existence, much of the material of the star is returned to the interstellar medium via stellar winds and explosive events. This returned material will constitute the birthplace of new stars. However, the study of the early stages of stellar evolution is not very advanced compared to our knowledge once the star reaches the main sequence. Certainly, the initial mass is the most important property, because it will set other properties such as brightness, temperature, lifetime, and the way to die.

2.1 Early stages of stellar evolution. Pre-main-sequence stars

2.1.1 Stellar formation and early evolution

Fig. 2.1 shows a simple scheme of the early stages of the evolution of a star until reaching the main sequence.

Stage a: An interstellar cloud. Stars are formed in molecular clouds, complexes of gas and dust. These clouds are composed almost entirely by molecular hydrogen (H_2); helium (He), carbon monoxide (CO), and many other molecules with less abundance complete the remaining mass. Only about 1% of the cloud is in the form of dust, that makes the cloud opaque to particular wavelengths. Molecular clouds have large dimensions of ~10-100 pc and masses of the order of 10^5 $M_\odot$. They are in hydrostatic equilibrium with the interstellar medium, with low temperatures of $10-100$ K and densities of 10-300 molecules/cm^3. Molec-

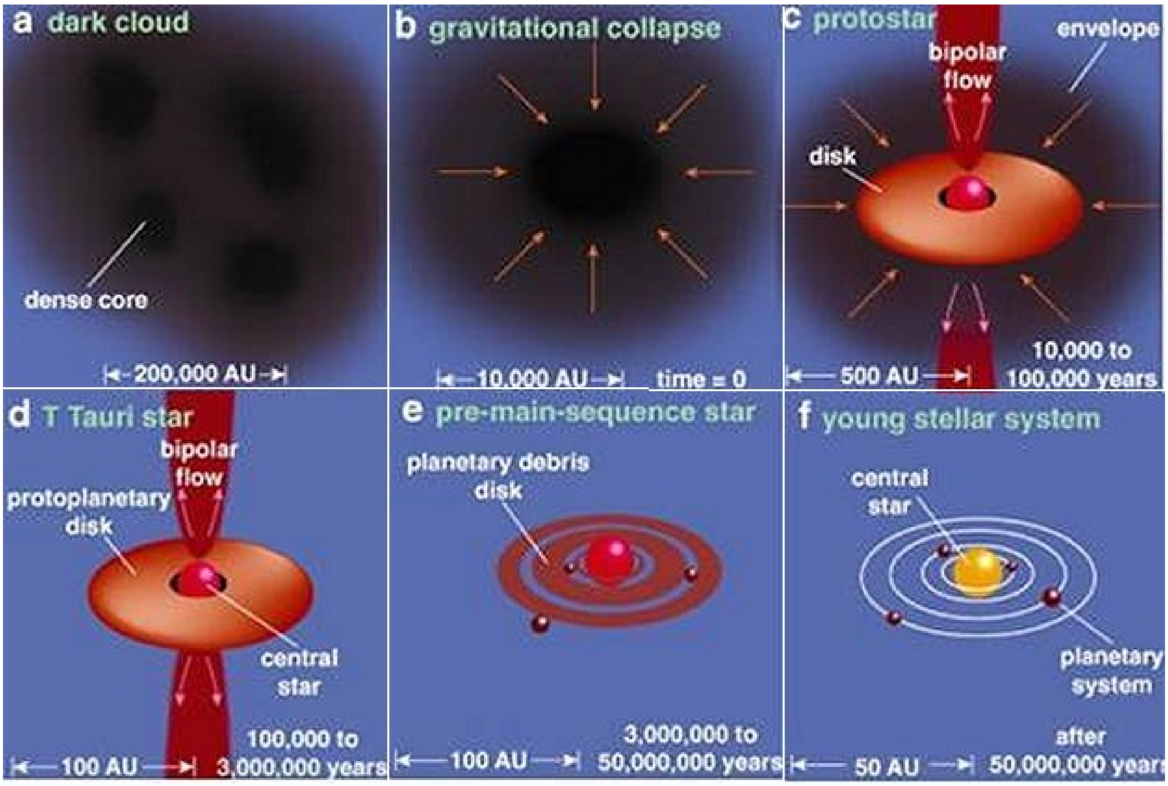

Fig. 2.1 Stages of the formation of a star. Credit: Spitzer Science Center.

ular clouds are not uniform and the gas and dust are distributed around filamentous structures with high density areas, where star formation takes place.

Stage b: Gravitational collapse. The formation of a star begins after a certain event, as may be a collision with another cloud or a supernova explosion, breaks the equilibrium, causing the gravitational collapse of the cloud. This collapse starts when the mass of the cloud exceeds a critical mass value knows as *Jeans mass*, given by

$$M_{\mathrm{J}} \simeq \left(\frac{5kT}{G\mu m_{\mathrm{H}}}\right)^{3/2}\left(\frac{3}{4\pi\rho_0}\right)^{1/2}, \tag{2.1}$$

where k is the Boltzmann constant, T is the temperature of the cloud, G is the Gravitational constant, μ is the mean molecular weight, m_{H} is the weight of an hydrogen atom, and ρ_0 is the initial mass density of the cloud. If we assume typical values in molecular clouds of T and μ, and ρ_0, then $M_{\mathrm{J}} \sim 10^3 - 10^4\,\mathrm{M}_{\odot}$. The densities involved at the beginning of the process are necessarily low and, therefore, the timescale of the gravitational collapse (given by $t_{gc} \propto \rho_0^{-1/2}$) is of the order of millions of years. Due to the collapse, the density of the cloud increases keeping the temperature almost constant. Accordingly, given Eq. 2.1, the Jeans mass decreases. The stability criterion is infringed again and the cloud starts to fragment into smaller pieces that begin to collapse locally. This process continues until the fragments have a mass less than ~0.1 $M_\odot$.

Stage c: Protostar. The large density of the fragments of the cloud, whose rate of increasement is larger in the core than in the surrounding gas, makes the gas opaque. The radiation is trapped, so the central regions start to heat up considerably and the gas pressure increases. At some fragments, the outward force exerted by the pressure gradient may compensate the inward force of the gravity; at this point, the core of this particular fragment comes into hydrostatic equilibrium and appears what is known as *protostar*.

Stage d: Protostellar evolution. The original molecular cloud was supposed to be in slow rotation. Due to the conservation of the angular momentum, by compressing, the collapsing fragments rotate faster leading to the formation of an accretion disk around the protostar where, eventually, planets or other minor bodies can form. Material procedent from the accretion disk falls onto the protostellar core increasing its mass and, therefore, its gravity, breaking the hydrostatic equilibrium. The core suffers an extra compression and the temperature increases. The protostellar phase ends when the major part of the gas that surrounded the star has been accreted and/or sweept away by the stellar radiation. From that moment, the star becomes visible and it begins the *pre-main-sequence* evolution (PMS star). PMS stars that preserve part of the surrounding accretion disk during the early evolution are called *T Tauri*.

Stage e: Pre-main-sequence star. The star undergoes to a gravitational contraction that forces the central temperature to increase until it is high enough to onset the hydrogen burning. The first (transient) nuclear burning occurs when the central temperature reaches about 10^6 K and deuterium ignites (D-burning). The D-burning produces energy enough to partially counterbalance the radiative loss at the stellar surface thus, slowing down the gravitational contraction. However, due to the small abundance of deuterium such phase is relatively short, and once deuterium has been exhausted the gravitational contraction stars again until the star reaches temperatures of about 10^7 K when the complete hydrogen burning begins. The end of the PMS phase occurs when the star reaches the zero age main sequence location (ZAMS; **stage f**); in this phase the star is fully sustained by the nuclear energy released by the hydrogen burning, meanwhile, the secondary elements are at their equilibrium abundances.

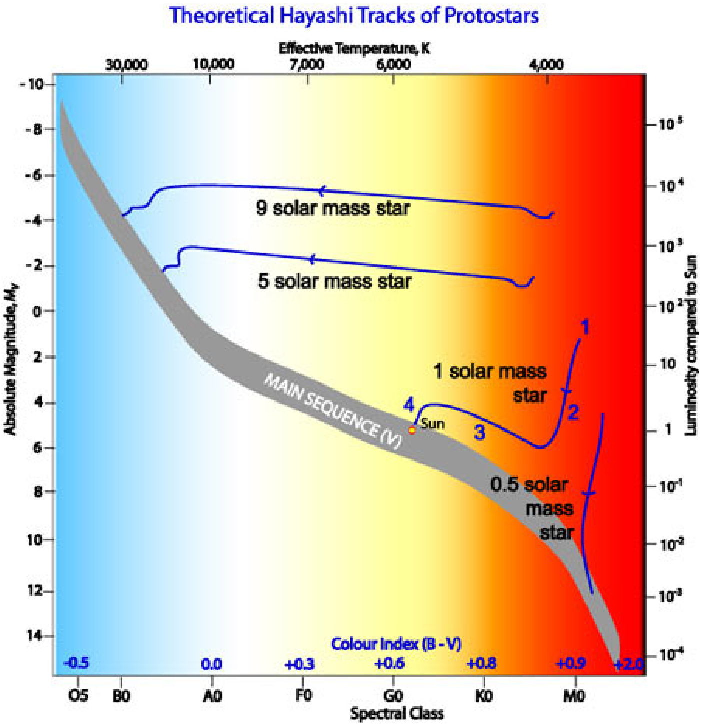

Fig. 2.2 Tracks that show the predicted evolutionary way on the H-R diagram for 0.5, 1, 5, and 9 $M_{\odot}$ during the PMS stage. Credit: ATNF.

2.1.2 H-R diagram. The Hayashi tracks

Once the star has ended its embedded phase into the cloud and it becomes visible, it can be placed it in the Hertzsprung-Russell (H-R) diagram. This point corresponds to the beginning of the PMS evolution which is a relatively short phase when compared to the total stellar lifetime (about 1%). The evolutionary path and the time that the star spends in the PMS phase depends mainly on the stellar mass; the more massive the star, the earlier it reaches the main sequence (Fig. 2.2).

In order to give a qualitative description of the main properties of a PMS star, we will focus on a solar-like model. At the beginning of the PMS the star is fully convective and the luminosity comes from gravitational contraction. The energy transport is efficient, making the temperature to remain fairly constant. This implies an almost vertical descent of the star in the track (from 1 to 2 in Fig. 2.2; this vertical line in the H-R diagram is called Hayashi track). At this stage the star evolves on a thermal time scale (Kelvin-Helmholtz time) and the collapse warms up the star. As the central temperature reaches about 10^6 K, it becomes efficient the nuclear burning of deuterium (D-burning, point 2 in Fig. 2.2). Such a reaction releases energy enough to partially counterbalance the energy loss at the stellar surface (about 70-80% of the stellar luminosity in dependence of the total mass). As a result, the gravitational contraction is partially halted and the star evolves approximately on the deuterium burning nuclear time scale. Such a time scale is essentially the time on which deuterium is exhausted.

Once deuterium has been depleted the gravitational contraction stars again, the internal temperature rises and the opacity drops. Consequently, the central region ceases to be convective because radiation can now transport the energy efficiently. At this point, the star stops to follow the vertical Hayashi track evolving towards higher temperatures (from 2 to 3 in Fig. 2.2). Since the radiative core allows energy to escape, the luminosity no longer decreases but it slightly increases with the temperature. Contraction continues until the temperature becomes high enough to ignite nuclear reactions in the core (T $\approx$ (8−10)$\times 10^6$ K), which provide additional heating and thermal pressure. The gravitational collapse progressively slows down and once the energy generated by hydrogen fusion compensates the energy loss at the surface and the secondary elements of the H-burning reach their equilibrium configuration, the contraction stops and the star reaches the ZAMS (point 4 in Fig. 2.2).

More massive stars (5−9 $M_\odot$ tracks in Fig. 2.2) move almost completely horizontally, and very fast, during its PMS stage. This is because the nucleus heats up quickly and become radiative rapidly. In contrast, stars less massive than the Sun (i.e., 0.5 $M_\odot$ tracks in Fig. 2.2) move vertically across the Hayashi tracks because the core never becomes radiative; therefore, they are fully convective during the complete PMS stage (see Fig. 2.3). We notice that the D-burning is important in young low-and very-low mass stars. At young objects, the inclusion/neglection of the D-burning phase might introduce an offset in the age/mass estimation. As seen in Fig. 2.4, the presence of D-burning leads to a larger luminosity at the same age with respect to the luminosity of the same object without D-burning.

2.2 Internal structure of a star

A star can be approximated to a sphere of gas that remains in thermal and hydrostatic equilibrium for most of its life. Depending on the evolutionary phase the energy required to maintain such an equilibrium is generated by gravitational contraction (mainly during the PMS phase) and/or by nuclear burning. The energy is then transported to the stellar surface where it is radiated away. The energy loss at the surface (cooling of the star) along with the change of the stellar chemical composition in presence of nuclear burning modify the structure in such a way that a continuous readjustment of the physical conditions inside the star is required to maintain the equilibrium. The conditions of the internal equilibrium can be

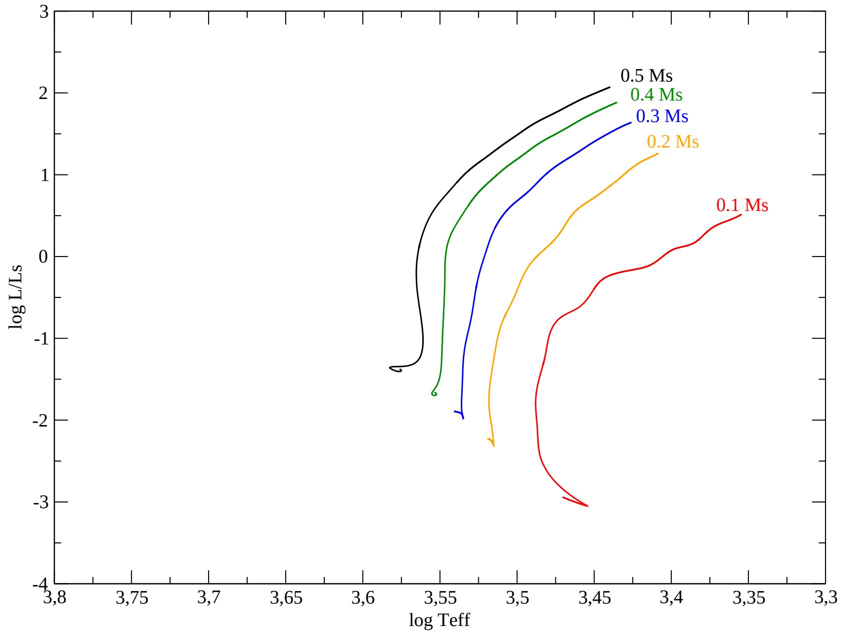

Fig. 2.3 Evolutionary tracks of stars with mass below 0.5 $M_\odot$. The verticality indicate that they are fully convective objects (see Section 2.1.2). Courtesy E. Tognelli.

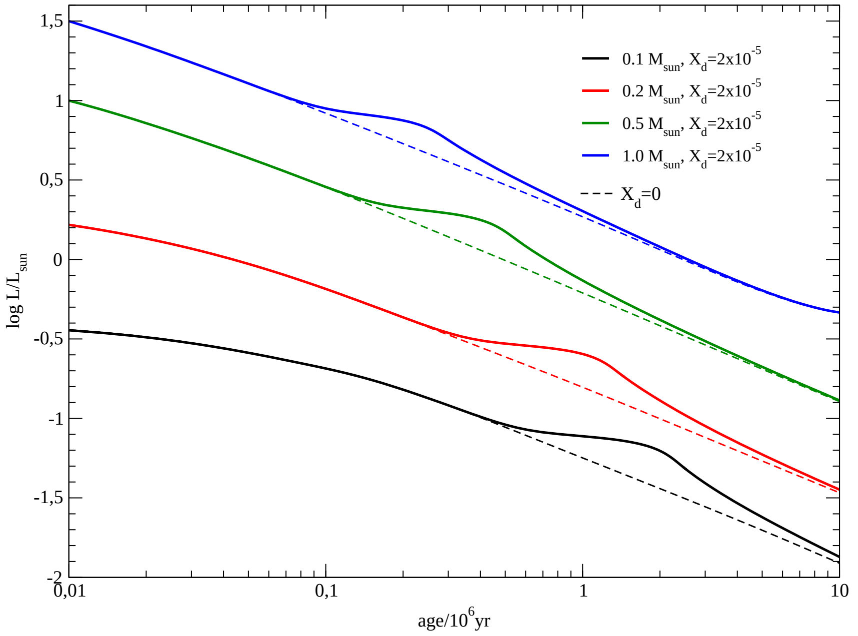

Fig. 2.4 Effect of the D-burning for isochrones at different solar masses. X_d indicates deuterium abundance. The inclusion of the D-burning leads to larger luminosities (see Section 2.1.2). Courtesy E. Tognelli.

expressed in four differential equations that describe the gas pressure, the mass distribution, and the production and transport of the energy (e.g., Carroll & Ostlie 2007):

$$\frac{\mathrm{d}P}{\mathrm{d}r} = -G\frac{m}{r^2}\rho \qquad \text{(hydrostatic equilibrium)} \tag{2.2}$$

$$\frac{\mathrm{d}m}{\mathrm{d}r} = 4\pi r^2\rho \qquad \text{(mass conservation)} \tag{2.3}$$

$$\frac{\mathrm{d}L}{\mathrm{d}r} = 4\pi r^2\rho\epsilon \qquad \text{(energy production)} \tag{2.4}$$

$$\begin{cases} \dfrac{\mathrm{d}T}{\mathrm{d}r} = -\dfrac{3}{4ac}\dfrac{\kappa\rho}{T^3}\dfrac{L}{4\pi r^2} & \text{(radiative transport)} \\ \dfrac{\mathrm{d}T}{\mathrm{d}r} = \left(1-\dfrac{1}{\Gamma^2}\right)\dfrac{T}{P}\dfrac{\mathrm{d}P}{\mathrm{d}r} & \text{(convective transport),} \end{cases} \tag{2.5}$$

where P is the star pressure, m is the star mass contained in a sphere of radius r, L is the star luminosity, T is the star temperature, ρ is the star density, G is the gravitational constant, ϵ is the energy generation rate per unit of mass and time ($\epsilon = \epsilon_n + \epsilon_g - \epsilon_\nu$ where, ϵ_n is the energy generated by nuclear burning, ϵ_g is the energy generated by the gravitational contraction, and ϵ_ν is the energy carried away by the neutrinos), a is the radiation constant, c is the speed of light, κ is the opacity, and Γ is the adiabatic exponent.

To complete the physical description of the internal structure of a star we need an equation of state (EOS) relating the thermodynamic variables. The EOS in stellar conditions is complicated because one needs to cover a very large regime of temperatures and densities where non-ideal effects are important. Besides the EOS, opacity and nuclear reaction rates are also needed to solve the stellar structure equations. Similarly to the EOS, the computation of the opacity in stellar condition is cumbersome.

Moreover, to resolve the stellar structure equations we also need boundary conditions, namely, values or relations between the unknown functions for some value of the radius r. In the center of the star, where $r = 0$, the conditions are obvious, because mass and luminosity are practically zero: $m = 0$ and $L = 0$. At the stellar surface, where r is the value of the total radius of the star, the boundary conditions consist in specify the pressure and the temperature obtained at the bottom of the stellar atmosphere, which is the outermost external region of a star. For a more realistic approach, it is necessary to use atmosphere models which provide the distribution of temperature and pressure on the surface of the stars.

The different stellar evolution models are obtained by the numerical resolution of the four differential equations 2.2, 2.3, 2.4, and 2.5, namely, by the deduction of the $P(r)$, $m(r)$, $L(r)$, and $T(r)$ functions. A suitable theory for stellar evolution requires an accurate EOS, a precise atmosphere model, a correct treatment of opacity/convection, and appropriate boundary conditions between the interior and the atmosphere of the star.

2.3 PMS stellar models

As we have noted earlier, our present knowledge of the PMS evolutionary phase is limited. Obtaining precise stellar evolution PMS models is a fundamental fact, because they are the primary mean to calculate the masses of young stars, so necessary to better understand the star formation and early stellar evolution. However, the formulation of a PMS theoretical model corresponding to a realistic description is extremely difficult, because it implies to consider the effects of dense and cold matter and complex processes such as accretion, rapid rotation, magnetic fields, and presence of dust in the atmosphere (Hillenbrand & White 2004; Mathieu et al. 2007). The different PMS stellar evolution models vary in the consideration of some physical aspects that we revise in turn:

Equation of state

Low-mass PMS stars are dense and cool objects, with typical central densities of 10-$10^3\,\mathrm{g\,cm^{-3}}$ and central temperatures lower than 10^7 K. These conditions generate strong interactions between particles, so the relation between the thermodynamic values is dominated by non-ideal effects and an EOS far from that of an ideal gas is required. In these case, is not only important the treatment of temperature-ionization and dissociation; the pressure-ionization and dissociation along the ρ/T profile is an essential but a very complicated task (Chabrier & Baraffe 1997). Much effort has been done by many authors to derivate an accurate EOS for low-mass PMS stars; a summary of the different equations reported in the literature can be found in Saumon et al. (1995) and Siess et al. (2000).

Convection

The low-mass stars considered in this thesis do not have a radiative core; therefore, convection is the dominant energy transport mechanism. Let's assume a mass element ("cell") that moves upwards adiabatically (i.e., with no energy exchange) due to a small perturbation; the cell will expand, changing its temperature and density. Convection will occur if the temperature gradient in the stellar interior is steeper than the temperature gradient in the cell, that is, $\left|\frac{\mathrm{d}T}{\mathrm{d}r}\right|_a < \left|\frac{\mathrm{d}T}{\mathrm{d}r}\right|_c$ (Schwarzschild criterion, where a indicates the temperature gradient of the bubble and c the temperature gradient in the surroundings): in this case, the cell will keep moving upwards. The simplest, and widely adopted, approach to treat the convection is the mixing-length theory or MLT (Böhn-Vitense 1958). According to the MLT, the gas in the star becomes unstable at a determined radius r_0 where the Schwarzschild criterion is satisfied. In this case, rising cells near r_0 will travel a characteristic length L, the mixing length, before they blend into the surrounding gas, releasing its energy into the ambient medium; the cells cool, fall back, absorb energy, and rise again a distance L (see Fig. 2.5).

The MLT of convection makes a large number of assumptions, namely, it ignores shocks or acoustic waves, magnetic fields, stellar rotation, and it assumes that the mixing length L, the size, and the velocity are equal for all cells, as well as the chemical composition. The PMS models include the MLT via the adjustable parameter α (the mixing-length parameter) defined as $\alpha = L/H_p$, where H_p is the pressure scale height simply calculated by $H_p = P/(\rho g)$. Typically, larger (smaller) values of α, a more (less) efficient convection, produce hotter (cooler) evolutionary tracks. The majority of the PMS models uses the MLT approach for a different value of α (from ~0.5 to ~2.3), which is fix for each model.

Nevertheless, there are other convection treatments, as the full spectrum turbulence models (FST; Canuto & Mazzitelli 1991; Canuto et al. 1996). This more sophisticated model exploits the fact of the unrealistic size of convective eddies (size of the convection currents) as given by the MLT formalism. The FST is developed to replace the one-eddy MLT scheme with a large number of convective eddies with different sizes given by a much more complex turbulent approach. The FST has also the advantage of avoiding the use of a fixed mixing length parameter. Rather, the FST model proposes that the mixing length corresponds to a function of the convective boundary (which is equivalent to a tunable α, see Ventura et al. 1998 for details).

Other approach consists in solving the full fluid equation of motion through a multi-dimensional, time-dependent, radiative hydrodynamical numerical simulations in 3D (i.e. Tremblay et al. 2015). However, due to the long computational time and numerical complexity

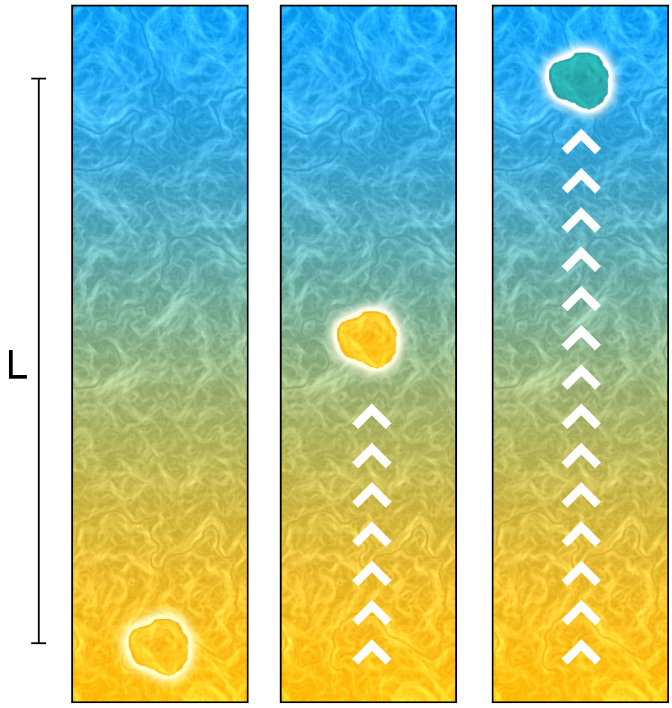

Fig. 2.5 Scheme of the mixing length theory. In the stellar interior, a cell will move upwards a distance L (the mixing length) before blending into the surrounding gas. Credit: public domain.

such simulations are used to solve part of stellar external envelope and, at present, they cannot yet be included in stellar evolutionary codes.

Basic models of stellar atmospheres

The stellar atmosphere can be considered as the transition from the stellar interior to the interstellar medium, acting as a boundary condition. The physical conditions of the atmospheric layers will determine the nature of the continuous spectrum, absorption and emission lines, therefore the modeling of the stellar atmosphere is essential. Basically, the atmospheric models used for a PMS star will deal with the solution of the differential radiative equation 2.5. Some of the commonly basic approximations made to obtain an atmospheric model are i) plane-parallel atmosphere, in which the physical parameters depend only of the vertical depth, ii) local thermodynamic equilibrium (LTE), which means that the radiation is determined only by the local temperature following a blackbody spectrum, and iii) the absorption coefficient (or equivalently the opacity, κ in Eq. 2.5) is independent of the frequency (i.e., "grey" –colorless– atmospheres). The "grey-body" approximation is far to be real: the absorption coefficient is highly frequency-dependent, causing significant deviations of the actual temperature distribution over the atmosphere from that derived for the grey approximation. The non-grey atmospheric model, where frequency-dependent opacities are actually used, attempts to cope with this limitation, in particular in the case of cold atmospheres where dust and grains can form (see e.g., Allard 2011). Another improvement consists in replacing the plane parallel approximation with the spherical geometry (see e.g., MARCS models; Gustafsson et al. 2008).

Another crucial issue for the atmosphere of low-mass stars is the convective heat transport. Indeed, convection is not only present in the interior of the star but it also penetrates into the stellar atmosphere. Similar approaches to that discussed in the previous section via MLT or FST are usually taken (i.e., Heitler et al. 2002; Hauschildt et al. 1999).

2.3.1 Comparison of track-predicted and dynamical masses

Fundamental calibration of PMS stellar evolution models is, however, not yet established. To perform this calibration, it is necessary to compare the predicted masses with those determined dynamically. It has been found that for stars with masses higher than $1.2\,\mathrm{M}_{\odot}$, there is a good correspondence between the dynamical masses and those predicted by the models; however, for stars with masses lower than that value, the models offer different predictions (see Fig. 2.6) and often underestimate the dynamical value between 10%-30%. Actually, several authors has indicated the necessity to fit well the evolution models for PMS stars (Hillenbrand & White 2004; Stassun et al. 2004; Mathieu et al. 2006). In Fig. 2.7, extracted from the work of Hillenbrand & White (2004), these differences can be corroborated. The contrast between the predictions of evolutionary tracks and observational data collected on this type of stars is worrisome from the point of view of the reliability of the models. Finding PMS stars with independent measurements of their mass and luminosity (and reasonable estimates of age and distance) is difficult and, although dynamical masses measurements of PMS stars have become more numerous during the last years, there is still a very small number of these stars with dynamically determined masses, so new measurements are essential to provide tests of theoretical models.

In this work, we will compare our observational results with the predictions of several PMS models. In practice, we will use sets of evolutionary tracks corresponding to the models of Baraffe et al. (1998, 2015; BCAH98, BHAC15), Siess et al. (2000; S00), Montalbán & D'Antona (2006; MD06, see also Montalbán el al. 2004), and Tognelli et al. (2011, 2012; TDP12). In turn, we report briefly the main properties and assumptions of each of these

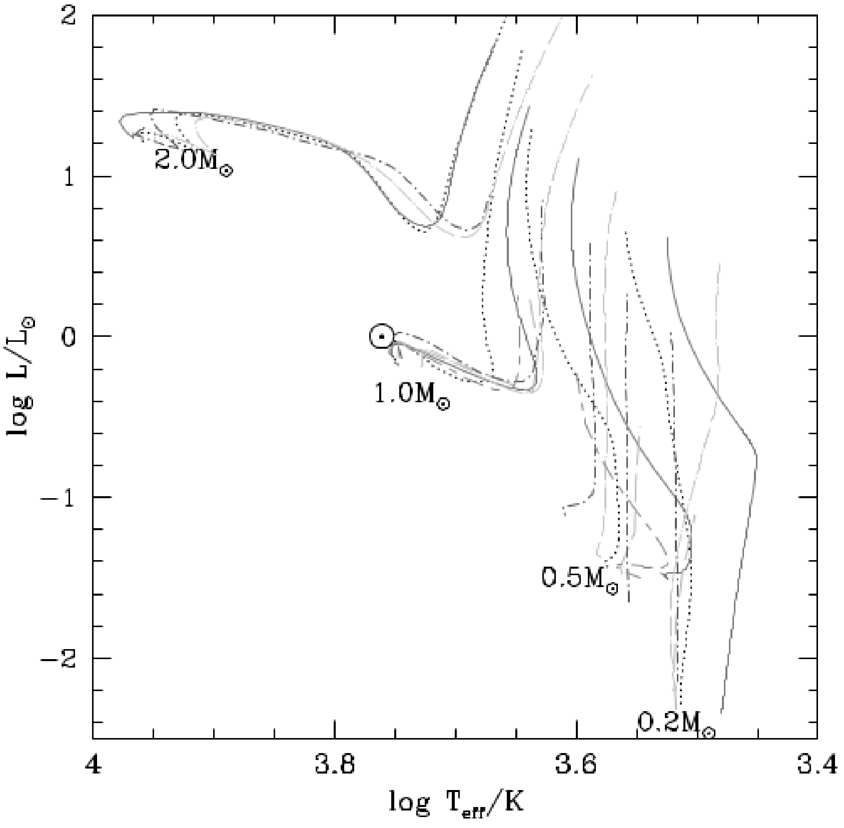

Fig. 2.6 Variations between different PMS evolutionary tracks for masses of 0.2, 0.5, 1.0, and 2.0 M$_\odot$ (Hillenbrand & White 2004).

models. We refer to the cited papers for a complete discussion of the physics and calculations involved.

BCAH98 models

PMS tracks of Baraffe et al. (1998) are possibly the most widely extended models covering masses from 1 M$_\odot$ down to the brown dwarf limit (~0.075 M$_\odot$) for solar type metallicities of [M/H]=0 and −0.5 (see Chabrier et al. 2000 and Baraffe et al. 2002 for an extension to young dwarfs down to one Jupiter mass). These models use the equation of state given in Saumon, Chabrier & Van Horn 1995), updated opacities (Iglesias & Rogers 1996), and non-grey atmosphere models of Hauschildt et al. (1999). Convection is treated according to the MLT for values of $\alpha = 1.0$ and 1.9. The tracks also use helium abundances of $Y = 0.275$ for [M/H] = 0 and $Y = 0.25$ for [M/H] = −0.5. Baraffe et al. (2015) present new, improved models; they maintain the calculation based on the input physics used to describe the stellar

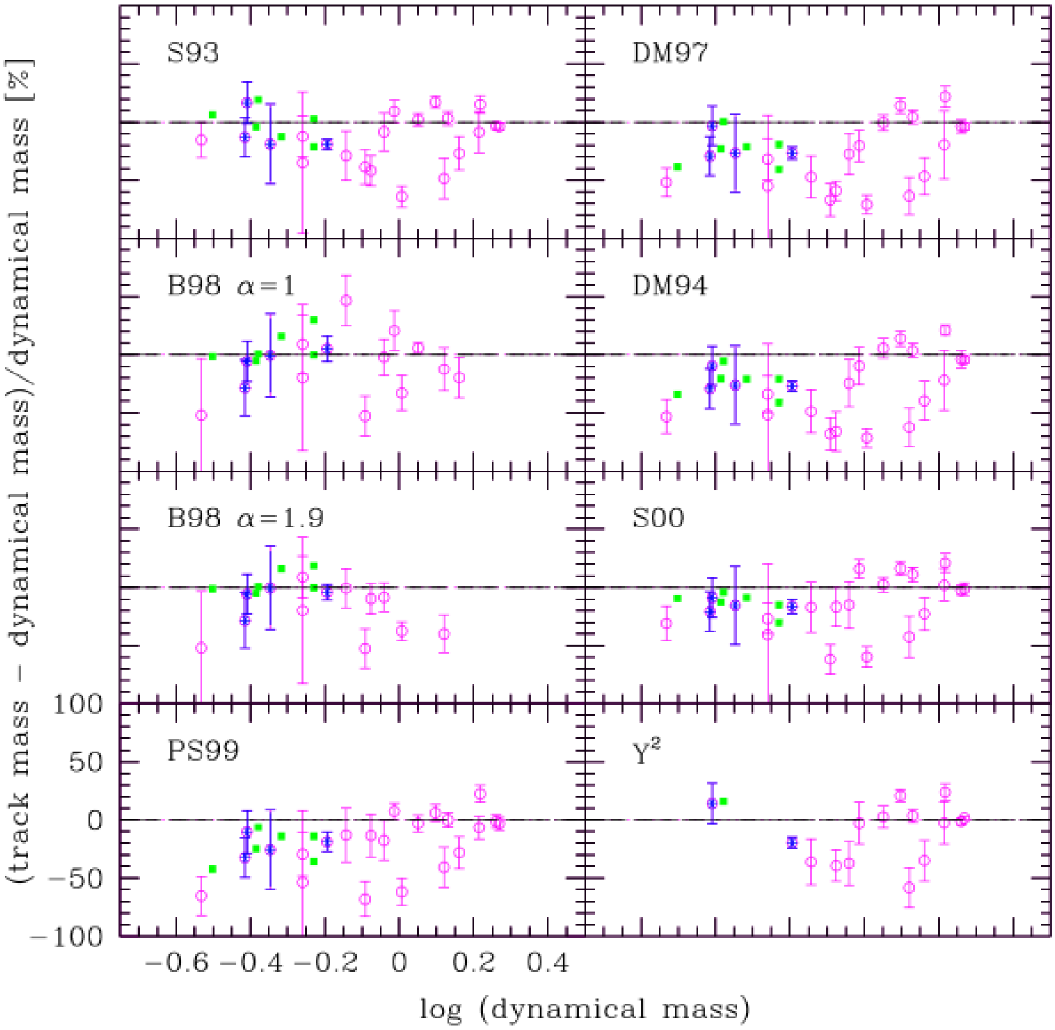

Fig. 2.7 Plot taken from Hillenbrand & White (2004) representing the percentage difference between tack-predicted and dynamical masses as a function of dynamically determined mass for different evolutionary models for PMS stars (S93, Swenson et al. 1994; DM94, D'Antona & Mazzitelli 1994; DM97, D'Antona & Mazzitelli 1997; B98, Baraffe et al. 1998; S00, Siess et al. 2000; PS99, Palla & Stahler 1999). Different colors correspond to different temperatures scales adopted to obtain the mass in each model.

and substellar interior structure, but incorporate modifications concerning the atmosphere models and the treatment of convection.

S00 models

The S00 models cover masses in the range 0.1−7.0 $M_\odot$ and the computations were carried out for four different metallicities ($Z = 0.01, 0.02, 0.03, 0.04$). The tracks use an EOS adopted by the scheme developed by Pols et al. (1995), the Iglesias & Rogers (1996) opacities, and the non-grey atmosphere models of Plez (1992). They treat convection with MLT with $\alpha = 1.6$.

MD06 models

Improving substantially those of D'Antona & Mazzitelli (1997), the MD06 models use the equation of state given in Montalbán et al. (2000), helium mass fraction of $Y = 0.28$, Rogers & Iglesias (1996) opacities, and non-grey atmospheres of Hauschildt et al. (1999) or Heitler et al. (2002). Different models of convections can be considered (MLT for different values of α and FST as in Canuto & Mazzitelli 1991) as well as different chemical compositions for [M/H] between −0.3 and +0.3.

TDP12 models

Very recent PMS stellar tracks covering a wide range of metallicities ($Z = 0.0002$ to 0.03), chemical composition (three values of Y for each Z), and stellar masses (0.2 to 7 $M_\odot$). They use the 2006 OPAL equation of state (Rogers & Iglesias 2002), the 2005 OPAL opacities (Iglesias & Rogers 1996) for $\log T[\mathrm{K}] \geq 4.5$ and the Ferguson et al. (2005) ones for lower temperatures. The MLT formalism is used to treat convection, with $\alpha = 1.20$, 1,68, and 1.90. Detailed non-grey atmosphere are considered (Brott & Hauschildt 2005; Catelli & Kurucz 2003).

Chapter 3

The AB Doradus moving group

Our interest in PMS stars resides in the determination of fundamental parameters of low-mass stars, essentially the dynamical mass, which should serve as benchmarks for PMS stellar evolutionary models. Binary stars belonging to young, nearby moving groups are specially favourable for this purpose. The age and kinematics of their members are relatively well known which in turn facilitate their location in H-R diagrams. Among all the moving groups recently discovered, the AB Doradus moving group (AB Dor-MG) appears as the most suitable to carry out our studies, basically due to its proximity and the presence of binary systems with remarkable emission in radio waves.

3.1 Young nearby moving groups

A moving group is an association of coeval stars moving in a coherent way through the galaxy. Stars belonging to the same moving group are thought to proceed from the same cloud of gas and share relevant properties as its kinematics, its chemical composition, and, specially, its age. Until late 1990s, the only groups known within ~60 pc of Earth where the Hyades (HYA) (located at 45 pc) and the Ursa Major (UMa) (at 25 pc) clusters; these two associations are hundreds of million of years old. During the recent years, however, a significant population of nearby stars have been discovered with ages between 5 and 100 Myr. The young ages and the close distances to Earth of these new moving groups allow to perform studies to understand the early phases of the stellar evolution and to provide information on the formation of planetary systems.

However, moving groups are not easy to identify. As each group is located at a close distance to the Sun, its members are scattered over the sky, without an overdensity of stars

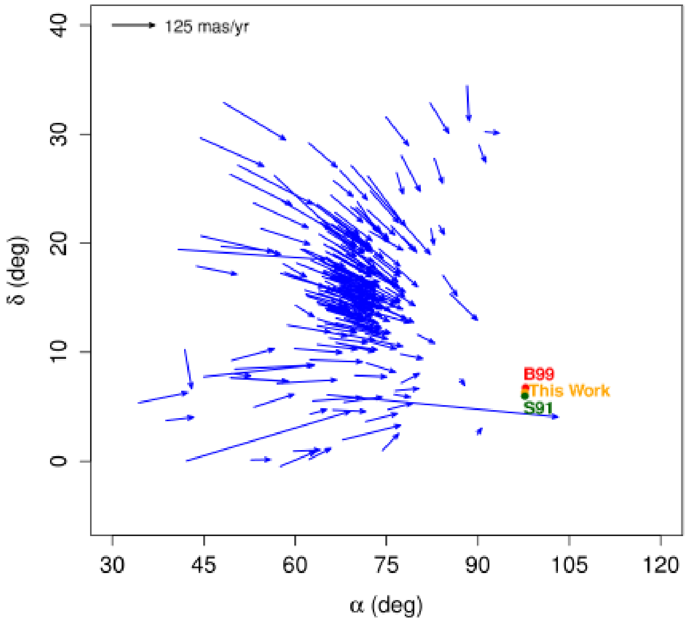

Fig. 3.1 Proper motion vectors of the Hyades members and the convergent point coordinates derived in different works. Projection effects of the real movements, that are parallel, induce apparent convergence towards a point in the sky with coordinates near (97°, 6°) (Galli et al. 2012).

that can be distinguished from the stellar background. However, since all members move coherently in the same direction, the proper motions of the stars seem to concur towards a convergent point due to perspective effects (Fig. 3.1). The knowledge of the convergent point may serve to identify which stars belong to a moving group and which are just field stars, but this criteria might not be sufficient, because some stars can move in the same direction with different velocities.

As members of a moving group are formed from the same cloud, they share a common space velocity within the galaxy, with typical dispersion of a few $\mathrm{km\,s^{-1}}$ or less. Also because of this common formation, young members of these associations should not be much dispersed around the galaxy yet. Fig. 3.2 taken from Song et al. (2003) allow us to visualize this fact: if we traced the positions of the stellar members back in time, we can see that all members were grouped in a smaller place. Therefore, one of the best ways to detect them is to look for objects with similar 6-dimensional coordinates (U, V, W, X, Y, Z), which we define in turn. On the one hand, the components (U, V, W) are the galactic space-velocity coordinates (U positive toward the center of the galaxy, V positive in the direction of galactic rotation, and W positive towards the north galactic pole) and they are calculated from the proper motion, the parallax, and the radial velocity of the stars, following the formulae given

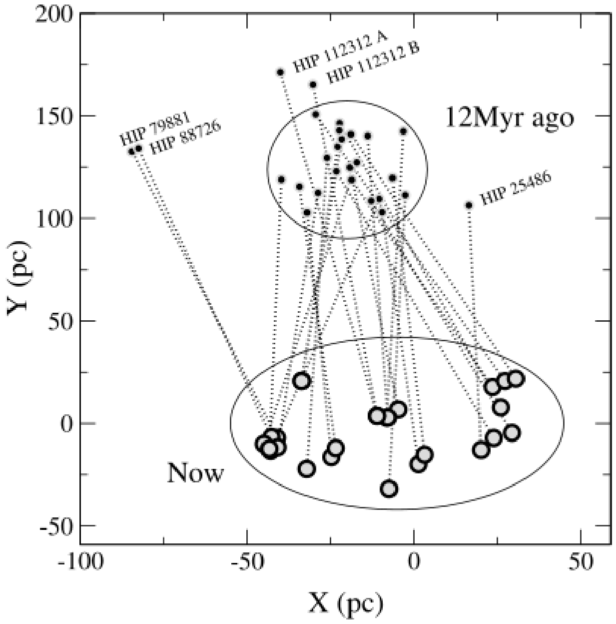

Fig. 3.2 Positions of β Pic moving group now and at the time of its birth (12 Myr ago) taken from Song et al. (2003). X and Y are the galactic positions, where X is positive toward the galactic anticenter and Y is positive in the direction of the galactic rotation. Assuming constant velocity trajectories, we can see that all members in the β Pic moving group, that now are dispersed in ~100 pc, were confined in a smaller space about 12 Myr ago.

in Johnson & Soderblom (1987). The *Hipparcos* (Perryman et al. 1997) and the *Tycho* (Høg et al. 2000) catalogs, together with others like the Two Micron All Sky Survey (2MASS, Skrutskie et al. 2006) provide precise proper motions and parallaxes; measurements of radial velocities, meanwhile, can be found in the literature reported by several authors. On the other hand, the components (X,Y,Z) are the coordinates of the galactic positions, and are defined in the same directions as (U,V,W). However, as it occurs with the convergent point method, this kinematic similarity could not suffice to establish the membership of a particular object to a moving group. In search for young moving groups (a few Myr old), frequently other criteria based on high level of chromospheric and coronal activity, high rotation rate, or lithium abundance are adopted. Stars fulfilling the conditions above can be considered *bona fide* candidates to be members of a particular moving group (Malo et al. 2013). Several moving groups have been reported so far.

With an age of 8-12 Myr, TW Hydrae (TWA) was the first young nearby moving group discovered (de la Reza et al. 1989, Gregorio-Hetem et al. 1992). At that time, the group consisted of four T Tauri stars located within 10° of the star TW Hya. Nowadays, this moving group has 18 well-identified members and more than 30 potential candidates (Mamajek 2005,

Table 3.1 Properties of young nearby moving groups

Name of the group	Age (Myr)	Distance (pc)	Number of members
TW Hydrae (TWA)	8–12	40–62	22
β Pictoris (βPMG)	12–22	18–40	48
Tucana-Horologium (THA)	20–40	38–51	44
Columba (COL)	20–40	26–63	41
Carina (CAR)	20–40	11–42	23
Argus (ARG)	30–50	15–48	64
AB Doradus (AB Dor-MG)	70–120	19–50	89

Nakajima & Morino 2012) placed at a distance range of 40-62 pc. The identified members are those accomplishing the following conditions: (i) age consistent with that of the group they belong to, (ii) a precise radial velocity measurement (error <5 km s^{-1}), (iii) a precise parallax measurement (error <7 pc), and (iv) a significant proper motion measurement (higher than 5σ).

The β Pic moving group (βPMG) was proposed by Zuckerman et al. (2001) and it is composed by 33 well-defined members sharing the galactic motion of the star β Pic. It is placed at a distance of 18–40 pc, has an age of 12–22 Myr, and the vast majority of its members are located in the southern hemisphere.

The Great Austral Young Association (GAYA) was a group of many young stars with similar kinematic and photometric properties. Torres et al. (2008) subdivided this association into three groups: Tucana-Horologium (THA), Columba (COL), and Carina (CAR). The Tucana and the Horologium associations were discovered independent and simultaneously by Zuckerman & Webb (2000) and Torres et al. (2000), respectively. Due to their similar space motion, age (20–40 Myr), and distance (38–51 pc) were grouped together in THA. It has 52 members, and at least 7 of them form a nucleus around the star β Tuc. COL and CAR associations, meanwhile, have a similar age to that of THA and 21 and 8 well-defined members, respectively. Other young moving group discovered was Argus (ARG), first proposed by Makarov & Urban (2000); it is placed at a distance of 15–48 Myr, has an age of 30–50 Myr, and is composed by 11 well-defined members.

Last, but not least, we have the AB Doradus (AB Dor-MG), which is explained in the next section. A summary of the properties of each one of the groups is shown in Tables 3.1 and 3.2 (adapted from Gagné et al. 2014).

Table 3.2 Mean galactic motion and position of young nearby moving groups

Name of the group	UVW ($\mathrm{km\,s^{-1}}$)	σ_{UVW} ($\mathrm{km\,s^{-1}}$)	XYZ (pc)	σ_{XYZ} (pc)
TW Hydrae	−9.87, −18.06, −4.52	4.15, 1.44, 2.80	12.49, −42.28, 21.55	7.08, 7.33, 4.20
β Pic	−10.94, −16.25, −9.27	2.06, 1.30, 1.54	9.27, −5.96, −13.59	31.71, 15.19, 8.22
Tucana-Horologium	−9.88, −20.70, −0.90	1.51, 1.87, 1.31	11.39, −21.21, −35.40	19.29, 9.17, 5.39
Columba	−12.24, −21.32, −5.58	1.03, 1.18, 0.89	−27.44, −31.32, −27.97	13.79, 20.55, 15.09
Carina	−10.50, −22.36, −5.84	0.99, 0.55, 0.14	15.55, −58.53, −22.95	5.66, 16.69, 2.74
Argus	−21.78, −12.08, −4.52	1.32, 1.97, 0.50	14.60, −24.67, −6.72	18.60, 19.06, 11.43
AB Doradus	−7.12, −27.31, −13.81	1.39, 1.31, 2.16	−2.37, 1.48, −15.62	20.03, 18.83, 16.59

3.2 The AB Doradus moving group

The AB Dor-MG was first identified by Zuckerman & Song (2004) with the determination of similar three-dimensional galactic space motions (U, V, W) of stars near the stellar system AB Dor. Among all discovered moving groups, this is the closest to Earth, with a range distance of 19−50 pc (Malo et al. 2013, Gagné et al. 2014). It is composed of 89 *bona fide* members (Torres et al. 2008) distributed through the northern and the southern hemispheres in a non-spherical form (although, if we approximate them with a sphere, it would have a radius of about 100 pc; Torres et al. 2008). A dozen of the members contained in a region of $\sim$10 pc form the nuclear group, which is located entirely in the southern hemisphere at an average distance of less than 20 pc (Zuckerman & Song 2004). We note that the number of objects belonging to the AB Dor-MG is subjected to change since several authors continuously propose more stars to be new members: 43 by Torres et al. (2008), 6 by Schlieder et al. (2010), 6 by Schlieder et al. (2012), 1 by Bowler et al. (2012), and 8 by Nakajima & Morino (2012). A representation of the AB Dor-MG included in Torres et al. (2008) can be seen in Fig. 3.3.

An alternative representation of *bona fide* members of the AB Dor-MG is displayed in Fig. 3.4, where the galactic positions (X, Y, Z) (mean values −7.12, −27.31, −13.81, in pc) and the spatial velocities (U, V, W) (mean values −2.37, 1.48, −15.62, in km s^{-1}) are plotted. In this figure, the members are represented by red dots and the models by red ellipsoids; the projections are represented by blue dots and orange lines, respectively. All members of the moving group concur to a convergent point near the solar apex, as can be noticed in Fig. 3.5.

The majority of the members of the AB Dor-MG are of spectral type F, G, and K (masses in the rage 0.7−1.5 $\mathrm{M}_{\odot}$). M-type stars have also been discovered (masses <0.7 $\mathrm{M}_{\odot}$) as well as a few objects of spectral type A and B (masses >1.5 $\mathrm{M}_{\odot}$). Moreover, the stars in the moving group are, in general, young variable fast rotators and have active chromospheres that produce stellar spots (being some of them, in addition, binary stars). Therefore, many members

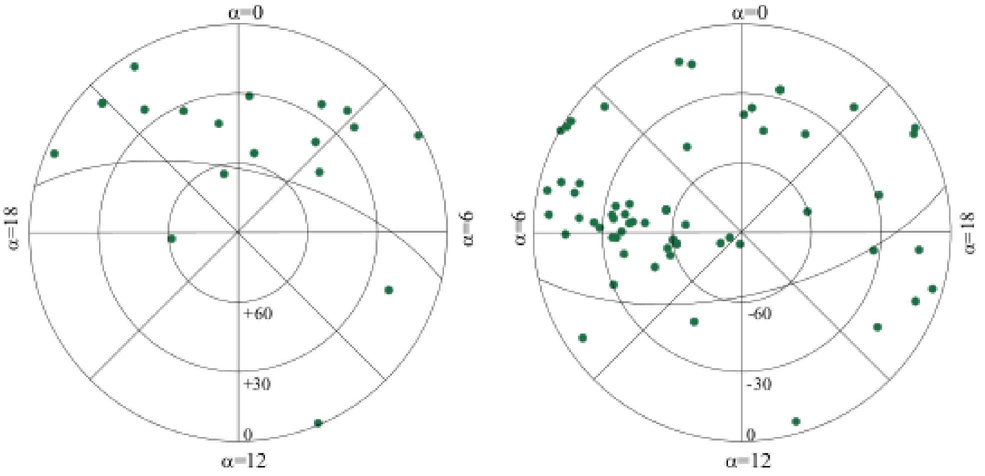

Fig. 3.3 Projection of the AB Dor-MG. At left, the northern hemisphere. At right, the southern hemisphere (Torres et al. 2008).

have been proposed as RS CVn or BY Dra variables, namely: PW And, IS Eri, V577 Per, AB Dor, UX Col, UY Pic, WX Col, TZ Col, TY Col, AK Pic, BD+20 1790, V372 Pup, PX Vir, HD 160934, LO Peg (Torres et al. 2008). In the last years, substellar members have also been detected: Wahhaj et al. (2011) and Bowler et al. (2012) observed the L4 and L0 brown dwarf companions to the AB Dor-MG members CD−35 2722 and 1 RXS J2351+3127, with masses 31±8 M_{Jup} and 32±6 M_{Jup}, respectively; furthermore, Delorme et al. (2012) discovered a 4−7 M_{Jup} free-floating planet, CFBDSIR2149−0403, of spectral type T7, and Naud et al. (2014) detected a planetary-mass companion to the star GU Psc, of spectral type T3.5 and with a mass range of 9−13 M_{Jup}. Ongoing projects are dedicated to the detection of substellar objects in the AB Dor-MG (as well as in the other groups), therefore, more discoveries of this kind of objects are expected (Gagné et al. 2014).

3.2.1 The age of the AB Dor moving group

The age of the AB Dor-MG is still a matter of discussion and different estimates can be found in the literature. Zuckerman et al. (2004) first proposed and estimate of 50 Myr based on comparisons of the intensity of Hα emission of the late K- and M-type stars in Tucana association with those in the AB Dor-MG and from the positions of M-type members of the AB Dor-MG in an M_K versus V-K diagram. In contrast, Luhman et al. (2005) proposed an

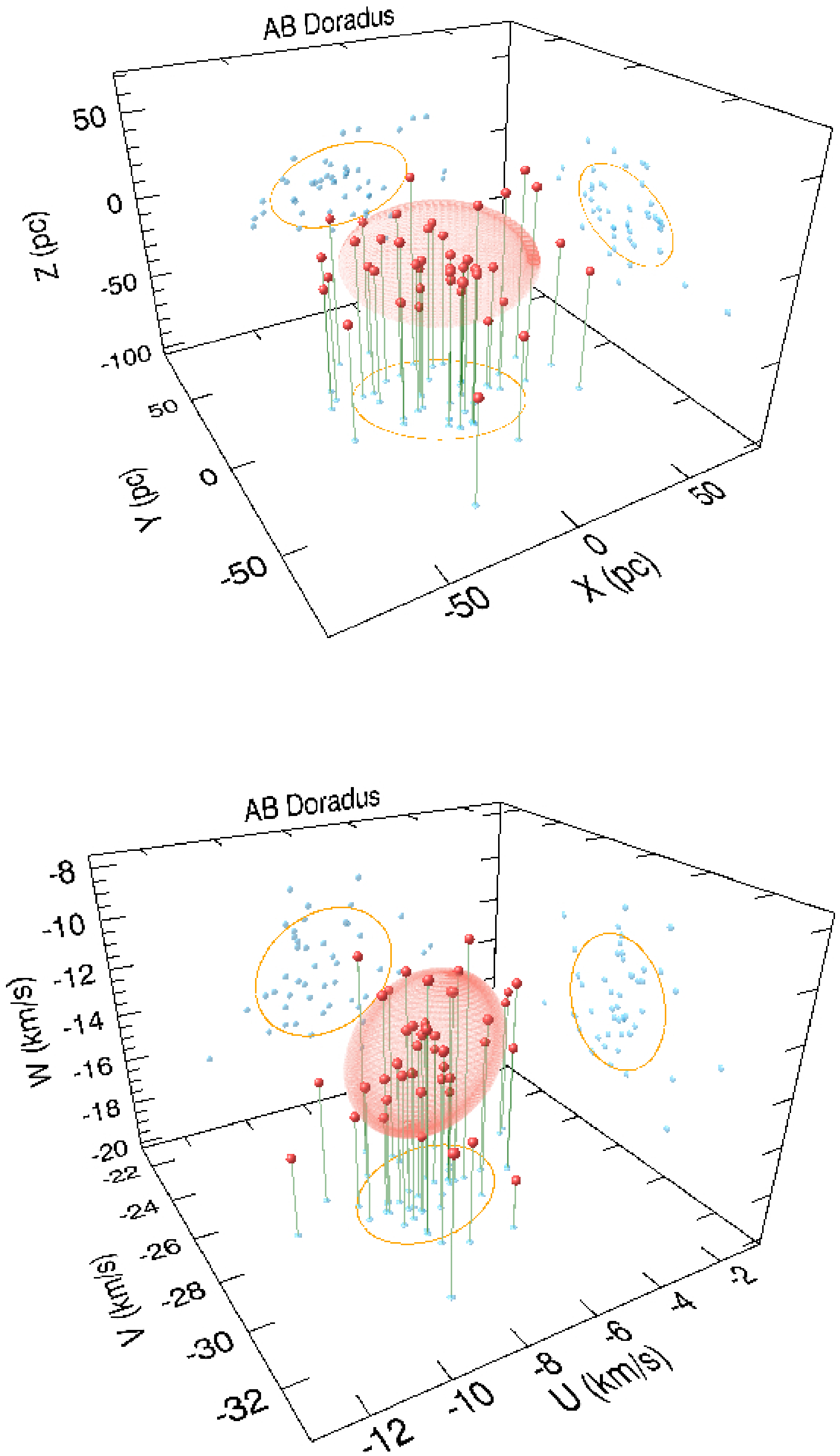

Fig. 3.4 Galactic positions and spatial velocities of the well-defined members of the AB Dor-MG. Members are represented by red dots and the models by red ellipsoids; the projections are represented by blue dots and orange lines, respectively (Gagné et al. 2014).

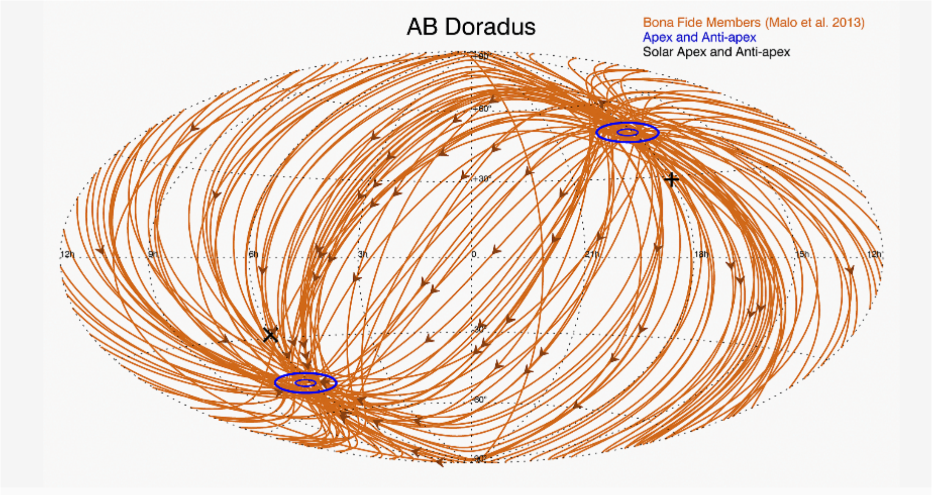

Fig. 3.5 Proper motion of each member of the AB Dor-MG as a function of position. From the position of each object, a great circle is drawn on the celestial sphere following the direction of the proper motion vector. The intersection of the circles shows two convergence points (the apex and anti-apex) which are typically near the Solar apex and anti-apex (Gagne et al. 2014).

age coeval with the Pleiades (100−125 Myr) after comparing the AB Dor-MG members with stars of the Pleiades and IC 2391 (35−50 Myr) open clusters in a M_k versus V-K diagram. Based on these considerations, they assume a conservative age of 75−150 Myr. Moreover, noting that the space motions of both groups are similar, they suggested that the AB Dor-MG has a common origin with the group of the Pleiades. Ortega et al. (2007) reinforced the idea of the common origin, based on the similarity of the galactic 3D orbits of the AB Dor-MG with those of the Pleiades, in turn very different to the orbits of other open clusters like α Persei (85−90 Myr) and IC 2602 (50 Myr). Recently, Barenfeld et al. (2013) reported a lower limit age >110 Myr for the AB Dor-MG nucleus, obtained from PMS contraction times for K-type members that have reached the main sequence.

3.2.2 The AB Doradus system

The well-known stellar system AB Doradus, the one that provides the name to the AB Dor-MG, deserves a closer look as it has a capital importance in our work. AB Doradus is placed at a distance of ~15 pc and it is actually a quadruple system formed by two pairs of stars separated by 9″, AB Dor A and AB Dor B (Fig. 3.6). AB Dor A (= HD 36705 = HIP 25647) is the main star of the system. This K0V star displays a high level of radio activity (Lim et al. 1992, Fig. 3.7; Guirado et al. 1997) generated by its rapid rotation (0.51 days) (more details of the stellar radio emission in Appendix 1). Given its high-level of radio emission,

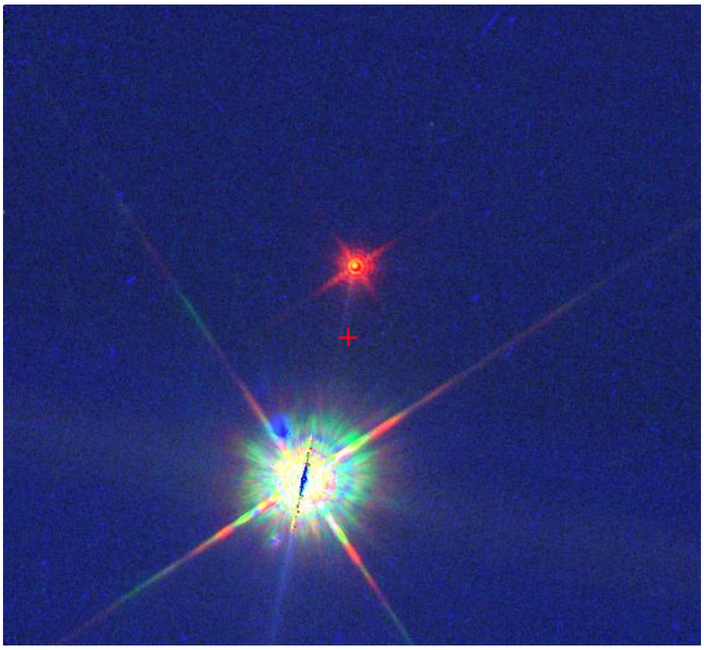

Fig. 3.6 Image of AB Dor A (*bottom*) and AB Dor B (*top*) taken by the instrument WFPC2 of the *Hubble Space Telescope* (HST) on 16 April 2008. Credit: HST archive.

during the early 90's AB Dor A was monitored astrometrically with VLBI (see Chapter 4) as part of a program to link the optical reference frame (defined by the positions of the stars observed by the ESA's astrometric satellite *Hipparcos* (Lindegren & Kovalevsky 1995; Lestrade et al. 1995) and the celestial reference frame, defined by VLBI positions (Lestrade et al. 1995). However, AB Dor A was not finally included in the set of radio stars defining the link between both references frames; rather, the VLBI and *Hipparcos* data revealed the presence of a low-mass companion, AB Dor C (0.090 $M_\odot$; Guirado et al. 1997) orbiting AB Dor A at an average angular distance of $0.''2$. Imaging this new low-mass companion was difficult and it had to wait until the VLT near-infrared observations carried out by Close et al. (2005; 2007) using commissioning time of the Simultaneous Differential Imager (SDI) at the VLT, which allowed independent photometry of AB Dor C, free from contamination of the much brighter AB Dor A (see Fig. 3.8). The combination of precise measurements of the dynamical mass and photometry of AB Dor C provided relevant consequences in terms of calibration of the mass-luminosity relationship for young, low-mass objects (see Fig. 3.9): basically, stellar model predictions tend to underweight the mass of the observed objects. A vivid discussion about the nature, age, and characterization of this new object followed to this result, including new observations using the VLT chronograph (Boccaletti et al. 2008), VLT SIMPHONI (Thatte et al. 2007), SPITZER (Plavchan et al. 2009), VLTI (Guirado et al. 2011), and LBA (see Chapter 5).

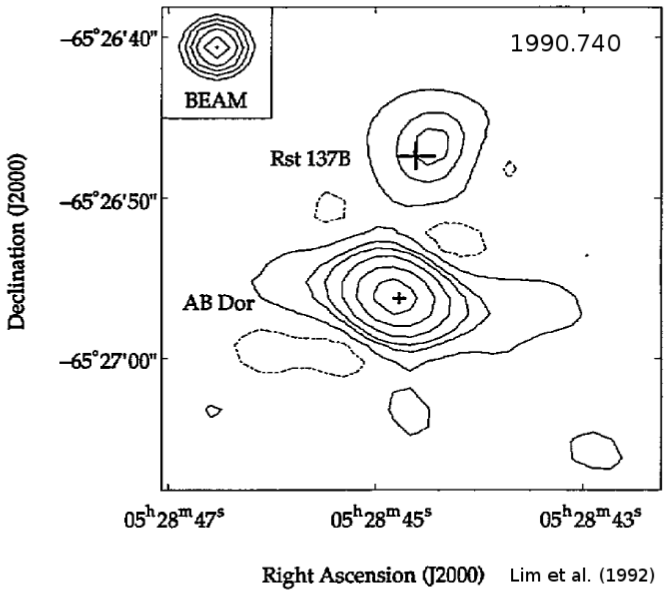

Fig. 3.7 Contour plot of the radio image of AB Dor A and AB Dor B taken on 1990 September 27 with ATCA. The optical positions of the stars are indicated by crosses. Contour levels are −0.3, 0.3, 1.0, 1.5, 2.5, 4.0, and 6.0 mJy. The synthesized beam (FWHM = 5.″4) is shown in the upper left-hand portion of the image (Lim et al. 1992).

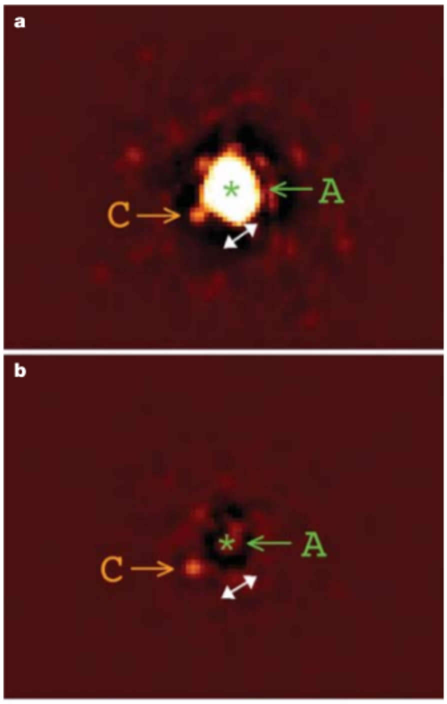

Fig. 3.8 **a.** Discovery image of AB Dor C with the VLT NACO SDI high contrast camera taken on 2004 February 2. **b.** Same image after subtraction of the scattered light from AB Dor A. The system separation (white arrow) was 0.″156 (Close at al. 2005).

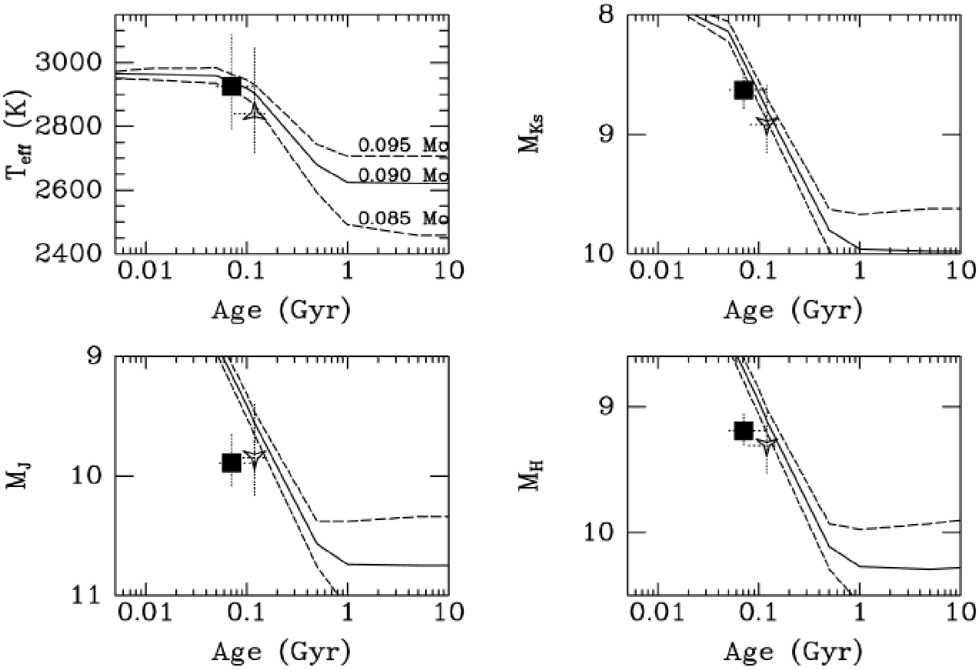

Fig. 3.9 Calibration of evolutionary models (tracks corresponding to 0.085, 0.090, and 0.095 M$_\odot$; Chabrier et al. 2000) with measurements of dynamical mass and luminosity for AB Dor C (0.090±0.005 M$_\odot$). M$_J$ and M$_H$ (magnitudes referred to the near-infrared JHK bands) values are plotted for an age of 75 (black square; Close et al. 2007) and 120 Myr (open triangle; Luhman et al. 2005). Even considering different ages for the system, there is some discrepancy between the predicted fluxes for this object (Close et al. 2007). This plot suggests the need to count with more objects suitable to serve as calibration points for the models.

Table 3.3 Selected stars from the AB Doradus moving group

Name	R.A. (h m s)	Dec. (° ′ ″)	Spectral type	Parallax (mas)	Detection?
PW And	00 18 20.89	+30 57 22.23	K2V	32.68 ± 1.00	Y (see Chapter 7)
IS Eri	03 09 42.29	−09 34 46.58	G0V	26.73 ± 1.12	N (< 0.04 mJy/beam)
V577 Per	03 33 13.49	+46 15 26.53	G5V-M0V	29.08 ± 1.02	N (< 0.03 mJy/beam)
AB Dor B	05 28 44.47	−65 26 46.31	M5-6	65.93 ± 0.57	Y (see Chapter 5)
AB Dor A	05 28 44.83	−65 26 54.86	K0V	65.93 ± 0.57	Y (see Chapter 5)
BD+20 1790	07 23 43.59	+20 24 58.66	K5Ve	31.60 ± 5.00	N (< 0.05 mJy/beam)
PX Vir	13 03 49.65	−05 09 42.52	G5V	46.10 ± 0.81	N (< 0.06 mJy/beam)
EK Dra	14 39 00.22	+64 17 29.84	G1.5V	29.30 ± 0.37	Y (see Chapter 7)
HD 160934	17 38 39.63	+61 14 16.03	K7Ve	30.19 ± 2.00	Y (see Chapter 6)
LO Peg	21 31 01.71	+23 20 07.37	K8V	40.32 ± 1.06	Y (see Chapter 7)
GJ 856	22 23 29.10	+32 27 33.92	M3V	64.47 ± 6.49	N (< 0.03 mJy/beam)
HIP 114066	23 06 04.84	+63 55 34.36	M1V	40.81 ± 1.60	N (< 0.05 mJy/beam)

Meanwhile, it is known that AB Dor B (=Rossiter 137 B) is composed by the stars AB Dor Ba and AB Dor Bb, which have spectral types M5 and M5-6 (Close et al. 2007), respectively, and are separated by an angular distance of ∼0.″06 (Guirado et al. 2006; Janson et al. 2007). The system shows a high rotation period period of 0.38 days (Lim 1993; Wolter et al. 2014) and it is also a strong radio emission as shown by observations with the Australian Telescope Compact Array (ATCA; Lim 1993, Fig. 3.7; Wolter et al. 2014).

3.3 A search for radio emission in the AB Dor moving group

Given the remarkable scientific output of AB Dor A (and AB Dor B, as we will see in Chapter 5), we considered desirable to count with new, similar stars, that is, young binaries, luminous both in infrared and radio wavelengths. As said above, numerous stars in the AB Dor-MG are fast rotators, showing traces of magnetic activity (as stellar spots) that well could be radio emitters, just as the representative star of the group. Certainly, the study of the radio properties of the AB Dor-MG has its own interest: although radio emission is often favored by the young age, it thought to faint rapidly as the stars approach the ZAMS. The stars in the AB Dor-MG, with an intermediate age between active T-Tauri and ZAMS stars, appear as an excellent scenario to study how the radio emission of a sample of active late-type stars, distributed over a range of stellar rotation periods, declines as they contracts towards the ZAMS. In addition, many of the AB Dor-MG stars are accessible by telescopes in the northern hemisphere. The previous reasoning was the main motivation to use observations with the Very Large Array (VLA; either archival data or newly proposed observations) to search for radio emission of the group member of the AB Dor-MG.

For these exploratory observations, we selected a sample of ten AB Dor-MG members based on the following criteria:

- We restricted the declination to $\delta > -20°$.
- We selected the star candidates to be radio-emitters, that is, objects with strong X-ray emission, spot activity, and high rotation rate.
- We favor the observation of objects with "high-probablity membership" to the AB Dor-MG, as defined by Torres et al. (2008). Members of a moving group may spread across a large portion of the sky, which increases the chance of including interlopers. 9 out of our 10 proposed stars (Table 3.3) are high-probability members. The only exception is EK Dra, whose group membership has been discussed (López-Santiago et al. 2006) but unable to be confirmed using dynamical convergence analysis (Torres 2008). Nevertheless, given its relatively high level of radio emission, we decided to maintain EK Dra in our sample.

In Table 3.3 we show the stars of our sample, including AB Dor A and AB Dor B. Aside of this later system, other stars with detected radio emission are EK Dra, LO Peg, PW And (from VLA archival data), and HD 160934 (from new VLA observations). All of them have been the target of VLBI observations (HD 160934, EK Dra, LO Peg, and PW And for the first time) to either determine their fundamental parameters (in the case of the binaries AB Dor A, AB Dor B, HD 160934 and EK Dra) or explore its possible binarity (LO Peg and PW And).

Regarding the non-detected stars, despite they are classified as active, flare stars, they were not detected in our VLA observations (noise floor in Table 3.3). In a closer look, we see that in some cases an earlier spectral type (IS Eri, V577 Per, PX Vir) combined with relatively large distances (>40 pc) could difficult the detection. However, other stars with similar spectral classification and distances are regularly detected with the VLA (e.g., EK Dra); therefore these non-detections may just reflect the variability of the radio emission, whose mechanism could be "switched off" at the time of observation. These stars are not treated anymore in this work, although known nearby binaries as PX Vir and GJ 856 are particularly good targets for our program and deserve further opportunities to find possible radio emission.

Chapter 4

Introduction to the VLBI technique

Very-long-baseline interferometry (VLBI) is the central technique used throughout this thesis work. We have exploited the high angular resolution and the large precise astrometry provided by VLBI, as well as the increasing sensitivity obtained by arrays like the EVN or the LBA. Although there is ample and very detailed literature about VLBI written by renowned authors (e.g., Burke & Graham-Smith 2009; Thompson, Moran & Swenson 2001, and references therein), before proceeding to the presentation of our observations and results, we should make a brief introduction to the technique, including relevant aspects for this work, such as data acquisition, processing, and descriptions of some usual tools used for performing the (phase-referenced) maps of the radio sources.

4.1 The two-element interferometer

At the diffraction limit, the angular resolution θ of an instrument is given by the Rayleigh criterion

$$\theta \approx \frac{\lambda}{D}, \tag{4.1}$$

where λ is the radiation wavelength and D is the diameter of the instrument. To achieve a resolution similar to that of an optical telescope, a radio telescope should have a size many times larger compared; for a radio telescope observing at a wavelength of 6 cm have the same resolution as an optical telescope of 5 m, its diameter should be of about 500 km. However, combining multiple radio telescopes of reasonable sizes and synchronizing its signals, it is possible to simulate one of larger size, using the technique known as *interferometry*.

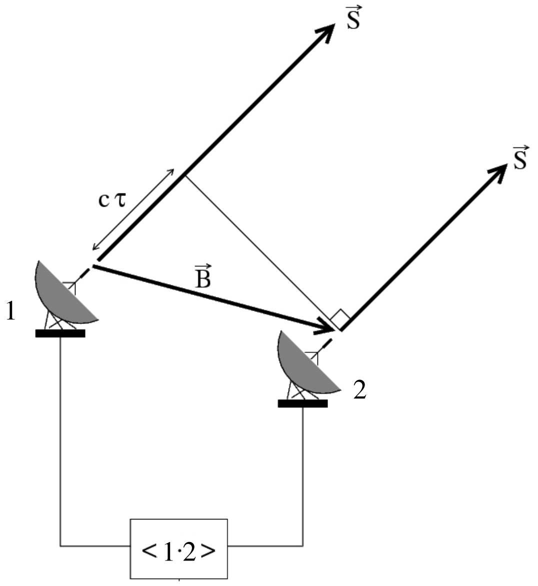

Fig. 4.1 Multiplier interferometer formed by two antennas.

To better understand the interferometric technique results convenient to study the two-element interferometer in response to a point source, for which both the Earth's rotation and atmosphere are not considered.

Consider the interferometer shown in Fig. 4.1. For monochromatic and unpolarized radiation, the voltage measured by the antenna 1 is:

$$v_1(t) = A\cos(\omega t), \tag{4.2}$$

where A is the maximum amplitude of the voltage (amplitude of the electric field); ω, the angular frequency of the radiation ($\omega = 2\pi\nu$; ν, the frequency of the radiation) and t, the time. Antenna 2 is separated from the antenna 1 by a vector $\vec{B}$ called baseline, such that the wavefront that comes from a radio source in the direction $\vec{S}$ (being $\vec{S}$ a unitary vector) reaches the antennas with a geometric delay of

$$\tau_g = \frac{\vec{B}\cdot\vec{S}}{c}. \tag{4.3}$$

The voltage measured by the antenna 2 is, therefore,

$$v_2(t) = A\cos(\omega(t-\tau_g)) \tag{4.4}$$

and the final voltage, result of the multiplication of the voltage provided by each antenna individually, would be

$$R(t) = \frac{A^2}{2}[\cos(2\omega t - \omega\tau_g) + \cos(\omega\tau_g)], \tag{4.5}$$

and its temporal average,

$$Re(t) = \frac{A^2}{2}\cos(\omega\tau_g). \tag{4.6}$$

The quantity $Re(t)$ provided by the interferometer is proportional to the specific intensity of the source, $I(\vec{S}) \propto A^2$, with a coefficient of proportionality of $\cos(\omega\tau_g)$.

Applying a phase shift of $\frac{\pi}{2}$ radians to the signal from one of the antennas, is possible to obtain a response from the interferometer of

$$Im(t) = \frac{A^2}{2}\sin(\omega\tau_g). \tag{4.7}$$

Combining both responses, Re(t) and Im(t), which have been named as real and imaginary, and considering Euler's formula, the complex visibility V function is defined by

$$V = Re(t) + iIm(t) = \frac{A^2}{2}e^{i\omega\tau_g}. \tag{4.8}$$

Therefore, for a simple two-element interferometer, the components $Re(t)$ and $Im(t)$ are generated simultaneously to construct the complex visibility function.

4.2 The response of an interferometer to an extended source. The *uv* plane

For an extended source, the response of the interferometer can be considered as the addition of the visibilities corresponding to a set of point-like sources. In practice:

$$V = \frac{1}{2}\int_{4\pi} I(\vec{S})e^{i\omega\tau_g}d\Omega = \frac{1}{2}\int_{4\pi} I(\vec{S})e^{i\frac{2\pi\nu}{c}\vec{B}\vec{S}}d\Omega, \tag{4.9}$$

where $d\Omega$ would be the differential solid angle subtended by the source.

In order to recover the value of the intensity $I(\vec{S})$ from the value of the visibility V, and to simplify the calculations, we assume a reference point of the extensive source such that the vector pointing to that point (defined as $\vec{S_0}$) is orthogonal to the baseline vector $\vec{B}$. Following Fig. 4.2, we define a coordinate system $(\vec{U},\vec{V},\vec{W})$ where the axes $(\vec{U},\vec{V})$ are in the plane orthogonal to S_0 and where the axis $\vec{W}$ is, therefore, proportional to $\vec{S_0}$. If (x,y,z) are the coordinates of the vector $\vec{S}$ in the base $(\vec{U},\vec{V},\vec{W})$ and $(u,v,0)$ the coordinates of $\vec{B}$, the scalar product $\vec{B}\cdot\vec{S}$ is

$$\vec{B}\cdot\vec{S} = ux + uy. \tag{4.10}$$

Moreover, the solid angle $d\Omega$, can be written as

$$d\Omega = \frac{dxdy}{\sqrt{1-x^2-y^2}}. \tag{4.11}$$

If we also consider that the source is compact (x $\ll$ 1, y $\ll$ 1), the visibility function can be expressed as

$$V(u,v) = \frac{1}{2}\int_{-\infty}^{+\infty}\int_{-\infty}^{+\infty} I(\vec{S})e^{i\frac{2\pi\nu}{c}\vec{B}\vec{S}}dxdy. \tag{4.12}$$

Therefore, the $V(u,v)$ function is the inverse Fourier transform of $I(\vec{S})$ and, thus, the way to get $I(\vec{S})$ is to compute the Fourier transform of $V(u,v)$.

The set of (u,v) pairs, which corresponds to the coordinates of the baseline vector, determine what is known as *uv plane*. The number of visibilities that we have in the *uv* plane is finite, so the better is sampled, the more reliable is the intensity distribution $I(\vec{S})$ of the radio source.

To improve the sampling of the *uv* plane we can, of course, increase the number of antennas involved in the observation, but above all, take advantage of the Earth's rotation. If we return to figure 4.1 with the two telescopes, we perceive that the Earth's rotation causes that the length and the angle of the vector $\vec{B}$ change over time, sampling then different points of the *uv* plane. The trajectories that define the (u,v) points of each baseline according to the Earth's rotation are known as *uv-tracks*. This is the base of the technique known as *aperture synthesis*, designed by Martin Ryle and Anthony Hewish at Cambridge University in the mid-twentieth century, and for which they received the Nobel Prize in Physics in 1974.

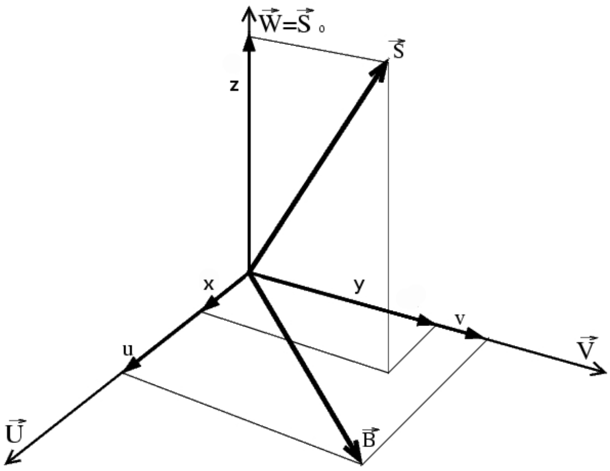

Fig. 4.2 Definition of the coordinate system ($\vec{U}, \vec{V}, \vec{W}$). See Section 3.2.

4.3 Very-Long-Baseline Interferometry

An interferometric network consists of a set of two or more antennas that record the signal from a source. We have been seen that it is necessary to multiply the voltages that arrive to each pair of antennas to then perform a Fourier transform and to obtain the intensity of the source. When this process is done in real time, with the antennas connected via waveguides, optical fibers or radio links to a computer where the calculations take place, we speak of *connected interferometry*.

However, when the separation of the different elements that form the interferometer is so large that it is very difficult to connect them physically, we talk about *very-long-baseline interferometry* (VLBI). In this case, the baselines may reach thousands of kilometres in length. The fact that they are so far from each other makes difficult to obtain the signal in real time; therefore, each station has a very precise atomic clock and records the received signals on tapes or disks. Subsequently, these signals received at each station are taken to a central processor or correlator where, effectively, the signals from each pair of antennas are multiplied. This distinction between connected and VLBI interferometry is somewhat blurred today with the advent of e-VLBI (electronic VLBI) that allows real-time VLBI thanks to the substantial increase in bandwidth for data transmission between the stations and the central processor.

Some disadvantages of the VLBI technique reside, precisely, in the large separation between the antennas. Weather conditions are often very diverse and the different relative speeds of the antenna on a rotating Earth produce Doppler effects on the radiation received at each antenna. Moreover, small synchronization errors between the atomic clocks at each station may cause a decrease in the data quality. However, the long baselines together with the Earth rotation allow for a much better sampling of the *uv* plane, providing information from sources with very little angular extension.

4.3.1 The Australian VLBI network

The Long Baseline Array (LBA) is a VLBI network which is located in the southern hemisphere; it has radio telescopes spread across Australia, New Zealand, and South Africa (Figure 4.3). The LBA core is constituted by the radio telescopes of the Australia Telescope National Facility (ATNF), which include ATCA (Australian Telescope; in turn, a connected interferometer), Parkes, and Mopra, and the antennas in Hobart and Ceduna, belonging to the University of Tasmania. The radio telescopes of the DSN (Deep Space Network) of Tidbinbilla, as well as the Hartebeesthoek radio telescope in South Africa and the Warkworth antenna in New Zealand are also part of the LBA. In addition, a single ASKAP (Australian Square Kilometre Array Pathfinder) antenna located in Western Australia is partially available for observations. The central frequency available for observations ranges from 1.4 GHz to 22.2 GHz (wavelengths from 21 cm to 2 cm). Once the observation has been done independently by each antenna, data are transported to the correlation center in Curtin University of Technology and are processed using the DiFX software correlator (Deller et al. 2007).

4.3.2 The European VLBI network

The European VLBI Network (EVN) is an interferometric array of radio telescopes located all around the world but, mainly, in Europe (Fig. 4.4). Thanks to the large collecting surface of its telescopes, it is the most sensitive VLBI array in the world. The main frequencies/wavelengths that can be observed are: 1.664 GHz (18 cm), 2.268 GHz (13 cm), 4.992 GHz (6 cm), 6.030 MHz (5 cm), 6.668 GHz (5 cm), 8.418 GHz (4 cm), and 22.230 GHz (1 cm). Moreover, at some stations it is also possible to observe at: 0.327 GHz (90 cm), 0.610 GHz (50 cm), 1.416 GHz (21 cm), 15.362 GHz (2 cm), and 43.214 GHz (7 mm). The data recorded on each antenna are correlated later with the EVN MkIV data processor at the Joint Institute for VLBI in Europe (JIVE) with the Correlator Control Software (JCCS) programs (Casse 1999; van Langevelde & Phillips 2002; Campbell 2004). Additionally, the EVN often carries out observations in conjunction with other arrays of radio telescopes as MERLIN in Great Britain or the VLBA in the USA.

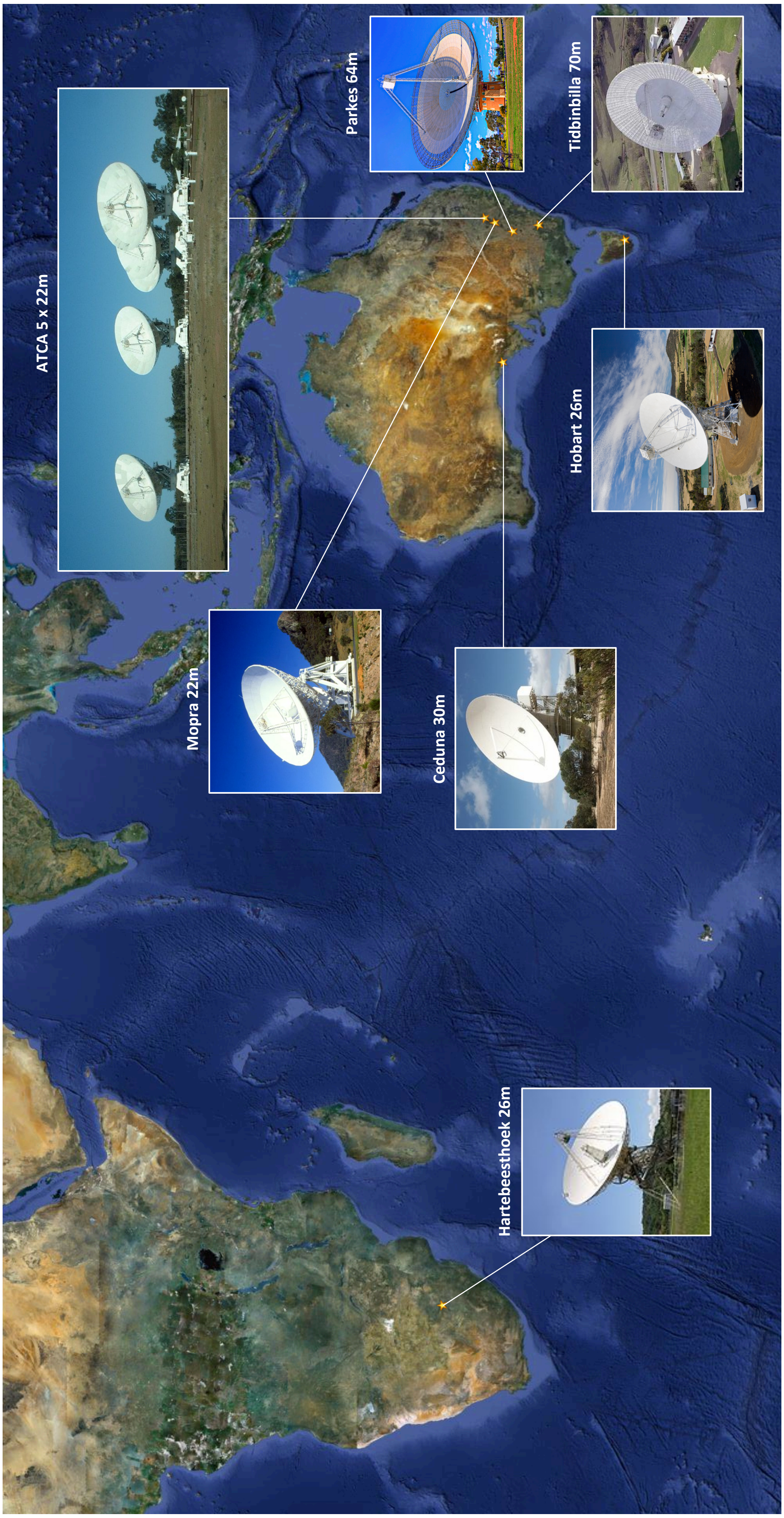

Fig. 4.3 Location of the main antennas used by the LBA.

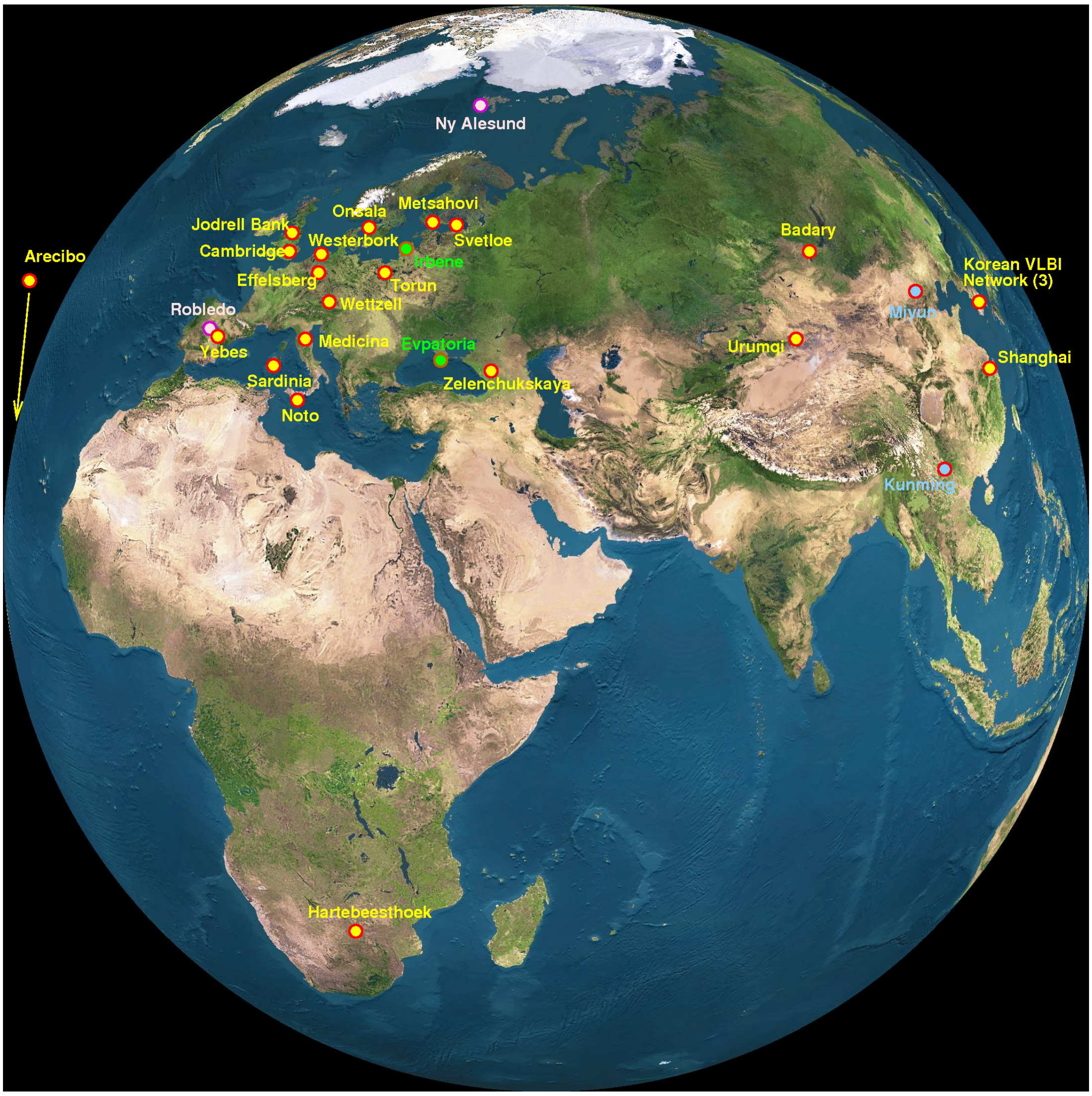

Fig. 4.4 Location of the main antennas used by the EVN. In yellow/red there are shown the current operational antennas; in cyan/red, antennas that soon will be EVN stations; in cyan/blue, new EVN antennas under construction; in pink/purple, non-EVN antennas that have participated in EVN observations; and in green/brown, non-EVN antennas with whom initial EVN tests have been realized. Credit: European VLBI Network.

4.4 Calibration of the data

The visibility $\tilde{V}_{ij}(t,\nu)$ (with amplitude $\tilde{A}_{ij}(t,\nu)$ and phase $\tilde{\theta}_{ij}(t,\nu)$) measured by the interferometer between the antennas i and j in frequency/time can be expressed as the true visibility $V_{ij}(t,\nu)$ (with amplitude $A_{ij}(t,\nu)$ and phase $\theta_{ij}(t,\nu)$) of the source multiplied by the gain factors $G_i(t,\nu)$ and $G_j(t,\nu)$:

$$\tilde{V}_{ij}(t,\nu) = G_i(t,\nu)G_j^*(t,\nu)V_{ij}(t,\nu) + \epsilon_{ij}. \tag{4.13}$$

where ϵ_{ij} is a thermal noise term. The gain factors $G_i(t,\nu)$ and $G_j(t,\nu)$ represent the amplitude and phase errors corresponding to each antenna, and can be defined as:

$$G_i(t,\nu) = a_i(t,\nu)e^{i\phi_i(t,\nu)}, \tag{4.14}$$

Separating the amplitude and phase parts, Eq. 4.13 can be written as:

$$\tilde{A}_{ij}(t,\nu)e^{i\tilde{\theta}_{ij}(t,\nu)} = a_i(t,\nu)a_j(t,\nu)A_{ij}(t,\nu)e^{i[\phi_i(t,\nu)-\phi_j(t,\nu)+\theta_{ij}(t,\nu)]}. \tag{4.15}$$

We have to estimate, somehow, the values of $a(t,\nu)$ (amplitude calibration) and $\phi(t,\nu)$ (phase calibration) for each telescope. This approach is the one taken for most of the usual astronomical softwares (AIPS, *DIFMAP*, etc). Additionally, we also have to make further corrections, among other the contribution due to the ionosphere and the effects of the parallactic angle.

4.4.1 Amplitude calibration

The objective of the amplitude calibration is to convert the measured visibility amplitudes (without units) in flux densities (in Jy) and to remove errors produced by instrumental factors at the antennas (gains depend on antenna size, geometry, shape, surface geometry, pointing performance, receiver noise, sky noise, etc) and in the correlator.

The power P received by a radio telescope can be related with a quantity named *antenna temperature* (T_a), that is, the temperature of a black body that give us the same power that we are observing, by the relation

$$P = kT_a\Delta\nu, \tag{4.16}$$

where k is the Boltzmann constant and $\Delta\nu$ is the receiver bandwidth (Moran & Dhawan 1995).

When we observe in radio astronomy, we are interested on the flux density of the source that we are studying, namely, we are looking for the antenna temperature due to the target source (T_t). However, there are other factors that contribute, besides the source, to the antenna temperature measured (as amplifiers and receivers noise generated at each station or the presence of the atmosphere where the source has to be propagated until reaching the antenna). All these contributions that not proceed from the source are grouped in a term called *system temperature* (T_{sys}).

The antenna gain g, meanwhile, is defined by the relation between the flux of the observed source S (in Jy) and the corresponding antenna temperature (in K) (Bondi et al. 1994)

$$g = \frac{T_a}{S} \qquad \text{(in K/Jy)}. \tag{4.17}$$

Finally, the *system equivalent flux density* (SEFD), which is given by

$$\text{SEFD} = \frac{T_{sys}}{g} \tag{4.18}$$

is the measure, in flux unities (Jy), of the total temperature of the receiver (Moran & Dhawan 1995).

Therefore, the relationship between the amplitude of the correlation coefficient $\tilde{A}_{ij}$ measured by the antennas i and j and the corresponding calibrated visibility amplitude A_{ij}, is given by

$$A_{ij} = \tilde{A}_{ij} b \sqrt{(\text{SEFD})_i (\text{SEFD})_j} = \tilde{A}_{ij} b \sqrt{\frac{T^i_{sys} T^j_{sys}}{g_i g_j}}, \tag{4.19}$$

where T^i_{sys}, T^j_{sys}, g_i, and g_j are the system temperatures and the antenna gains for the antennas i and j, respectively (Cohen et al. 1975). The coefficient b has some necessary corrections as digitisation losses or corrections on the internal structure of the correlator (Cohen 1973).

Thereby, to carry out precise amplitude calibration of the observed visibilities frequent system temperatures for each station should be measured and accurate gain curves characterising the variation of the gain versus the elevation should be obtained.

4.4.2 Phase calibration. Fringe-fitting

There are several contributions affecting the value of the measured interferometric phase $\tilde{\theta}_{ij}(t,\nu)$, concretely:

$$\tilde{\theta}(t,\nu) = \tilde{\theta}_{geo}(t,\nu) + \tilde{\theta}_{ins}(t,\nu) + \tilde{\theta}_{atm}(t,\nu) + \tilde{\theta}_{ion}(t,\nu) + 2\pi n, \tag{4.20}$$

where $\tilde{\theta}_{geo}$ is the contribution due to the geometric delay τ between the two antennas, $\tilde{\theta}_{ins}$ is the contribution due to the antennas instrumentation, $\tilde{\theta}_{atm}$ and $\tilde{\theta}_{ion}$ are the contributions due to atmospheric and ionospheric effects, and $2\pi n$ is an integer number of cycles.

At the correlator, a model of (among other effects) earth rotation, atmosphere, and station clocks is applied to determine their contribution to the phase and remove them from the data. However, the model has a limited precision and residual delays remain that require additional treatment. The aim of the fringe-fitting is precisely that: to remove those residuals still present in the phases provided by the correlator (Beasley & Conway 1995).

We assume that through the (t,ν) interval solution of the fringe-fitting $a(t,\nu)$ and $|\mathrm{V}_{ij}|$ change slowly, so that they can be considered constant. Also we assume that the phases vary linearly with time and frequency, in this case, a first order expansion for the phase of the baseline i-j at the reference point (t_0,ν_0) within the relevant interval can be written as:

$$\tilde{\theta}_{ij}(t,\nu) = \phi_i(t_0,\nu_0) - \phi_j(t_0,\nu_0) + \theta_{ij}(t_0,\nu_0) + [\dot{\tau}_{ij}(t-t_0) + \tau_{ij}(\nu-\nu_0)], \tag{4.21}$$

where the quantities

$$\dot{\tau}_{ij} \equiv \left. \frac{\partial(\phi_i - \phi_i + \theta_{ij})(t,\nu)}{\partial t} \right|_{(t_0,\nu_0)} \tag{4.22}$$

and

$$\tau_{ij} \equiv \left. \frac{\partial(\phi_i - \phi_i + \theta_{ij})(t,\nu)}{\partial \nu} \right|_{(t_0,\nu_0)} \tag{4.23}$$

are called the fringe rate and delay, respectively. The visibility (Eq. 4.15) can be written as:

$$\begin{aligned} \tilde{V}_{ij}(t,\nu) &= a_i(t_0,\nu_0)a_j(t_0,\nu_0)A_{ij}(t_0,\nu_0)\times \\ &\times\ e^{i[\phi_i(t_0,\nu_0)-\phi_j(t_0,\nu_0)+\theta_{ij}(t_0,\nu_0)]}e^{i[\dot{\tau}_{ij}(t-t_0)+\tau_{ij}(\nu-\nu_0)]}. \end{aligned} \tag{4.24}$$

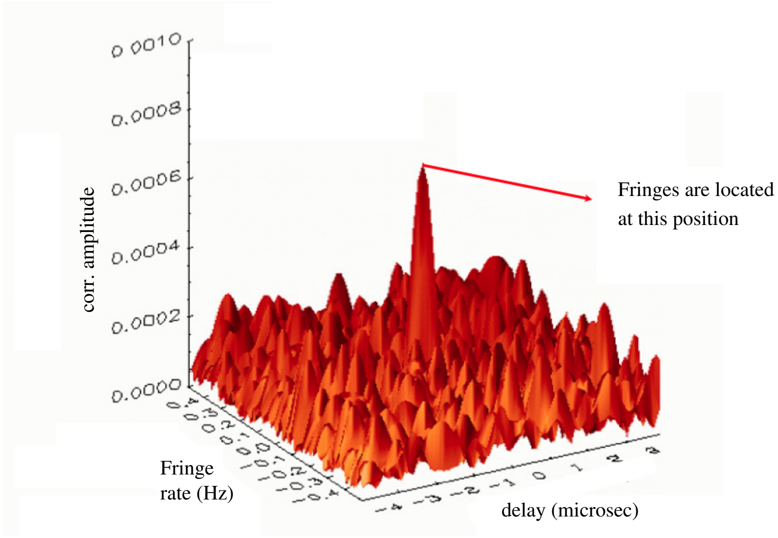

Fig. 4.5 Fourier transform of observed visibilities in delay, delay-rate space. The maximum amplitude indicates the corrected values of τ and $\dot{\tau}$. Credit: K. Kingham, United States Naval Observatory.

For a single baseline, the values of $\dot{\tau}_{ij}$ and τ_{ij} can be determined by searching the peak in the delay/delay-rate space of the Fourier transform of the expression 4.24. In essence, the fringes in the (t,ν) space will appear as an isolated point in the $(\tau,\dot{\tau})$ domain (see Fig. 4.5). Finally, the corrected, calibrated phases are extracted from the argument of the following expression:

$$\begin{aligned}\tilde{V}_{ij}(t,\nu)e^{-i[\dot{\tau}_{ij}(t-t_0)+\tau_{ij}(\nu-\nu_0)]} &= a_i(t_0,\nu_0)a_j(t_0,\nu_0)A_{ij}(t_0,\nu_0)\times \\ &\times \; e^{i[\phi_i(t_0,\nu_0)-\phi_j(t_0,\nu_0)+\theta_{ij}(t_0,\nu_0)]}. \end{aligned} \tag{4.25}$$

The contribution of $a_i(t_0,\nu_0)a_j(t_0,\nu_0)e^{i[\phi_i(t_0,\nu_0)-\phi_j(t_0,\nu_0)]}$ is removed in post-processing by self-calibration/hybrid mapping techniques.

Throughout the complete fringe-fitting process described above, we have assumed that the thermal noise term ϵ_{ij} is small, that is, in this baseline-based approach, a high SNR is needed for each baseline. To overcome this limitation for low SNR data, in the so-called *global fringe fitting* approach (Schwab & Cotton 1983; Walker 1989), it is possible to solve for antenna-dependent delays and delay-rates, if they are referred to a reference antenna, for which both values are set to zero. In practice, data from the higher SNR baselines are used to estimate the parameters of the weaker baselines, ensuring that both the delays and rates closure properties are preserved.

4.4.3 Ionospheric corrections

When the radio wave travels along the ionosphere, the signal is delayed due to the ionospheric plasma. This plasma is characterized, mainly, by its content of free electrons and ions. The total electron content (TEC) is a useful descriptive quantity for the ionosphere and it is defined as the number of electrons in a column along the ray path of one square meter cross section

$$\mathrm{TEC} = \int_0^{h_0} N \cdot dh, \tag{4.26}$$

where N is the number density of electrons, h is the coordinate of propagation of the wave, an h_0 is the value that represents the end of the ionosphere. TEC depends on multiple factors, such as local time, location, season, and solar activity. NASA's crustal dynamics data interchange system (CDDIS) provides, for each day and in the web page *ftp://cddis.nasa.gov/pub/gps/products/ionex/*, ionospheric models produced by five different groups: the Jet Propulsion Laboratory (JPL), the Center for Orbit Determination in Europe (CODE), the Geodetic Survey Division of Natural resources Canada (EMR), the ESOC Ionosphere Monitoring Facility (ESA), and the Technical University of Catalonia (UPC). These models consist in files in IONEX format containing a series of maps of the zenith total electron content of the ionosphere as a function of geographical latitude and longitude taken at different times.

The measurements of TEC are used to estimate the excess delay of a radio wave propagating through the ionosphere, $\Delta\tau_{\mathrm{ion}}$, that is given by

$$\Delta\tau_{\mathrm{ion}} = \pm\frac{\kappa}{c\nu^2} \cdot \mathrm{TEC}, \tag{4.27}$$

where $\kappa \approx 40.3$ ($\mathrm{m}^3\,\mathrm{s}^2$), c is the speed of light ($\mathrm{m\,s^{-1}}$), and ν the frequency (Hz). The positive sign refers to group delays and the negative sign for phase delays.

4.4.4 Parallactic angle

An altazimuth mounted antenna following the trajectory of a source produces a rotation seen by the source. This rotation is known as the parallactic angle $\chi(t)$ and is given by

$$\chi(t) = \arctan\left(\frac{\cos\lambda \sin(h(t))}{\sin\lambda\cos\delta - \cos\lambda\sin\delta\cos(h(t))}\right), \tag{4.28}$$

where δ is the source declination, λ is the latitude of the antenna, and $h(t)$ is the source hour angle (Taylor et al. 1999).

In VLBI observations, the large baselines between antennas pointing to the same source result in different parallactic angles. This difference introduces an additional phase that is necessary to correct, especially in polarization and phase-referencing experiments.

4.5 VLBI imaging

The calibrated amplitudes and phases of the interferometric visibility have an obvious astrophysical information. However, further processing and corrections are necessary to finally obtain an image of the radio source we have observed.

4.5.1 Closure phases

The interferometer phases are fairly noisy and highly dependent on instrumental effects and atmospheric conditions of each antenna. Therefore, it is essential for the correct calibration of the data, use amounts independent of phase shifts caused by the instruments and the atmosphere. These quantities are called *closure phases*.

After the fringe-fitting process, we obtain the following visibility phase on the baseline ij:

$$\varphi_{ij} \equiv \phi_i - \phi_j + \theta_{ij}. \tag{4.29}$$

In addition, we can consider that

$$\theta_{ij} = \vec{B}_{ij} \cdot \vec{S} + \psi_{ij}, \tag{4.30}$$

being $\vec{B}_{ij}$ the baseline vector between antennas i and j, $\vec{S}$ is the unit vector in the direction of the source, and ψ_{ij} is the contribution of the structure of the source.

The *closure phase* $C\sigma_{ijk}$ is formed by summing the "corrupted" visibility phases around a triangle of baselines ij, jk, and ki (Fig. 4.6):

$$\begin{aligned} C_{ijk} &= \varphi_{ij} + \varphi_{jk} + \varphi_{ki} \\ &= (\phi_i - \phi_j + \theta_{ij}) + (\phi_j - \phi_k + \theta_{jk}) + (\phi_k - \phi_i + \theta_{ki}) \\ &= \theta_{ij} + \theta_{jk} + \theta_{ki} \\ &= (\vec{B}_{ij} + \vec{B}_{jk} + \vec{B}_{ki}) \cdot \vec{S} + \psi_{ij} + \psi_{jk} + \psi_{ki} \\ &= \psi_{ij} + \psi_{jk} + \psi_{ki}. \end{aligned} \tag{4.31}$$

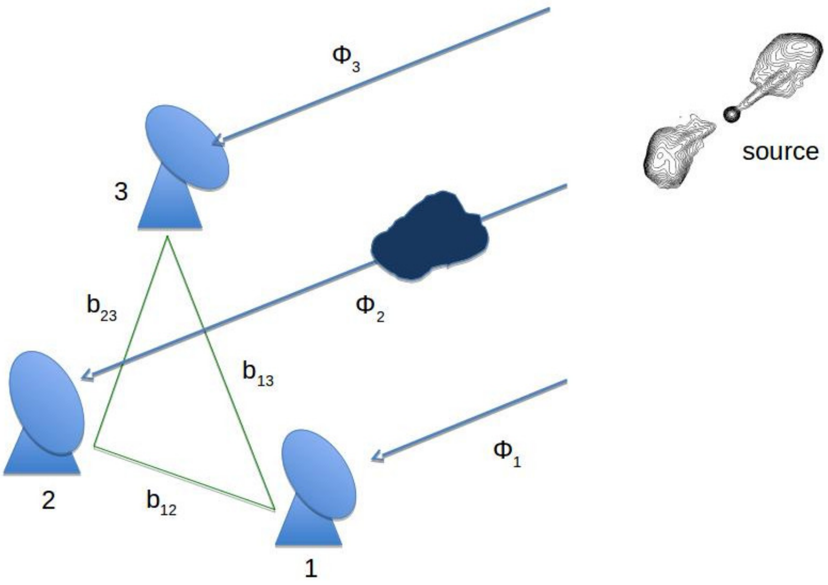

Fig. 4.6 A set of three baselines in an array that forms a triangle, which can be used to generate a phase closure variable.

As we can see, this quantity only depends on the structure of the source and is free from any instrumental effects. An important disadvantage of the closure phase is that it does not preserve the absolute position of the source, although it retains the relative positions between its components.

4.5.2 Hybrid mapping

Hybrid mapping is an iterative process that allows us to get the model that best fits the closure phase of visibilities. This process alternates two kind of iterations: image deconvolution and self-calibration.

In Section 4.2 we introduced the visibility function (Eq. 4.12), whose Fourier transform is the intensity $I(x,y)$. As we have a finite number of visibilities in the *uv plane*, to obtain a first model of the intensity of the source, we perform by the Fast Fourier Transform (FFT) algorithm, the discrete Fourier transform of the visibilities, $I_D(x,y)$

$$I_D(x,y) = \int_{-\infty}^{+\infty}\int_{-\infty}^{+\infty} W(u,v)V(u,v)S(u,v)e^{-i\frac{2\pi\nu}{c}(ux+vy)}dudv, \tag{4.32}$$

where $S(u,v)$ is known as *sampling function* and takes the value of one where there is visibility data and of zero in the rest of the *uv plane*. This expression $I_D(x,y)$ is called *dirty map* and relates the real emission of the source with the Fourier transform of the sampling function $B(x,y) = \int_{-\infty}^{+\infty} S(u,v) e^{-i\frac{2\pi\nu}{c}(ux+vy)} dudv$, called *dirty beam*. $W(u,v)$ is a weighting function that we can select to improve the results of the imaging process in different ways. This weighting function is used to account for the different density of visibilities in different parts of the *uv plane*, which is, in turn, divided in a grid of cells. There are two widely used weighting functions: natural and uniform. The natural weighting uses $W(u,v) = 1$, giving a constant weight to all visibilities, while uniform weighting uses $W(u,v) = 1/N$, where N is the number of data points within the cell. Natural weighting provides optimum sensitivity and good signal-to-noise ratio, but lower angular resolution, meanwhile uniform weighting provides better resolution, but a high rms image noise.

Deconvolution

Once we have the dirty map, we use an algorithm to compensate the insufficient coverage of the *uv plane*. The most generalized is called CLEAN and was developed by Jan Högbom in 1974. This algorithm looks for a model that best fits the visibility measurements we have by following these steps:

1. Search on the dirty map the position and the intensity of the point of maximum emission.
2. Subtract the dirty beam from the dirty map, centered on the coordinates of the point of maximum intensity and multiplied by a gain factor. CLEAN saves the coordinates of the point of maximum intensity and the gain value of the scaled intensity.
3. CLEAN repeats the above steps starting from the dirty map obtained on the last subtraction and reiterate this process until on the map only remains noise.
4. The algorithm has stored a set of coordinate values of maximum emission peaks and CLEAN gains. This set of values is convolved with an ideal beam, called *clean beam* (a Gaussian with FWHM equal to the FWHM of the central lobe of the dirty beam). We thus obtain the *clean map* of the source.

The CLEAN model is a representation of the source, but it is not the representation of the true distribution. Calibration errors and noise are still present.

Self-calibration

The model obtained with CLEAN will approach a little more to the real structure of the source, but improvements are possible. Self-calibration determines the antenna gains that minimize the differences between the model visibilities and the observed visibilities by minimizing the expression

$$\chi^2(g_1,\ldots,g_n) = \sum_{i<j}^{N} \omega_{ij} \left| V_{ij}^{obs} - g_i g_j^* V_{ij}^{mod} \right|^2, \tag{4.33}$$

where N is the number of antennas, g_i is the gain of the antenna i, ω_{ij} are the baseline weights (visibilities close to the noise level should receive lower weight than high signal-to-noise visibilities), and V_{ij}^{obs} and V_{ij}^{mod} are the observed and model visibilities for the pair (i, j), respectively.

The gain corrections are applied to the initial data set to obtain better calibrated visibilities and a new model is determined applying again the CLEAN algorithm to the corrected data set. With this new model visibilities, Eq. 4.33 is again used to obtain new corrections. This process is repeated until a convergent model is reached. It should be noted that the self-calibration process requires a sufficiently bright source to converge satisfactorily.

Phase-referencing

We have seen that in VLBI imaging the phase, delay, and delay rate residuals present in the data are estimated with fringe-fitting and self-calibration using the source data itself. However, when the source is weak, it is necessary information of an external source (known as *calibrator source*) that is transferred to the weaker source (known as *target source*) by a process called *phase-referencing*. This technique consists, basically, in i) during the observation, interleaving short scans of both the target and calibrator source, ii) estimating the antenna gains using only the calibrator data, iii) interpolating these gain solutions from the calibrator onto the target data.

The application of the phase-referencing technique requires the use of a calibrator source with specific characteristics, regarding flux density (the calibrator should be a strong source to obtain a good signal-to-noise in a short time), structure (the calibrator should be an unresolved source), and position (the calibrator should be nearby in angle to the target source that the propagation effects are indistinguishable).

Chapter 5

Dynamical masses of the low-mass stellar binary AB Doradus B

This chapter is based on the publication appeared in the journal Astronomy and Astrophysics, 578, A16, 2015:

Dynamical masses of the low-mass stellar binary AB Doradus B

R. Azulay, J.C. Guirado, J.M. Marcaide, I. Martí-Vidal, E. Ros, D. L. Jauncey, J.-F. Lestrade, R. A. Preston, J. E. Reynolds, E. Tognelli, P. Ventura

Abstract

Context: AB Doradus is the main system of the AB Doradus moving group. It is a quadruple system formed by two widely separated binaries of pre-main-sequence (PMS) stars: AB Dor A/C and AB Dor Ba/Bb. The pair AB Dor A/C has been extensively studied and its dynamical masses have been determined with high precision, thus making AB Dor C a benchmark for calibrating PMS stellar models. If the orbit and dynamical masses of the pair AB Dor Ba/Bb could be determined, they could play a similar role to that of AB Dor C in calibrating PMS models, and would also help to better understand the dynamics of the whole AB Doradus system.
*Aims:*We aim to determine the individual masses of the pair AB Dor Ba/Bb using VLBI observations and archive infrared data as part of a larger program that monitors binary systems in the AB Doradus moving group.
Methods: We observed the system AB Dor B between 2007 and 2013 with the Australian Long Baseline Array (LBA) at a frequency of 8.4 GHz in phase-reference mode.
Results: We detected, for the first time, compact radio emission from both stars in the binary, AB Dor Ba and AB Dor Bb. This result allowed us to determine the orbital parameters of both the relative and absolute orbits and, consequently, their individual

dynamical masses: 0.28±0.05 $M_{\odot}$ and 0.25±0.05 $M_{\odot}$, respectively.

Conclusions: Comparisons of the dynamical masses with the prediction of PMS evolutionary models show that the models underpredict the dynamical masses of the binary components Ba and Bb by 10−30% and 10−40%, respectively, although they still agree at the 2-σ level. Some of the stellar models considered favor an age between 50 and 100 Myr for this system, while others predict older ages. We also discuss the evolutionary status of AB Dor Ba/Bb in terms of an earlier double-double star scenario that might explain the strong radio emission detected in both components.

5.1 Introduction

Stellar evolution models are used to predict fundamental parameters of the stars, such as their mass. The estimates from mass-luminosity theoretical relationships are not in agreement for the particular case of pre-main-sequence (PMS) stars with masses < 1.2 $M_{\odot}$. Either more accurate observations or revised models are needed. As reported in Azulay et al. (2014), a VLA/VLBI program to detect binary stars with substantial emission at radio wavelengths is underway. This program focuses on stars members of the AB Doradus moving group, AB Dor-MG (Zuckerman et al. 2004), which includes the already studied pairs AB Dor A/C (Guirado et al. 2006) and HD 160934 A/c (Azulay et al. 2014).

Located at a distance of ~15 pc (Guirado et al. 2006), the stellar system AB Dor has a pair of binaries, AB Dor A and AB Dor B, separated by ~9″. The K0V star AB Dor A, the main star of the system, is an active star with detectable emission at all wavelengths. In particular, it has strong radio emission (Guirado et al. 1997) generated by the amplification of the magnetic field by a dynamo effect caused by its rapid rotation (0.51 days). This star has a low-mass companion, AB Dor C (0.090 $M_{\odot}$), whose study is important in order to calibrate the stellar evolution models of young low-mass stars (Close et al. 2005).

The other binary of the AB Doradus system is AB Dor B (=Rossiter 137 B), which consists of two components, AB Dor Ba and AB Dor Bb, with spectral types M5 and M5-6 (Close et al. 2007), respectively. These components are separated by an angular distance of ~0.″06 (Guirado et al. 2006; Janson et al. 2007). The combined system shows a high rotation rate with a period of 0.38 days (Lim 1993; Wolter et al. 2014) and displays strong radio emission detected both by the Australian Telescope Compact Array (ATCA; Lim 1993; Wolter et al. 2014) and the Australian VLBI Network (Guirado et al. 2006; Azulay et al. 2015). Close et al. (2007) and Wolter et al. (2014) report information on the relative orbit from NIR VLT observations at H and K bands. The latter authors estimated a value of the sum of the masses of the components Ba and Bb of $0.69^{+0.02}_{-0.24}$ $M_{\odot}$ that is somewhat larger than the

Table 5.1 Journal of observations of AB Dor B

Date (Epoch)	Array configuration[a]	UT Range	Beam size [mas]	P.A. [°]
11 Nov 2007 (2007.863)	At, Cd, Ho, Mp, Pa, Hh	10:00 - 22:00	3.04×1.18	−2.4
25 Oct 2010 (2010.816)	At, Cd, Ho, Mp, Pa	11:00 - 23:00	2.96×2.76	74.3
16 Aug 2013 (2013.625)	At, Cd, Ho, Mp, Pa, Hh, Ti, Ww	15:00 - 03:00	2.61×1.05	0.8

Notes. [a]: At: Australia Telescope Compact Array, Cd: Ceduna, Ho: Hobart, Mp: Mopra, Pa: Parkes, Ti: DSS43 - NASA's Deep Space Network Tidbinbilla, Ww: Warkworth, Hh: Hartebeesthoek

model-dependent estimates from Janson et al. (2007) (0.13−0.20 and 0.11−0.18 $M_\odot$ for Ba and Bb, respectively).

An important point of debate is the age of the AB Doradus system, which has not been determined with sufficient accuracy and presents different estimates in different publications: from 40-50 Myr (Zuckerman et al. 2004; López-Santiago et al. 2006; Guirado et al. 2011) to 50-100 Myr (Nielsen et al. 2005; Janson et al. 2007; Boccaletti et al. 2008) and 100-140 Myr (Luhman et al. 2005; Ortega et al. 2007; Barenfeld et al. 2013). The determination of the age of the AB Doradus system is fundamental to calibrating the evolution models of PMS stars.

In this chapter we report the results of three epochs of VLBI observations of AB Dor B, leading to the discovery of radio emission from both components, the determination of the dynamical masses for the individual components, and their comparisons with theoretical models. We also discuss a possible evolutionary scenario for AB Dor Ba and AB Dor Bb in terms of an earlier quadruple system that evolved to its present state via Kozai cycling and tidal friction (Mazeh & Shaham 1979; Fabrycky & Tremaine 2007).

5.2 Observations and data reduction

We carried out three epochs of observations with the Long Baseline Array (LBA), the Australian VLBI Network, between 2007 and 2013 (see Table 5.1). Each observation lasted 12 hours at the frequency of 8.4 GHz. Both RCP and LCP polarizations were recorded with a rate of 1024 Mbps (two polarizations, eight subbands per polarization, 16 MHz per subband, 2 bits per sample), except at Hobart and Ceduna, with a recording rate of 512 Mbps (two polarizations, four subbands per polarization, 8 MHz per subband, 2 bits per sample). We used the phase-reference technique, interleaving scans of the ICRF[1]-defining source

---

[1] International Celestial Reference Frame. http://hpiers.obspm.fr/icrs-pc/

Table 5.2 Circular Gaussian fits corresponding to the VLBI maps of the components of AB Dor B

Epoch	Component	Flux (mJy)	Diameter (mas)
2007.863	Ba	0.82 ± 0.18	2.81 ± 0.10
	Bb	0.88 ± 0.17	3.04 ± 0.06
2010.816	Ba	1.39 ± 0.08	2.92 ± 0.02
	Bb	0.60 ± 0.11	2.02 ± 0.13
2013.625	Ba	0.63 ± 0.07	1.62 ± 0.07
	Bb	0.92 ± 0.07	1.74 ± 0.02

BL Lac PKS 0516−621 and the star AB Dor B (separated by 3.6°). The observation sequence target-calibrator-target lasted about four minutes.

We reduced the data using the Astronomical Image Processing System (AIPS) program, of the National Radio Astronomy Observatory (NRAO), following standard procedures: (i) we calibrated the visibility amplitude using system temperatures and antenna gains; (ii) we removed the ionospheric contribution (using GPS-based Global Ionospheric Maps[2]); and corrected the parallactic angle; (iii) we performed a fringe-search on the calibrator to remove residual contributions to the phases; and (iv) we interpolated these solutions from the calibrator onto the star data.

We imaged the radio sources with the program *DIFMAP* (Shepherd et al. 1994) and cross-checked the results with the *IMAGR* task in AIPS. To re-scale the visibility amplitudes of the calibrator PKS 0516−621, known to be a variable source (Sadler et al. 2006; Murphy et al. 2010), we used the 8.4 GHz flux density values obtained from ATCA measurements of this calibrator taken at the same time as our LBA observations (0.85, 1.40, and 1.50 Jy for epochs 2007.863, 2010.816, and 2013.625, respectively). We iterated amplitude and phase self-calibrations with deconvolutions using the CLEAN algorithm to finally obtain the uniformly weighted maps of PKS 0516−621 (see Fig. 5.1). For each epoch, this iterative procedure allowed us to determine both the amplitude scaling corrections and self-calibrated phase for each telescope. Back to the AIPS program, these corrections were then interpolated and applied to the AB Dor B data. The phase-referenced naturally weighted images of AB Dor B are shown in Fig. 5.2. We note that in this phase-reference mapping process the positional information of AB Dor B with respect to the external quasar is conserved, thus relating the position of AB Dor B to the ICRF.

---

[2] http://cddis.nasa.gov/cddis.html

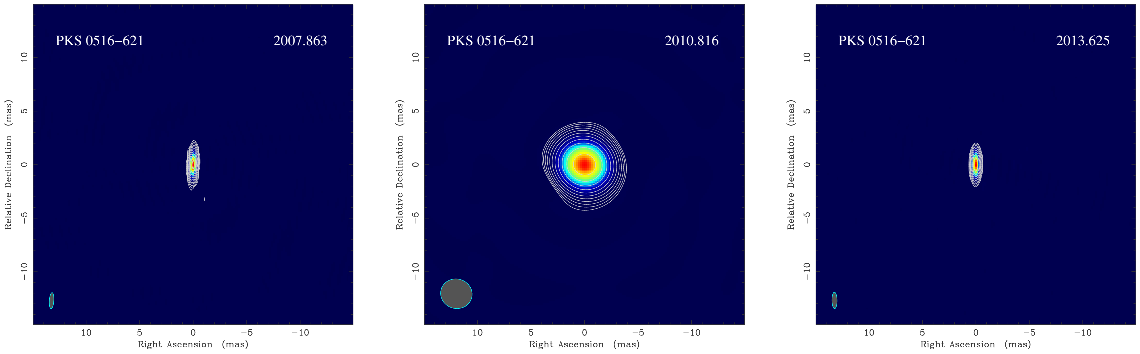

Fig. 5.1 Contour images of the calibrator PKS 0516−621 at the three LBA epochs. In each map, the lowest contour level corresponds to 3 times the statistical root-mean-square (3, 1.5, and 3 mJy beam^{-1}) with a scale factor between contiguous contours of $\sqrt{3}$. The peak flux densities in the images are, respectively, 0.89, 1.54, and 1.44 Jy beam^{-1}. We note that the second epoch has only intra-Australian baselines and therefore a lower resolution. See Table 5.1.

5.3 Results

5.3.1 Maps of AB Dor Ba/Bb

At each of the three observing epochs, two sources are clearly distinguishable in Fig. 5.2; we identify both spots with the components Ba and Bb previously seen in NIR images (Janson et al. 2007). We determined the flux and position of both components from a circular Gaussian least-squares fit (see Table 5.2). Both components appear unresolved for all three epochs. These are the first VLBI images of AB Dor B where we confirm that both components are compact and strong radio emitters. Previous studies (Lim 1993; Wolter et al. 2014) already found the system to have an intense radio emission, which combined with the high X-ray luminosity, close to the saturation limit for active late-type stars, confirm the strong magnetic activity of this system. Our radio maps show that each component Ba and Bb should retain a high rotation rate to maintain such intense activity. The AB Dor B IR spectral analysis reported in Wolter et al. (2014) is compatible with two rapid rotators (although a model based on a single high-rotation star is not excluded). Using the fluxes and sizes listed in Table 5.2, we derived a mean radio luminosity for Ba and Bb of $L_{\rm R} = 2.7 \times 10^{14}$ erg Hz^{-1} s^{-1}, similar to other radio star members of the AB Dor-MG, indicating that gyrosynchrotron emission originating at the stellar corona is the responsible mechanism for the radio emission.

For a proper astrometric analysis, we still need to identify the components Ba and Bb, as labeled by Janson et al. (2007) in their NIR images, in each of our images of AB Dor B. These authors selected component Ba to be the brightest one; however, the flux density of both stars is very variable at radio wavelengths (see Table 5.2) making an identification under

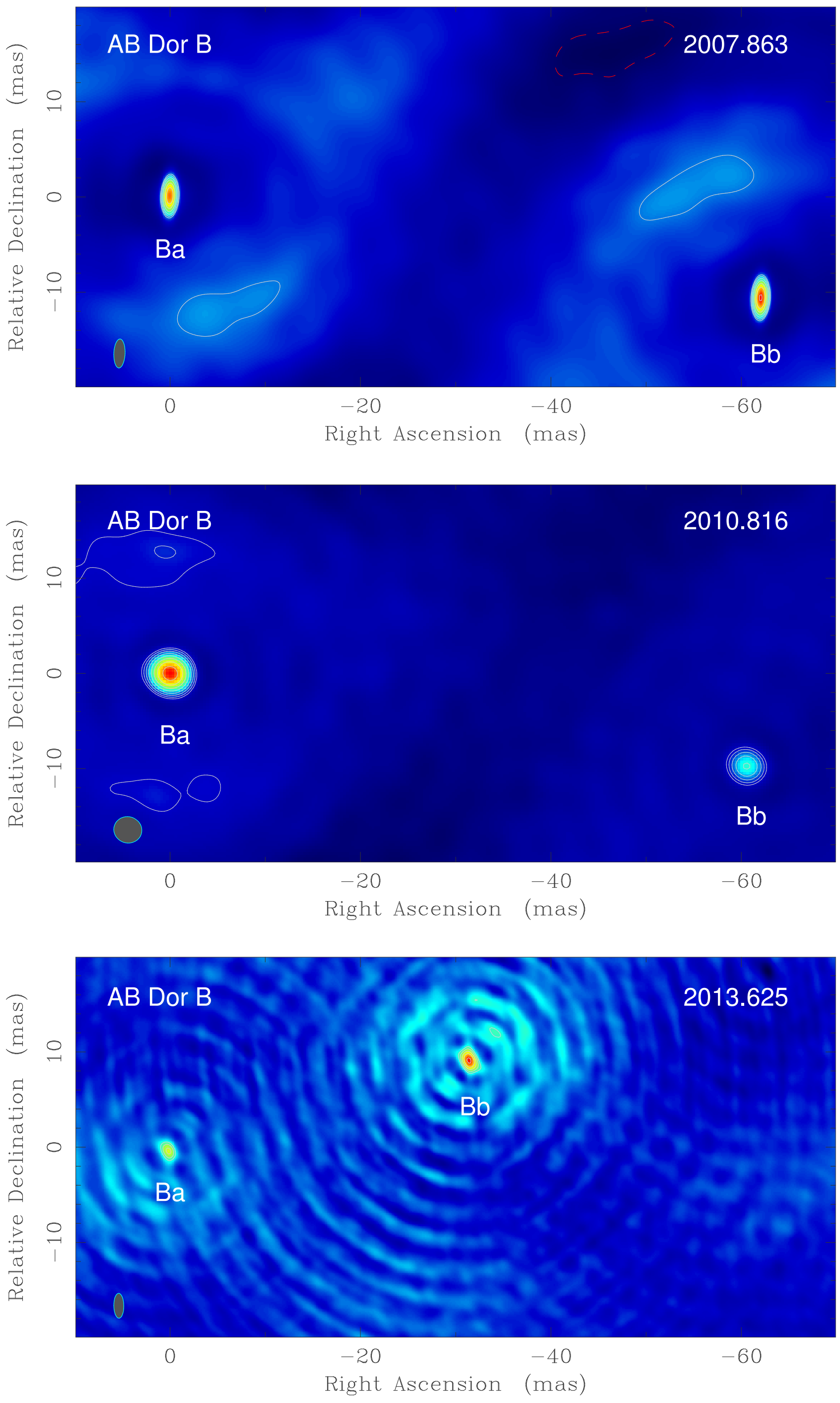

Fig. 5.2 Clean maps of the binary AB Dor B at the three LBA epochs. In each map, the lowest contour level corresponds to 3 times the statistical root-mean-square (0.08, 0.19, and 0.12 mJy beam^{-1}) with a scale factor between contiguous contours of $\sqrt{2}$. The peak flux densities in the images are, respectively, 0.86, 1.25, and 0.89 mJy beam^{-1}. For image parameters see Table 5.2. In all the maps we have centered the position of AB Dor Ba at the origin. Absolute positions of both Ba and Bb are in Table 5.3.

the same criteria difficult. To break this ambiguity, and based on the similar relative position of components Ba and Bb in both the NIR and radio images, we selected the easternmost component of the radio maps to be Ba. This choice was confirmed to be correct after the analysis of the orbital motion (see Sect. 5.3.2). It must be noted that the appropriate registration of Ba and Bb through the three epochs is guaranteed by the use of the quasar PKS 0516−621 as an external astrometric reference.

5.3.2 Orbit determination of AB Dor Ba/Bb

To estimate the orbital elements of AB Dor Ba/Bb, we used the positions of AB Dor Ba/Bb resulting from the astrometric analysis of our three LBA observations, both the relative positions (as measured directly on the maps shown in Fig. 5.2) and the absolute positions (in turn referenced to the position of the quasar PKS 0516−621). We included the NIR relative positions available in the literature (Wolter et al. 2014, and references therein) in our fit. We complemented our data sets with the absolute positions reported in Guirado et al. (2006) and re-interpreted here. These authors made a first attempt to estimate the orbital elements with LBA epochs ranging from 1992 to 1996, but their least-squares analysis did not converge to any plausible solution. A possible reason for this non-convergence could be the misidentification of the only component detected, wrongly associated with AB Dor Ba at all epochs. Preliminary fits of the Guirado et al. (2006) positions along with the new ones presented in this chapter show that only the positions at epochs 1992.685 (corresponding to Bb) and 1993.123 (corresponding to Ba) are compatible with the new LBA data. Accordingly, only those positions are included in our fit. The rest of the positions of AB Dor Ba/Bb in Guirado et al. (2006) are therefore not included in our analysis. Table 5.3 summarizes all the positions used in this work.

To find the astrometric and Keplerian parameters of the AB Dor B system, we selected a non-redundant data set from the positions shown in Table 5.3. In practice, in our fit we combined the absolute positions of AB Dor Bb and all relative positions of AB Dor Bb to AB Dor Ba. The reason for this choice is that the absolute orbit of AB Dor Bb and the relative orbit constructed using AB Dor Ba as reference (Bb−Ba) are identical, except for their semimajor axes, which are related by the mass ratio. An equivalently valid choice would have been a combination of absolute data of Ba and relative data constructed as Ba−Bb. We note that other combinations of absolute and relative data would have produced an extra difference of π radians in the longitude of the periastron (ω) between the absolute and relative orbits, which would have complicated our orbit analysis (see below). We used a least-squares fit approach similar to that described in Guirado et al. (2006), but slightly improved to deal with relative data, which we outline here.

We define the absolute position of AB Dor Bb ($\alpha_{\rm Bb}, \delta_{\rm Bb}$) at epoch t through the expressions

$$\begin{aligned}\alpha_{\rm Bb}(t) = \alpha(t_0) + \mu_\alpha(t-t_0) + Q_\alpha(t-t_0)^2 + \pi P_\alpha + \\ S_\alpha(t,A,B,F,G,P,e,T_0) \\ \delta_{\rm Bb}(t) = \delta(t_0) + \mu_\delta(t-t_0) + Q_\delta(t-t_0)^2 + \pi P_\delta + \\ S_\delta(t,A,B,F,G,P,e,T_0),\end{aligned} \tag{5.1}$$

where t_0 is the reference epoch, μ_α and μ_δ are the proper motions in each coordinate, Q_α and Q_δ are the secular perspective accelerations in each coordinate (i.e., time variation of the proper motions), π is the parallax, P_α and P_δ are the parallax factors (Green 1985), and S_α and S_δ are the absolute orbital motions of AB Dor Bb in α and δ, respectively. The acceleration terms are intended to model the long-term expected curvature of the sky trajectory of AB Dor B due to the gravitational pull of AB Dor A, 9″ away (see Guirado et al. 2006). We used the Thieles-Innes elements (A,B,F,G), which are combinations of the semimajor axis of the absolute orbit $a_{\rm Bb}$, the inclination i, the longitude of the ascending node Ω, and the longitude of periastron ω (see Appendix B). The three remaining non-linear parameters are the period P, the eccentricity e, and the time of periastron passage T_0.

Similarly, the relative positions ($\alpha_{\rm rel}, \delta_{\rm rel}$, constructed as Bb−Ba) at epoch t' (not necessarily different from t) are included in the fit through the expressions

$$\begin{aligned}\Delta\alpha_{\rm rel}(t') = S_\alpha(t',q,A,B,F,G,P,e,T_0) \\ \Delta\delta_{\rm rel}(t') = S_\delta(t',q,A,B,F,G,P,e,T_0),\end{aligned} \tag{5.2}$$

where q is the ratio between the semimajor axes of the relative and absolute orbit, $a_{\rm rel}/a_{\rm Bb}$. We note that q behaves as a scale factor between the absolute and relative orbit, both sharing all the orbital elements but the semimajor axes (provided that the absolute and relative data sets have been chosen appropriately, as explained above). Accordingly, the true Thieles-Innes constants of the relative orbit can be written as (qA, qB, qC, qG), so that q remains as the only additional free parameter in our fit when adding the relative orbit data. Given the definition of both data types, the χ^2 to be minimized is

$$\begin{aligned}\chi^2 = \sum_{i=1}^{N} \frac{(\alpha_{\rm Bb}(t_i) - \hat{\alpha}_{\rm Bb}(t_i))^2}{\sigma^2_{\alpha_{\rm Bb}}(t_i)} + \sum_{i=1}^{N} \frac{(\delta_{\rm Bb}(t_i) - \hat{\delta}_{\rm Bb}(t_i))^2}{\sigma^2_{\delta_{\rm Bb}}(t_i)} + \\ \sum_{i=1}^{M} \frac{(\Delta\alpha_{\rm rel}(t'_i) - \Delta\hat{\alpha}_{\rm rel}(t'_i))^2}{\sigma^2_{\alpha_{\rm rel}}(t'_i)} + \sum_{i=1}^{M} \frac{(\Delta\delta_{\rm rel}(t'_i) - \Delta\hat{\delta}_{\rm rel}(t'_i))^2}{\sigma^2_{\delta_{\rm rel}}(t'_i)},\end{aligned} \tag{5.3}$$

Table 5.3 Compilation of astrometric measurements for the AB Dor B system

		Relative positions AB Dor Bb − AB Dor Ba		
Epoch	Instrument	$\Delta\alpha$ (mas)	$\Delta\delta$ (mas)	Reference
2004.091	VLT (IR)	−56.8±3.0	−33.1±3.0	(1)
2005.019	"	−64.6±3.0	−27.4±3.0	(1)
2005.909	"	−66.7±3.0	−4.0±3.0	(1)
2008.650[a]	"	9.6±3.0	−16.4±3.0	(1)
2008.855	"	−61.3±3.0	−9.9±3.0	(1)
2008.967	"	−61.5±3.0	−24.8±3.0	(1)
2009.003	"	−57.3±3.0	−26.7±3.0	(1)
2009.131	"	−45.6±3.0	−32.7±3.0	(1)
2007.863	LBA (radio)	−62.0±0.3	−10.5±0.7	(2)
2010.816	"	−60.3±1.5	−9.7±1.4	(2)
2013.625	"	−31.3±0.4	9.3±0.9	(2)
		Absolute positions AB Dor B (LBA)		
Epoch	Component	RA (h m s)	Dec (° ′ ″)	
1992.685	Bb	5 28 44.41973 ± 0.00060	−65 26 47.0047 ± 0.0021	(3)
1993.123	Ba	5 28 44.40441 ± 0.00080	−65 26 46.9869 ± 0.0028	(3)
2007.863	Ba	5 28 44.57761 ± 0.00008	−65 26 45.1002 ± 0.0010	(2)
	Bb	5 28 44.56766 ± 0.00008	−65 26 45.1107 ± 0.0010	(2)
2010.816	Ba	5 28 44.61098 ± 0.00019	−65 26 44.7132 ± 0.0008	(2)
	Bb	5 28 44.60130 ± 0.00014	−65 26 44.7229 ± 0.0008	(2)
2013.625	Ba	5 28 44.63954 ± 0.00015	−65 26 44.2920 ± 0.0009	(2)
	Bb	5 28 44.63453 ± 0.00013	−65 26 44.2827 ± 0.0008	(2)

Notes. [a] In Wolter et al. (2014) this position was instead considered to be an upper bound of 19 mas for the separation of Ba/Bb at 2008.855. (1) Wolter et al. (2014); (2) This work; (3) Guirado et al. (2006). The standard deviation of the relative position corresponds to the uncertainty based on the signal-to-noise ratio of the peaks of brightness of AB Dor Ba and Bb. The absolute positions were obtained with reference to the IERS coordinate of the external quasar PKS 0516−621 ($\alpha = 5^{h}16^{m}44^{s}.926178, \delta = -62^{\circ}\,7'\,5''.38930$). The standard deviation of the absolute position includes, in addition to the uncertainty of their respective peaks of brightness, the contribution of the propagation media and the reference source structure.

where N is the number of absolute positions, M the number of relative positions, σ the corresponding standard deviations, and the circumflexed quantities are the theoretical positions derived from the *a priori* values of the astrometric and orbital parameters. We have used the Levenberg-Marquardt algorithm (L-M; e.g., Press et al. 1992) to minimize the χ^2. Like other methods used to find minima in a non-linear χ^2 space, the efficiency of the L-M algorithm is much improved if good *a priori* values are used for the orbital elements. In our particular case, exploration of the relative orbit data yields a reasonable initial value for the period: as seen in Table 5.3, the two first NIR positions are similar, indicating that the time difference between both epochs, nearly one year, could be a promising initial value for the period. In addition, the separation and the position angle in the first two LBA epochs (2007.863 and 2010.816) are almost coincident, with a difference of less than two milliarcseconds. This strongly suggests that the time difference between the two LBA epochs (2.95 years) should be approximately an integer number of the true orbital period. If we assume that three complete orbits have elapsed between the two epochs, the orbital period would be 0.98 yr, coincident with the estimate made from the relative infrared data. The use of an *a priori* value for the period of 1 yr did facilitate the convergence of the L-M algorithm. Of course, the previous argumentation is also valid for shorter periods as long as $P \sim 1/n$ yr, with n being an integer number; however, no convergence is found in our fit for periods with $n \geq 2$.

The set of orbital parameters that produces a minimum in the χ^2 (1.2) is shown in Table 5.4. Plots of the relative and absolute orbits are shown in Figs. 5.3 and 5.4, respectively. These parameters coincide with those of Wolter et al. (2014) to within their standard deviations (except for Ω, with a difference of $\sim \pi/2$, which may reflect a quadrant ambiguity). The sum of the masses of the system can be calculated from $a_{\rm rel}$ and the period P using Kepler's Third Law ($m_{\rm Ba} + m_{\rm Bb} = a^3_{\rm rel}/P^2$), which resulted in 0.53±0.05 $M_\odot$, somewhat lower, but within uncertainties, than the Wolter et al. (2014) estimate of $0.69^{+0.02}_{-0.24}\,M_\odot$. More importantly, since our data also provide the semimajor axis of the absolute orbit of AB Dor Bb, $a_{\rm Bb}$, we can also calculate the mass of the component Ba, $m_{\rm Ba}$, using Kepler's third law in the form $m^3_{\rm Ba}/(m_{\rm Ba} + m_{\rm Bb})^2 = a^3_{\rm Bb}/P^2$. This yields a value of $m_{\rm Ba}$=0.28±0.05 $M_\odot$, with the uncertainty calculated from the propagation of the standard deviations of the semimajor axis $a_{\rm Bb}$, the period P, and $m_{\rm Ba} + m_{\rm Bb}$. Since we also have the absolute data of AB Dor Ba, we can estimate, independently of the previous fit, a value of $m_{\rm Bb}$ (i.e., not just the difference between mass sum and $m_{\rm Ba}$). To this end, we repeated the fit described throughout this section but using the absolute positions of AB Dor Ba and the relative positions constructed as Ba-Bb. As explained above, this is an equivalent fit to the previous one, except that it provides an estimate of $a_{\rm Ba}$ instead of $a_{\rm Bb}$. Again, using Kepler's Third Law, now with $a_{\rm Ba}$, we obtain a value of $m_{\rm Bb}$=0.25±0.05 $\rm M_\odot$, this estimate being largely independent of $m_{\rm Ba}$ and the total mass.

Regarding the astrometric parameters in Table 5.4, we note that the long-term orbit of the pair AB Dor B around AB Dor A is reflected in the values of the perspective acceleration; solving for Q_α and Q_δ reduced the rms of the residuals by a factor of three. The magnitude of the acceleration can be easily reproduced from the simple expression (circular orbit) $(2\pi/P_{\rm AB})^2 \times r_{\rm AB}$, taking the A/B distance $r_{\rm AB} = 9.22''$ at the reference epoch (2000.0) and assuming reasonable values of the period of B around A, $P_{\rm AB}$ (∼2000 yr; within the plausible orbits defined in Guirado et al. 2006).

Finally, as seen in Figs. 5.3 and 5.4, the orbit of the pair in AB Dor B is not fully covered. However, the orbital elements in Table 5.4 are satisfactorily determined. This apparent contradiction may be explained in two ways. First, the so-called Eggen's effect (Lucy 2014), which predicts that for poorly covered orbits, the quantity a^3/P^2 has little variation for the values of the parameters (a, P) that minimize the χ^2 defined in Eq. 5.3. We note that a^3/P^2 is proportional to the star masses, and therefore sensitive to any trace of orbital motion present in one of the components of the binary. Second, we have a precise *a priori* value for the orbital period, which when combined with the previous effect leads to a reliable estimate of the semimajor axis, greatly constraining the rest of the orbital elements.

5.4 Discussion

5.4.1 Stellar evolution models for PMS stars

The measurements of dynamical masses are essential in order to check PMS stellar evolution models. The mass is the most important stellar parameter, but determinations of the luminosity and the temperature are also necessary in order to calibrate the theoretical models. Extensive description and comparison between existing stellar models can be seen in Hillenbrand & White (2004).

We have considered isochrones and isomasses corresponding to the PMS models of Baraffe et al. (1998; BCAH98), Siess et al.(2000; S00), Montalbán & D'Antona (2006; MD06), and Tognelli et al. (2011, 2012; TDP12). A metallicity value of [Fe/H]= 0.0 has been adopted as the average value of the AB Doradus moving group was reported to be [Fe/H]=0.02 ± 0.02 (Barenfeld et al. 2013). All the quoted models provide theoretical masses for stars down to 0.1 $\rm M_\odot$, but for different mass spacing. Low convection efficiency (i.e., mixing length parameter $\alpha_{\rm ML}$ = 1.0), which optimizes the comparison with our data, have

Table 5.4 Estimates of the astrometric and orbital parameters of AB Dor B[a,b]

Parameter	Value
α_0 (h m s):	5 28 44.48396 ± 0.00022
δ_0 (° ′ ″):	−65 26 46.0573 ± 0.0013
μ_α (s yr^{-1}):	0.01054 ± 0.00012
μ_δ (arcsec yr^{-1}):	0.1287 ± 0.0005
Q_α (s yr^{-2}):	0.000008 ± 0.000001
Q_δ (arcsec yr^{-2}):	−0.00010 ± 0.00005
π (arcsec)[c]:	0.0664 ± 0.0005
P (yr):	0.986 ± 0.008
$a_{\rm rel}$ (″):	0.052 ± 0.002
$a_{\rm Ba}$ (″):	0.028 ± 0.002
$a_{\rm Bb}$ (″):	0.025 ± 0.002
e:	0.6 ± 0.1
i (°):	121 ± 5
$\omega_{\rm Bb}$ (°)[d]:	54 ± 20
Ω (°):	270 ± 15
T_0:	2003.68 ± 0.05
$m_{\rm Ba}$ (M$_\odot$):	0.28 ± 0.05
$m_{\rm Bb}$ (M$_\odot$):	0.25 ± 0.05

Notes. [a] The reference epoch is 2000.0. [b] The number of degrees of freedom of the fit is 14; the minimum value found for the reduced χ^2 is 1.2. [c] We note that our parallax estimate is more accurate than the *Hipparcos* value given for AB Dor A and still compatible. [d] For the absolute orbit of AB Dor Ba $\omega_{\rm Ba} = \omega_{\rm Bb} + \pi$.

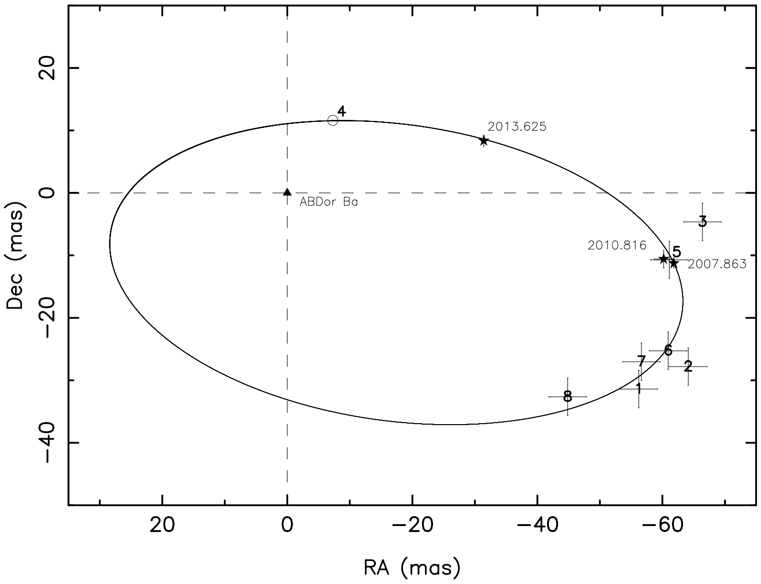

Fig. 5.3 Relative orbit for the binary AB Dor Bb using the orbital elements in Table 5.4 (with $a_{\rm rel}$). The AB Dor Ba component is indicated by the triangle at the origin. Star symbols and epochs correspond to the VLBI data. For the sake of clarity, the NIR points are marked with numbers, following a chronological order which corresponds with their entries in Table 5.3. A prediction of the relative position at epoch 2008.605 is shown as an empty circle, indicating that the upper bound of 19 mas suggested by Wolter et al. (2014) is fully accomplished.

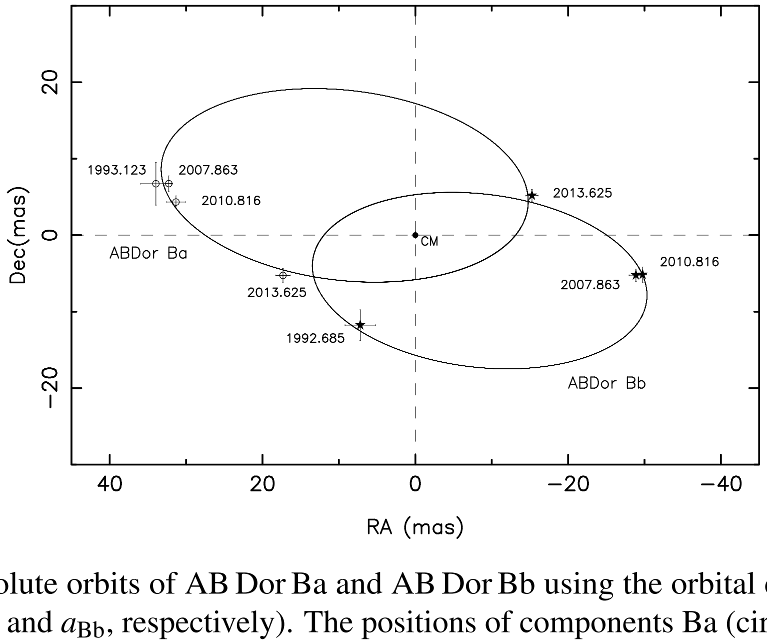

Fig. 5.4 Absolute orbits of AB Dor Ba and AB Dor Bb using the orbital elements in Table 5.4 (with $a_{\rm Ba}$ and $a_{\rm Bb}$, respectively). The positions of components Ba (circles) and Bb (star symbols) are marked along with their respective epochs. The center of mass (CM) of the system is placed at the origin.

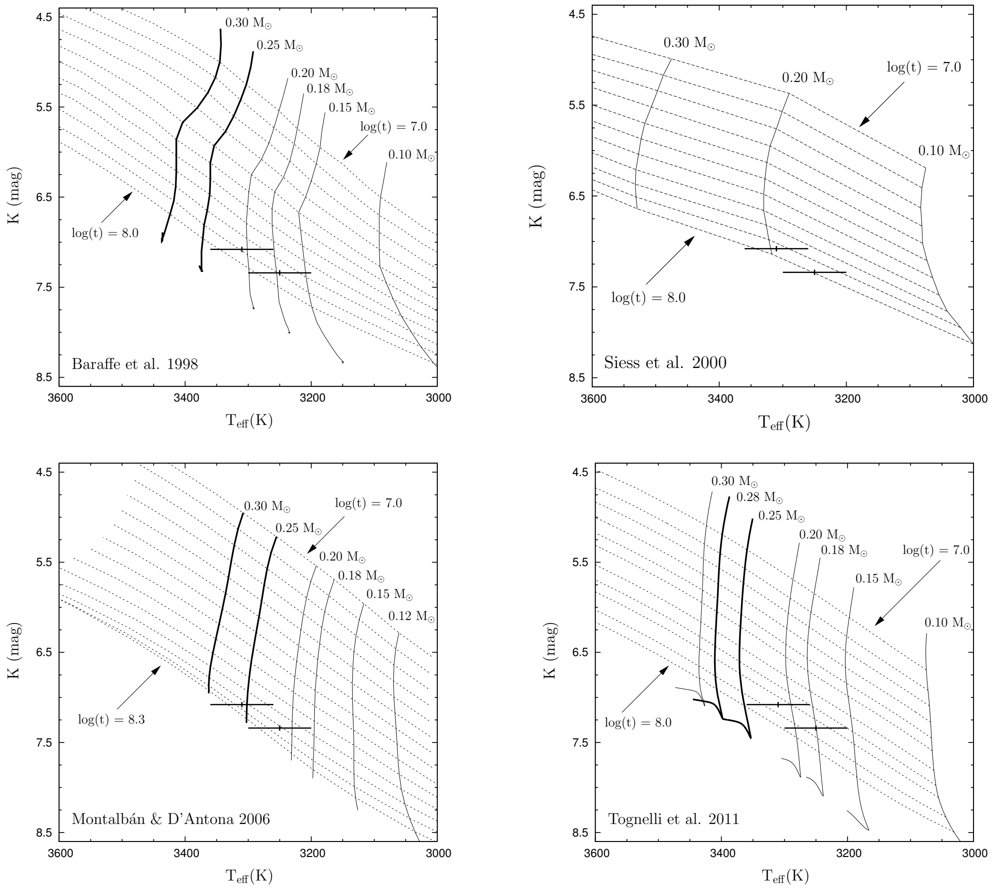

Fig. 5.5 Comparison of AB Dor B components with some PMS theoretical models (Baraffe et al. 1998, *top left*; Siess et al. 2000, *top right*; Montalán & D'Antona 2006, *bottom left*; Tognelli et al. 2011; *bottom right*). For each model isomasses (solid lines) and isochrones (dashed lines) are plotted. We highlight the nearest tracks available corresponding to our dynamical mass values. The theoretical masses are consistent with our dynamical estimates just at the extreme of their uncertainties.

been used in the case of the BCAH98, MD06, and TDP12 models. For the S00 models, tracks are available only for solar calibration, with $\alpha_{\mathrm{ML}} = 1.61$.

In addition to the convection treatment, other differences among the quoted PMS low-mass star models are relevant, in particular the adopted equation of state, the radiative opacity, the atmospheric structures used to specify the outer boundary conditions, and the adopted initial abundances of the chemical elements (mainly helium and total metallicity) at a fixed [Fe/H] value (see, e.g., Siess et al. 2001, Mathieu et al. 2007, Tognelli et al. 2011). As a result, the age and mass inferred by comparing evolutionary tracks and data might change significantly for different stellar models (i.e., input physics).

These models are shown in Fig. 5.5, where different isomasses and isochrones are plotted. We have placed AB Dor Ba and Bb in the H-R diagrams in Fig. 5.5 using the spectroscopically determined effective temperatures of Wolter et al. (2014) and the K magnitude measured by Janson et al. (2007). The BCAH98 and TDP12 models suggest that AB Dor Ba and Bb are coeval, with an age between ~50 Myr and 100 Myr, similar to that reported by Janson et al. (2007) and Wolter et al. (2004). S00 provides a slightly older age, but non-coevality. Finally, MD06 predicts substantially older ages, 100−125 Myr for both stars. This last age range seems to agree with the age derived by Barenfeld et al. (2013) for the nucleus of the AB Dor-MG (>110 Myr).

On the other hand, the theoretical masses predicted from the models agree with our dynamical estimates just at the extreme of their uncertainties. The models of BCAH98 and TDP12 (with a denser distribution of isomasses than S00) predict mass ranges of 0.18−0.25 $M_\odot$ for component Ba and 0.14−0.21 $M_\odot$ for component Bb. The MD06 models also underpredict the masses of Ba and Bb but with a better agreement, in practice within the standard deviations of our dynamical measurements. Therefore, for the BCAH98, TDP12, and S00 models the dynamical masses reported in this work are 30% and 40% larger than the central values of the range predicted for AB Dor Ba and Bb, respectively. This disagreement decreases to 10% for the MD06 models. Our results seem consistent with similar comparisons of dynamical and theoretical masses done by other authors (Hillenbrand & White 2004; Stassun et al. 2004; Mathieu et al. 2007) who concluded that models underpredict stellar masses by 10−30% for PMS stars with masses in the range 0.3−1.2 $M_\odot$. Our comparisons suggest that this disagreement holds for masses below 0.3 $M_\odot$. We note that other stellar models designed specifically for lower mass objects (e.g., DUSTY models, Chabrier et al. 2000) do not cover the range 0.2−0.3 $M_\odot$.

5.4.2 Alternative scenario for the binary AB Dor B

As noted in Sect. 5.3.1, both AB Dor Ba and AB Dor Bb are strong, compact radio emitters, which contributes to the emerging perception that many radio stars reside in double or multiple systems (Melis et al 2013; Azulay et al. 2014). Considering the radio/X-ray activity correlation (Güdel et al. 1993), this perception finds support in other, better reported statistics which relates X-ray activity and binarity, namely, that about 79% of the X-ray emitters are in binary systems (Makarov & Eggleton 2009). Many of these binaries correspond to close binaries, but interestingly, a large fraction of the total X-ray binaries (67%; Makarov & Eggleton 2009) are part of hierarchical triple systems, with the third body in a wider orbit. In this scheme, the presence of the wide companion induces dynamical perturbations to the orbit of the close binary at each periastron passage through the Kozai cycles and tidal friction mechanism (e.g., Mazeh & Shaham 1979; Fabrycky & Tremaine 2007). Provided that the inner and outer orbits are misaligned, such an interaction progressively produces a loss of angular momentum that leads the close binary to shrink, to increment its orbital period, and in some cases to begin a merging process. The resulting merger will retain part of the angular momentum showing, as a consequence, an extraordinarily high rotational velocity, which will translate to high levels of activity both at X-ray and radio. This appears precisely to be the scenario found in some of the young radio stars in binary systems. Makarov & Eggleton (2009) explained the origin of the high rotation rate of AB Dor A (0.5 days) via Kozai cycling and tidal interaction between a close binary (now merged in AB Dor A) and the 0.090 $M_\odot$ low-mass companion AB Dor C, orbiting AB Dor A at a mean distance of 2 A.U. with a period of 11.74 yr.

Could a similar mechanism be acting in AB Dor B? The remarkably high radio emission in both AB Dor Ba and AB Dor Bb reported in this work and the rapid rotation suspected to occur in the two stars, <0.88 days (Wolter et al. 2014), provide support for this hypothesis. In addition, the separation Ba−Bb is only 0.15 A.U. at periastron with a much faster period than the pair AB Dor A/C, ~1 yr. Therefore, a more efficient Kozai cycling and tidal interaction might be taking place. Interestingly, this hypothesis would imply a double-double scenario where both components, Ba or Bb, resulting from their respective mergers, would act as mutual "third bodies" with respect to each other. This double-double scenario does not appear to be rare and it has been proposed to explain the light curves of quadruple systems of eclipsing binaries (Cagaš & Pejcha 2012).

5.5 Conclusions

We have shown the first VLBI images of the binary AB Dor B where we detect the presence of compact radio emission in both components. The scientific output of our LBA astrometric monitoring has been optimized, since both the absolute and relative orbits have been determined in combination with published NIR relative positions. The dynamical masses of the individual components of AB Dor B are very similar (0.28 and 0.25 $M_{\odot}$, for Ba and Bb, respectively). Depending on the models, these values are 10−30% (10−40%) larger than the theoretical estimates of PMS evolutionary models for AB Dor Ba (AB Dor Bb), emphasizing the known tendency of these models to underpredict the masses, yet within 2-σ of the predicted values. Comparisons in H-R diagrams favor an age between 50 Myr and 100 Myr, although the Montalbán & D'Antona (2006) models predicts ages older than 100 Myr. AB Dor B is one of the systems in the AB Dor-MG whose two components are radio emitters, contributing to the evidence that many young, wide binaries are strong radio emitters (like AB Dor A and HD 160934; see Azulay et al. 2014). This radio/binarity correlation may be the radio counterpart of the better established relationship between wide binaries and X-ray activity, which can be explained under the assumption that the present wide binaries were originated by dynamical interaction of hierarchical triple systems. This means that AB Dor Ba/Bb could be understood as two earlier close binaries, a double-double system, where both binaries were forced to shrink and merge via mutually induced, cyclic dynamical perturbations. The two evolved mergers (the present stars Ba and Bb) would thus keep part of the angular momentum as a very rapid rotation, responsible in turn for both the X-ray and radio activity.

New and more precise estimates of the dynamical masses would be desirable via an improved coverage of the orbit, where the resolution and sensitivity of the LBA array has been shown to be essential. Likewise, as pointed out by Janson et al. (2007) and Wolter et al. (2014), high-resolution spectroscopy of the components in AB Dor B would also better constrain their placement in H-R diagrams. These observations would also help to confirm the suspected rapid rotation of both components, as well as to determine the tilt of the spin axis of each star with respect to the orbital plane, which could add arguments in favor of the interpretation of the binary AB Dor B as an earlier double close-binary system.

Annex: New model BHAC15

During the first half of 2015, Baraffe et al. (2015) presented new models for low-mass stars that supersede the popularly used BCAH98 models, which incorporate, among other improvements, a new treatment of atmospheric convection (calibrated on 2D/3D radiative hydrodynamic simulations; Freytag et al. 2010; 2012), particularly susceptible at young ages. Accordingly, we have added comparisons with these new models to check the effect of those improvements on the AB Dor Ba/Bb system; the representation is shown in Fig. 5.6 (right side). While the age of the system remains similar in both BCAH98 and BHAC15 models, we can see noticeable differences in relation to the masses, where the new models seem to be $\sim$0.1−0.2 $M_\odot$ closer to the dynamical estimates than the BCHA98 predictions. In any case, the new theoretical isomasses still underestimate our dynamical masses.

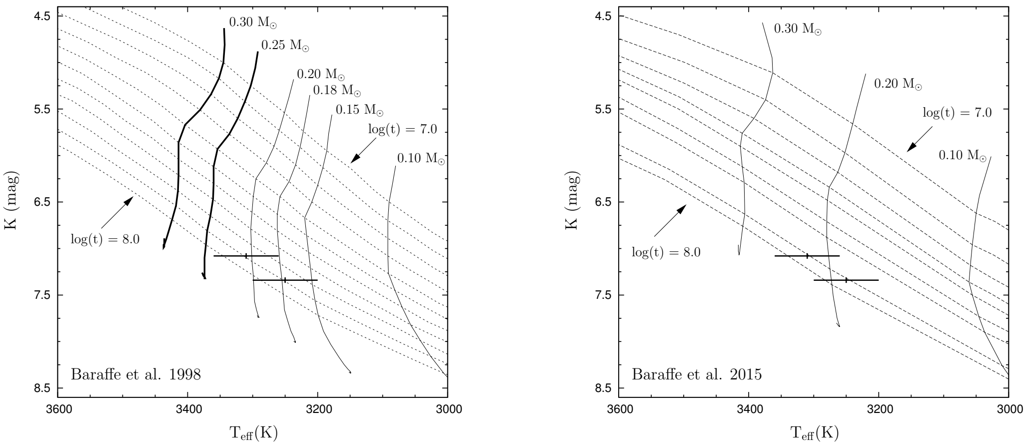

Fig. 5.6 Comparison of AB Dor B components with the new PMS theoretical models of Baraffe et al. 2015. Isomasses (*solid lines*) and isochrones (*dashed lines*) are plotted. The theoretical masses remain consistent with our dynamical estimates just at the extreme of their uncertainties (*right*). For an easy viewing of the improvements regarding the BCAH98 models, the latter are also plotted (*left*).

Annex: The AB Dor A/C system revisited

As we said in Section 3.2.2 (Chapter 3), AB Dor A, the main system of the AB Dor-MG, is a very studied star. Simultaneously with our observations made for AB Dor B with the LBA, AB Dor A was also observed in the three epochs. Although we are not going to deepen in its study, these new observations force us to revise the orbital parameters and masses (masses of AB Dor A and its companion AB Dor C) obtained so far.

The phase-referenced naturally-weighted images of AB Dor A are shown in Fig. 5.7. In the process of obtaining the images we used exactly the same observations of the calibrator PKS 0516−621 that we used for AB Dor B and proceeded in a similar way. In all the three images the star AB Dor A, that is known to be a strong radio emitter, is clearly detected. Circular Gaussian least-squares-fitted parameters are shown in Table 5.5. The companion AB Dor C, direct imaged by Close et al. (2005) with the NACO SDI camera, is not detected in any of the three maps.

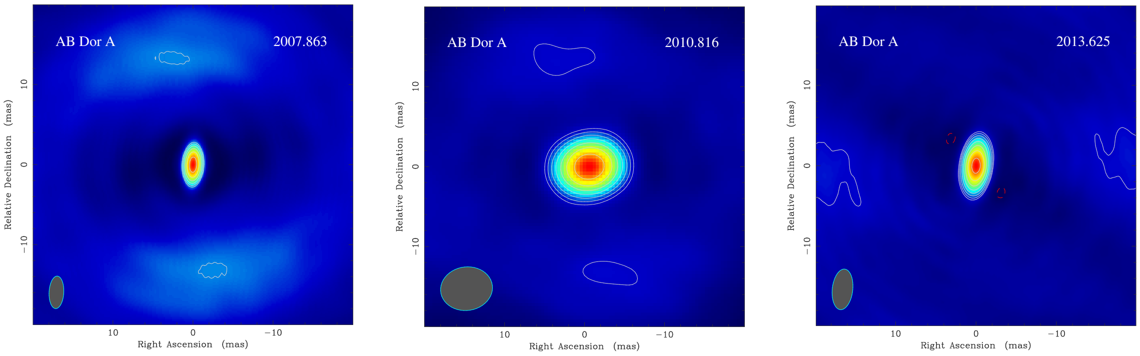

Fig. 5.7 Clean maps of the star AB Dor A at the three LBA epochs. In each map, the lowest contour level corresponds to 3 times the statistical root-mean-square (0.20, 0.05, and 0.18 mJy beam^{-1}) with a scale factor between contiguous contours of $\sqrt{2}$. The peak flux densities in the images are, respectively, 11.1, 5.84, and 10.10 mJy beam^{-1}. For image parameters see Table 5.5. In all the maps we have centered the position of AB Dor A at the origin. Absolute positions are in Table 5.6.

Table 5.5 Circular Gaussian fits corresponding to the VLBI maps of the components of AB Dor B

Epoch	Component	Flux (mJy)	Diameter (mas)
2007.863	A	10.84 ± 0.28	2.97 ± 0.05
2010.816	A	5.43 ± 0.06	4.81 ± 0.04
2013.625	A	9.90 ± 0.25	2.56 ± 0.04

Table 5.6 Compilation of astrometric measurements for the AB Dor A system

		Relative positions AB Dor A − AB Dor C		
Epoch	Instrument	$\Delta\alpha$ (arcsec)	$\Delta\delta$ (arcsec)	Reference
2004.093	VLT/NACO (IR)	−0.125±0.008	0.094±0.006	(1)
2005.017	"	−0.089±0.004	0.200±0.007	(2)
2006.066	"	0.003±0.003	0.202±0.003	(2)
		Absolute positions AB Dor A		
Epoch	Instrument	RA (h m s)	Dec ($^\circ\,'\,''$)	
1990.3888	*Hipparcos*	5 28 44.77474 ± 0.00026	−65 26 56.24163 ± 0.00074	(3)
1990.5640	*Hipparcos*	5 28 44.78652 ± 0.00025	−65 26 56.22719 ± 0.00068	(3)
1991.0490	*Hipparcos*	5 28 44.77578 ± 0.00024	−65 26 56.26151 ± 0.00075	(3)
1991.5330	*Hipparcos*	5 28 44.78942 ± 0.00025	−65 26 56.07567 ± 0.00083	(3)
1992.0180	*Hipparcos*	5 28 44.78202 ± 0.00024	−65 26 56.11601 ± 0.00088	(3)
1992.2329	VLBI	5 28 44.77687 ± 0.00019	−65 26 56.00487 ± 0.00070	(3)
1992.6849	VLBI	5 28 44.80124 ± 0.00018	−65 26 55.93947 ± 0.00063	(3)
1993.1233	VLBI	5 28 44.78492 ± 0.00024	−65 26 55.91371 ± 0.00084	(3)
1994.8137	VLBI	5 28 44.81768 ± 0.00019	−65 26 55.68661 ± 0.00047	(3)
1995.1425	VLBI	5 28 44.80247 ± 0.00027	−65 26 55.62477 ± 0.00114	(3)
1996.1507	VLBI	5 28 44.81137 ± 0.00013	−65 26 55.48519 ± 0.00032	(3)
1996.3607	VLBI	5 28 44.81776 ± 0.00018	−65 26 55.37851 ± 0.00104	(3)
2007.863	VLBI	5 28 44.91481 ± 0.00018	−65 26 53.8633 ± 0.00104	(4)
2010.816	VLBI	5 28 44.94156 ± 0.00018	−65 26 53.4577 ± 0.00104	(4)
2013.625	VLBI	5 28 44.96397 ± 0.00018	−65 26 52.9318 ± 0.00104	(4)

Notes. (1) Close et al. (2005); (2) Close et al. (2007); (3) Guirado et al. (1997); (4) This study. The standard deviation of the relative position corresponds to the uncertainty based on the signal-to-noise ratio of the peaks of brightness of AB Dor Ba and Bb. The absolute positions were obtained with reference to the IERS coordinate of the external quasar PKS 0516−621 ($\alpha = 5^{\mathrm{h}}16^{\mathrm{m}}44^{\mathrm{s}}.926178, \delta = -62^\circ\,7'\,5''.38930$). The standard deviation of the absolute position includes, in addition to the uncertainty of their respective peaks of brightness, the contribution of the propagation media and the reference source structure.

These new observations allowed us to determine new absolute positions of AB Dor A. These positions, together with the previous ones obtained, can be seen in Table 5.6. We did again a least-square fit to determine revisited orbital parameters and the individual masses of both components, A and C, that are 0.894±0.040 and 0.090±0.005, respectively. All these parameters are shown in Table 5.7. Plots of the absolute orbits and a detail of the AB Dor A orbit are shown in Fig. 5.8 and 5.9. The weighted rms of the postfit residuals of AB Dor A (plotted in Fig. 5.10) is 1.1 mas; although some unmodelled effects are present we discard, within our present uncertainties, the presence of further companions to this system.

In order to compare our dynamical masses with the PMS theoretical models we have used the models from BCAH98, TDP12, and BHAC15 for AB Dor A and the models from DUSTY (Chabrier et al. 2000) and BHAC15 for AB Dor C. The choice of different models depending on the star is due to the availability of them according to the masses of the objects. Each star

Table 5.7 Estimates of the astrometric and orbital parameters of AB Dor A[a,b]

Parameter	Value
α_0 (h m s):	5 28 44.79483 ± 0.00016
δ_0 (° ′ ″):	−65 26 55.91774 ± 0.00071
μ_α (s yr^{-1}):	0.00755 ± 0.00001
μ_δ (arcsec yr^{-1}):	0.14101 ± 0.00004
π (arcsec)[c]:	0.06640 ± 0.00030
P (yr):	11.78 ± 0.07
$a_{\rm rel}$ (″):	0.345 ± 0.002
$a_{\rm A}$ (″):	0.0314 ± 0.0007
e:	0.59 ± 0.03
i (°):	66 ± 1
ω_A (°):	116 ± 2
Ω (°):	131 ± 2
T_0:	1991.9 ± 0.1
$m_{\rm A}$ ($M_\odot$):	0.894 ± 0.040
$m_{\rm C}$ ($M_\odot$):	0.090 ± 0.005

Notes. [a] The reference epoch is 2000.0. [b] The minimum value for the reduced χ^2 is 1.3.

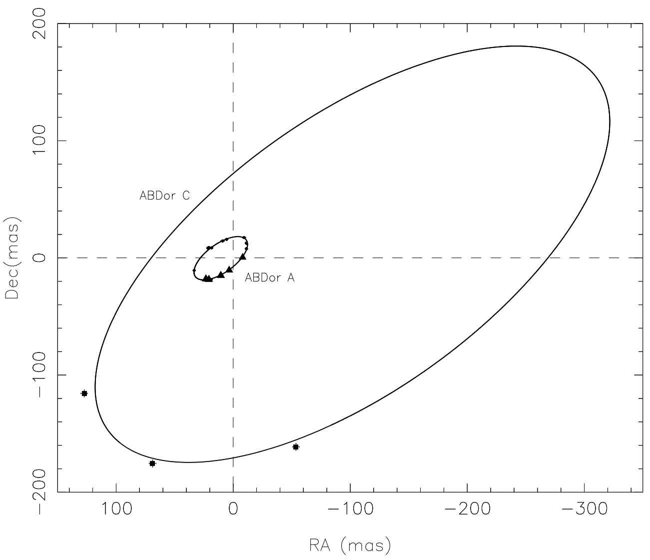

Fig. 5.8 Absolute orbits of the components AB Dor A and AB Dor C using the orbital elements in Table 5.7 (with a_A and a_C, respectively). The positions of the component A (circles and triangles) and C (squares) are marked. The center of mass of the system is placed at the origin.

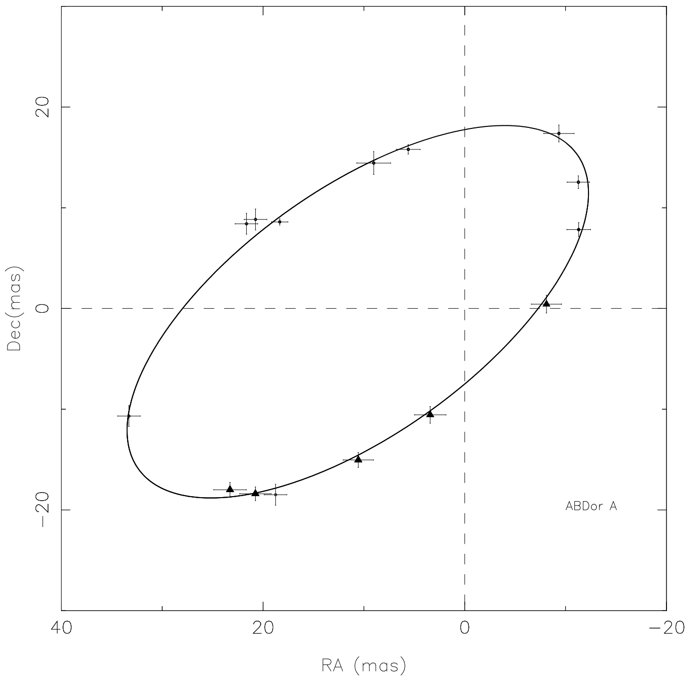

Fig. 5.9 Zoom of Fig 5.8 to show in detail the orbit of the component AB Dor A.

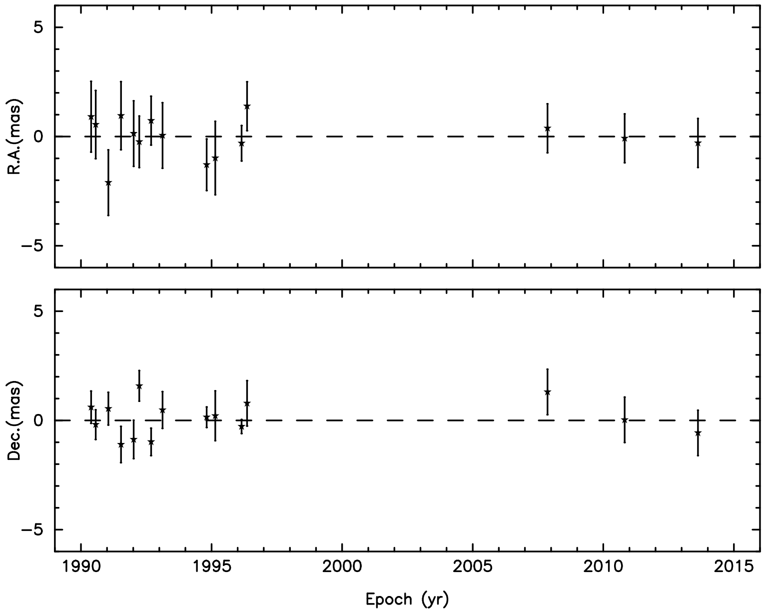

Fig. 5.10 Postfit residuals in right ascension (*upper panel*) and declination (*lower panel*) of the component AB Dor A. The weighted rms is 1.1 mas (see text).

is placed in the H-R diagrams using the absolute K magnitude, the effective temperature, and the luminosity from Close et al. (2007). In Fig. 5.11 we show the H-R diagrams for the three models considered for AB Dor A; in Fig. 5.12, the models considered for AB Dor C.

On the one hand, in the case of AB Dor A, we have discarded to plot the models with $\alpha = 1.00$, following the results reported by Guirado et al. (2011), who showed that they fail to predict any of the measurements. All three models, BCAH98 with $\alpha = 1.90$, BHAC15 with $\alpha = 1.90$, and TDP12 with $\alpha = 1.74$, offer good predictions for the mass within the uncertainties. All models seems to favor an early age for AB Dor A (a range of 35−50 Myr covers the estimates of the three models). On the other hand, in the case of AB Dor C, the models derive a mass of 0.09 $M_{\odot}$, a good estimate of our dynamical mass. Both models suggest an age between 40 and 120 Myr.

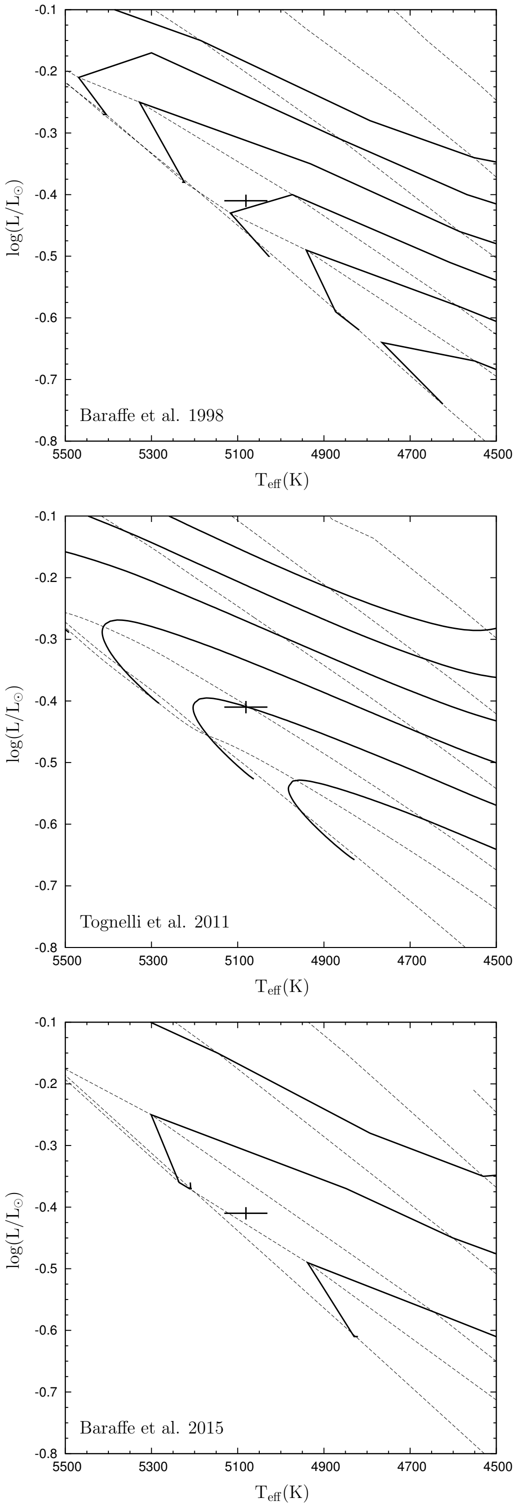

Fig. 5.11 Comparison of AB Dor A with some PMS theoretical models (BCAH98, *top*; TDP12, *middle*; BHAC15, *bottom*). Isochrones (dashed lines) correspond to 10 (top isochrone), 16, 25, 40, 50, and 100 Myr. Isomasses (solid lines) are for 0.75 (bottom isomass), 0.80, 0.85, 0.90, 0.95, and 1.00 $M_\odot$ in the case of BCAH98 and TDP12, and for 0.80 (bottom isomass), 0.90, and 1.00 $M_\odot$ in the case of BHAC15. We have considered the value $\alpha = 1.90$ for BCAH98 and the value $\alpha = 1.74$ for TDP12.

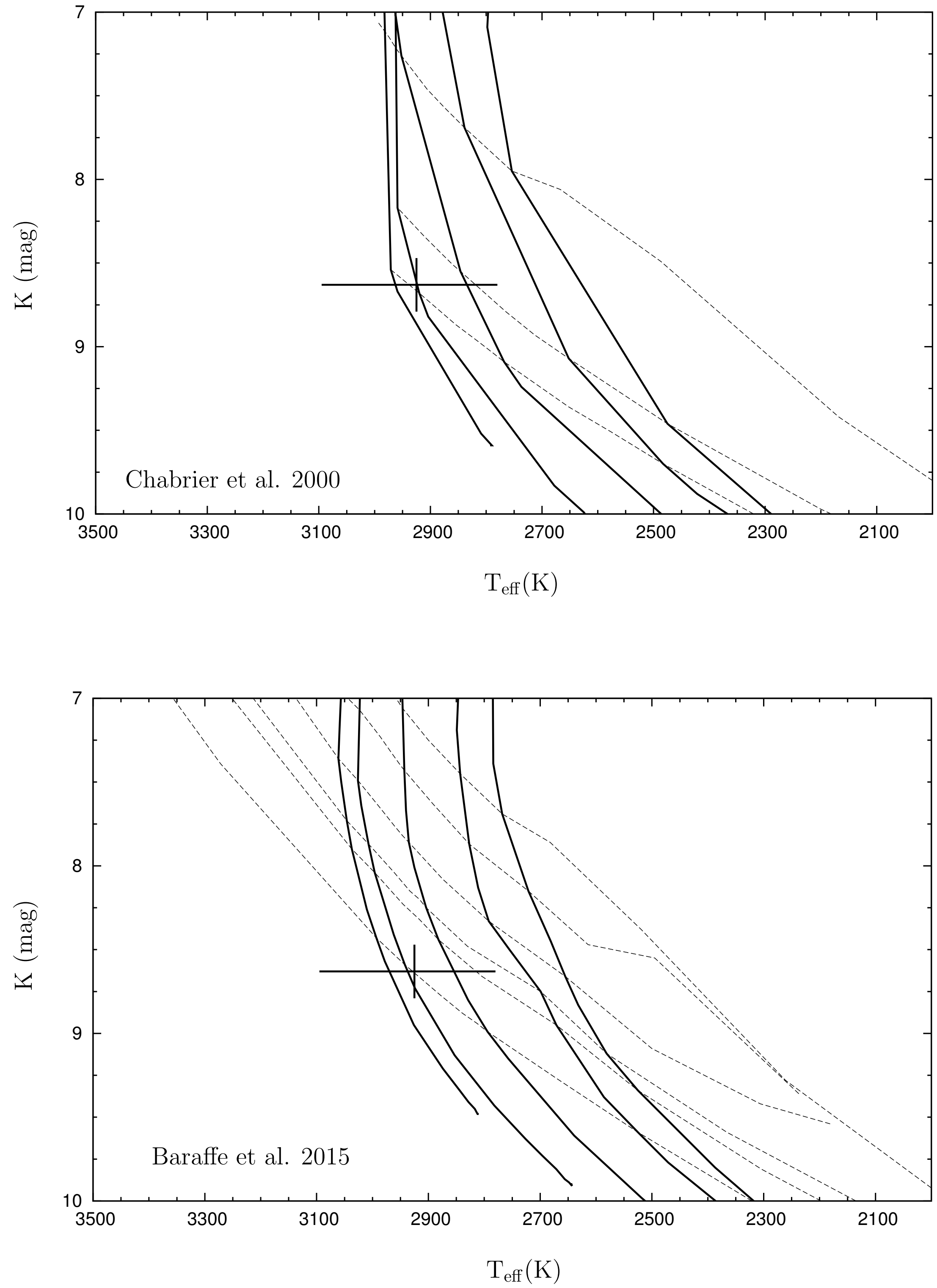

Fig. 5.12 Comparison of AB Dor C with PMS theoretical models of Chabrier et al. (2000) (*top*) and Baraffe et al. (2015) (*bottom*). Isochrones (dashed lines) correspond to 10 (top isochrone), 50, and 100 Myr, in the case of the DUSTY models, and to 10 (top isochrone), 16, 25, 40, 50, and 100 Myr, in the case of BHAC15. Isomasses (solid lines), in both cases, are for 0.04 (rightmost isomass), 0.05, 0.07, 0.09, and 0.10 $M_\odot$.

Chapter 6

Radio detection and dynamical masses of the young binary HD 160934

This chapter is based on the publication appeared in the journal Astronomy and Astrophysics, 561, A38, 2014:

Radio detection of the young binary HD 160934

R. Azulay, J.C. Guirado, J.M. Marcaide, I. Martí-Vidal, B. Arroyo-Torres

Abstract

Context: Precise measures of dynamical masses of pre-main-sequence (PMS) stars are essential to calibrate stellar evolution models that are widely used to derive theoretical masses of young low-mass objects. Binary stars in young, nearby loose associations are particularly good candidates for this calibration since all members share a common age. Interestingly, some of these young binaries present a persistent and compact radio emission, which makes them excellent targets for astrometric VLBI studies.
Aims: We aim to monitor the orbital motion of the binary system HD 160934, a member of the AB Doradus moving group.
Methods: We observed HD 160934 with the Very Large Array and the European VLBI Network at 8.4 and 5 GHz, respectively. The orbital information derived from these observations was analyzed along with previously reported orbital measurements.
Results: We show that the two components of the binary, HD 160934 A and HD 160934 c, display compact radio emission at VLBI scales, providing precise information on the relative orbit. Revised orbital elements were estimated.
Conclusions: From our VLBI monitoring of this pair we have determined precise model-independent mass estimates for the A and c components, which serve as calibration tests for PMS evolutionary models.

6.1 Introduction

Studies of the fundamental parameters of pre-main-sequence (PMS) stars are relevant since they provide tests of stellar evolution models (e.g. Baraffe et al. 1998; Chabrier et al. 2000). These models are widely used to derive theoretical masses of photometrically detected young low-mass objects. Given the importance of these models we need to find objects whose mass and luminosity are independently measured, so they can act as calibrators. Certainly, there is a small number of systems with masses $< 1.2\,\mathrm{M}_\odot$ (Hillenbrand & White 2004) with precise mass determination.

There are several methods to calculate dynamical masses: spectroscopy of double-line binaries (e.g., Steffen et al. 2001), rotation of circumstellar disks (e.g., Simon et al. 2000; Dutrey et al. 2003), or monitoring of the orbital motion at different wavelenghts, for instance, in the infrared (Ghez et al. 1993) or radio (Guirado et al. 1997). Necessarily, all of these methods are applicable to a limited number of stars only. Particularly, we used tecniques based on the star compact radio emission to monitor the orbital motion of the binary with high precision. This method has previously been applied to revelant cases such as the AB Doradus quadruple system (Guirado et al. 2006) or V773 Tau (Boden et al. 2007; Torres et al. 2012); similar studies have been reported for T Tau Sb (Loinard et al. 2007), YLW15 (Girart et al. 2004), and L1551 IRS 5 (Rodríguez et al. 2003).

Binary stars in young nearby moving groups (loose associations of coeval, co-moving stars; Zuckerman & Song 2004; Torres et al. 2008) offer an opportunity to increase the number of PMS stars with dynamically determined masses. We selected the AB Doradus moving group (AB Dor-MG) as the best-suited association to apply radio-based high-precision astrometric techniques to study binary systems. This choice is well supported by the system's mean distance to the Sun (30 pc), its reasonably well known age (50-70 Myr; Janson et al. 2006; Guirado et al. 2011), and the presence of radio emission in some of its active members, among others LO Peg, PW And, and AB Dor (Guirado et al. 2006; Azulay et al. 2015). Following the list of AB Dor-MG members in Torres et al. (2008), we initiated a VLA/VLBI program to monitor binary systems known to host low-mass companions, and which are likely to present radio emission.

One of the stars included in our program is HD 160934 (= HIP 86346), a very active young star with spectral type K7Ve (Schlieder et al. 2012), placed at a distance of ~33 pc (van Leeuwen 2007), which belongs to the AB Dor-MG (López-Santiago et al. 2006). The activity of this star is shown by strong X-ray emission ($L_X = 0.25 \times 10^{30}$ erg s^{-1}), star spots, a high rotation rate ($v \sin i = 16.4$ km s^{-1}; Fekel 1997), and chromospheric activity (Pandey et al. 2002). Despite this intense activity, no radio emission has been reported so far. The existence of a close companion (HD 160934 c) around the main star (HD 160934 A) was first reported by Gálvez et al. (2006) from radial velocity measurements; in addition, relative astrometry was provided by Hormuth et al. (2007) and Lafrenière et al. (2007). A combined analysis of all previous data, including new precise relative astrometry from aperture-masking interferometry, has been undertaken by Evans et al. (2012) to derive a period of ~3764 days, semimajor axis of ~152.5 mas (5.05 AU), and a total mass for both stars of $1.21\pm0.27\,M_\odot$. HD 160934 is a tertiary system: Lowrance et al. (2005) detected a third low-mass ($0.15\,M_\odot$) component (HD 160934 B) at a distance of ~8.″7 from the primary pair.

In this chapter we report infrared (AstraLux) and radio observations (VLA/VLBI) of HD 160934 which have resulted in a revised photometry and the discovery of compact radio emission from components A and c, respectively. These detections provide new, precise points on their relative and absolute orbits, which necessarily leads us to a revision of the orbital elements and mass estimates.

6.2 Observations and data reduction

6.2.1 AstraLux observations

We observed the system HD 160934 with the Lucky Imaging AstraLux camera (Hormuth et al. 2008) at the Calar Alto 2.2 m telescope. The Lucky Imaging technique permits to reduce the distortions due to atmosphere by acquiring a large number of short-exposure images and combining the best few percent of high-quality images to obtain a final image relatively unaffected by atmospheric turbulence (Hormuth et al. 2007 and reference therein). The observations were carried out on June 24, 2013 and November 19, 2015 using two different filters, SDSS_i and SDSS_z. We took 10000 individual frames with exposure times of 30 ms each. The individual frames were dark and flat corrected before selecting the best 10% of the accquisitions. The final image was constructed by shifting and adding the selected frames. We also observed the stars at the center of the globular cluster M15, whose positions were used for astrometric calibration in the way described in Hormuth et al. (2007). The field of view was 24″×24″ in a 512×512 pixel frame.

The resulting images of HD 160934 are shown in Fig. 6.1. We notice that both components are not distinguished in the 2013 images, but clearly they are in those of 2015, where c is near the apoastron. We fit a binary model to find the separation and flux ratio of the latter images; the results are shown in Table 6.1, along with previous estimates.

To proceed with the calibration of PMS models, in a similar way that we did in the previous chapter for AB Dor B, we need the K magnitude and effective temperature of components A and c. Estimates of the individual K magnitudes can be obtained from the

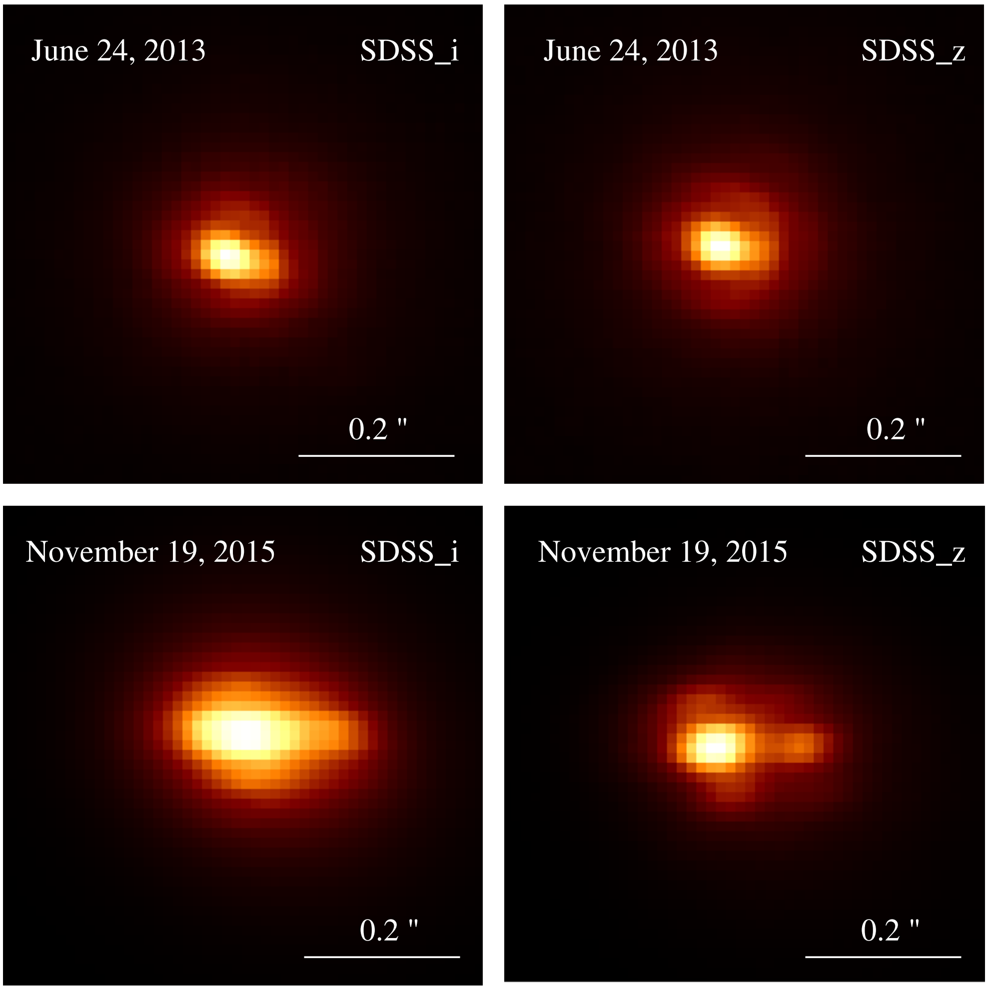

Fig. 6.1 AstraLux SDSS_i and SDSS_z images of the binary star HD 160934 in 2013 and 2015; North is up and East is to the left. Both components of the star are not distinguished in the 2013 images but are clearly detectable in the 2015 images.

Table 6.1 Binary properties of HD 160934

Date (Filter)	Separation [″]	PA [°]	Flux ratio	Reference
June 30, 1998 (F165M)	0.155 ± 0.001	275.5 ± 0.2	0.485 ± 0.006	Hormuth et al. (2007)
April 17, 2005 (NIRI−CH4)	0.218 ± 0.002	268.5 ± 0.7	0.455 ± 0.021	Lafrenière et al. (2007)
July 8, 2006 (RG830)	0.215 ± 0.002	270.9 ± 0.3	0.329 ± 0.051	Hormuth et al. (2007)
November 19, 2015 (SDSS_z)	0.226 ± 0.010	267 ± 1	0.51 ± 0.10	This work
November 19, 2015 (SDSS_i)	0.209 ± 0.025	270 ± 5	0.58 ± 0.20	This work

Notes. The central wavelength of the filters are (in μm): 1.6511 (F165M), 1.58 (NIRI-CH4), 0.910 (RG830), 0.907 (SDSS_z), and 0.767 (SDSS_i).

Table 6.2 Unresolved 2MASS photometry of HD160934

Filter/Color	Magnitude
J	7.618 ± 0.024
H	6.998 ± 0.016
K	6.812 ± 0.020

unresolved JHK 2MASS photometry (see Table 6.2) combined with the flux ratio between c and A ($f_{\mathrm{c/A}}$) at K band; however, although $f_{\mathrm{c/A}}$ has been measured for different filters (see Table 6.1), there is not available a value for K-band. To solve this, we calculated $f_{\mathrm{c/A}}$ at K-band by extrapolation of the values given in Table 6.1. To cover this rough approximation we assigned a conservative standard deviation to this flux ratio ($f_{\mathrm{c/A}} = 0.39 \pm 0.11$). Final values for the absolute K-magnitudes were 4.65±0.15 and 5.68±0.15 for components A and c, respectively. Regarding the effective temperatures, we derived a value for component A from its spectral type (K7−K8, McCarthy & White 2012) using the empirical color-temperature transformation reported by Hartigan et al. (1994). For component c, we proceed in a similar way by assuming a M2−3 spectral type (Gálvez et al. 2006), estimated from the unresolved H−K color and flux ratios in Table 6.2. Final values for the effective temperature were 3940±60 K and 3425±80 K for component A and c, respectively.

6.2.2 VLA observations

We observed the star HD 160934 with the VLA at 8.4 GHz in B configuration on 2009 February 13. The effective bandwidth was 4 × 43 MHz in RCP, which was enough to achieve an rms sensitivity of 0.020 mJy. The source 0137+331 was used as primary flux calibrator, and the quasar J1746+6226 (1.5°distant from the target) was selected as phase calibrator. The observations lasted 1.5 hours in total, with 1 hour integration time on HD 160934. We reduced the data using standard routines of the program Astronomical Image Processing System (AIPS) of the National Radio Astronomy Observatory. The resulting image of HD 160934 is shown in Fig. 6.2. To our knowledge, this is the first image of HD 160934 at radio wavelengths, revealing a relatively strong, unresolved radio emitter with an integrated flux of 1.92 mJy.

The position of the radio source seen in the VLA image ($17^{\rm h}\,38^{\rm m}\,39.^{\rm s}628$ in R.A. and $+61^\circ 14'\,16.''360$ in Dec) coincides with the J2000 expected optical position of HD 160934 derived from the *Hipparcos* position and proper motion ($17^{\rm h}\,38^{\rm m}\,39.^{\rm s}605$ in R.A. and $+61^\circ 14'\,16.''46$ in declination, accurate to $0.''5$) for that epoch. The deviation between our radio coordinates and the optical expected ones is $0.''20$, which is within the *Hipparcos* uncertainties, and below the resolution provided by the synthesized beam of our observations ($\sim 1''$). Given the small separation of components A and c at the VLA observing epoch (one sixth of the synthesized beam, 140 mas, as estimated from the binary orbit, see Sect. 6.3.2), the two components appear to be blended in Fig. 6.2. On the other hand, we found no evidence of radio emission of the third, low-mass companion HD 160934 B, reported to be at $\sim 8.''7$ from the primary (Lowrance et al 2005).

6.2.3 VLBI observations

The VLA detection described above triggered VLBI observations of HD 160934 that were carried out between 2012 and 2014, using the European VLBI Network, the EVN (see Table 6.2). The frequency of the observations was 5 GHz and both polarizations were recorded with a rate of 1024 Mbps (two polarizations, eight subbands per polarization, 16 MHz per subband, 2 bits per sample). The data were correlated with the EVN MkIV data processor at the Joint Institute for VLBI in Europe (JIVE). These observations lasted 10 hours and were scheduled in phase-reference style, interleaving scans of the ICRF quasar J1746+6226 and the target star HD 160934. The cycle target-calibrator-target lasted about six minutes.

We used AIPS to (i) calibrate the visibility amplitudes, (ii) correct for the ionospheric contribution (task *TECOR* with GPS-driven Global Ionospheric Maps[1]), (iii) self-calibrate

---

[1] http://cddis.nasa.gov/cddis.html

Table 6.3 Journal of observations of HD 160934

Date (Epoch)	Array	UT Range	Beam size [arcsec]	P.A. [°]
13 Feb 2009	VLA (B configuration)	17:15 - 22:15	1.01×0.79	−35.9
30 Oct 2012	EVN[a]	10:30 - 20:30	2.29×1.59	−28.4
23 May 2013	"	21:00 - 07:00	2.20×1.76	−31.3
5 Mar 2014	"	02:00 - 12:00	2.05×1.59	−27.3

Notes. [a]: EVN array: Ef, Wb, Jb, On, Mc, Nt, Tr, Ys, Sv, Zc, Bd, Ur, Sh; where Ef: Effelsberg, Wb: Westerbork, Jb: Jodrell Bank, On: Onsala, Mc: Medicina, Nt: Noto, Tr: Torun, Ys: Yebes, Sv: Svetloe, Zc: Zelenchukskaya, Bd: Badary, Ur: Urumqi, Sh: Shanghai, Hh: Hartebeesthoek.

Table 6.4 Circular Gaussian fits corresponding to the VLBI maps of the components of HD 160934

Epoch	Component	Flux (mJy)	Diameter (mas)
2012.830	A	0.16±0.01	2.76±0.17
	c	0.06±0.01	1.20±0.20
2013.392	A	0.05±0.01	2.52±0.46
2014.175	A	0.13±0.01	2.76±0.20
	c	0.06±0.01	1.83±0.30

the phase of J1746+6226, and (iv) to apply these self-calibration solutions to the target source HD 160934. Both sources were finally deconvolved and imaged using the Caltech imaging program *DIFMAP* (Shepherd et al. 1994). Fig. 6.3 shows the maps of the phase calibrator J1746+6226, performed with uniform weighting to obtain maximum resolution, in which the source presents a jet oriented towards the southwest. The phase-referenced naturally-weighted images of HD 160934 are shown in Fig. 6.4; two point-like features are clearly seen in the VLBI images corresponding to 2012.830 and 2014.175 that can readily be associated to components A and c of the binary HD 160934. In contrast, only a single component (assigned to A) is detected in 2013.392. Circular Gaussian least-squares-fitted parameters for the two components are listed in Table 6.4.

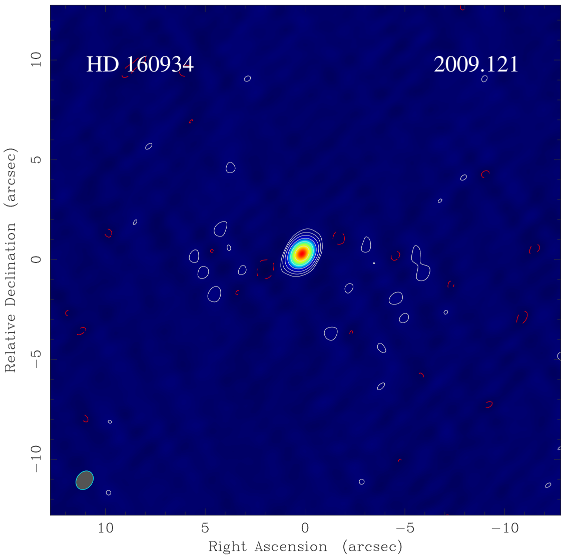

Fig. 6.2 8.4 GHz map of HD 160934 from VLA data taken on 2009.121. The lowest contour level corresponds to 1.5 times the statistical root-mean-square noise (0.01 mJy beam^{-1}) with a scale factor between contiguous contours of $\sqrt{2}$. The peak flux densities in the image is 1.92 mJy/beam. The restoring beam (shown in the bottom-left corner of the map) is an elliptical Gaussian of 1.01 × 0.79 arcsec (PA −35.9°).

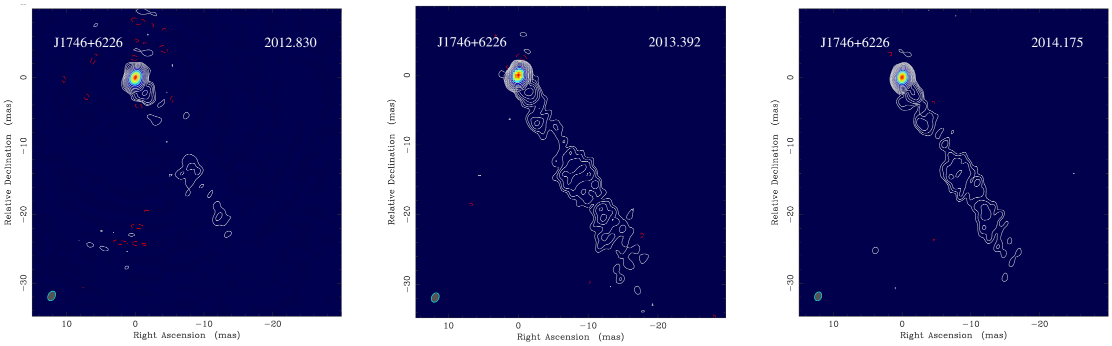

Fig. 6.3 Maps of the calibrator J1746+6226 in the three epochs. In each map, the lowest contour level corresponds to 4 times the statistical root-mean-square noise (0.5, 0.2, and 0.2 mJy beam^{-1}) with a scale factor between contiguous contours of $\sqrt{3}$. The peak flux densities in the images are, respectively, 0.32, 0.32, and 0.34 mJy beam^{-1}.

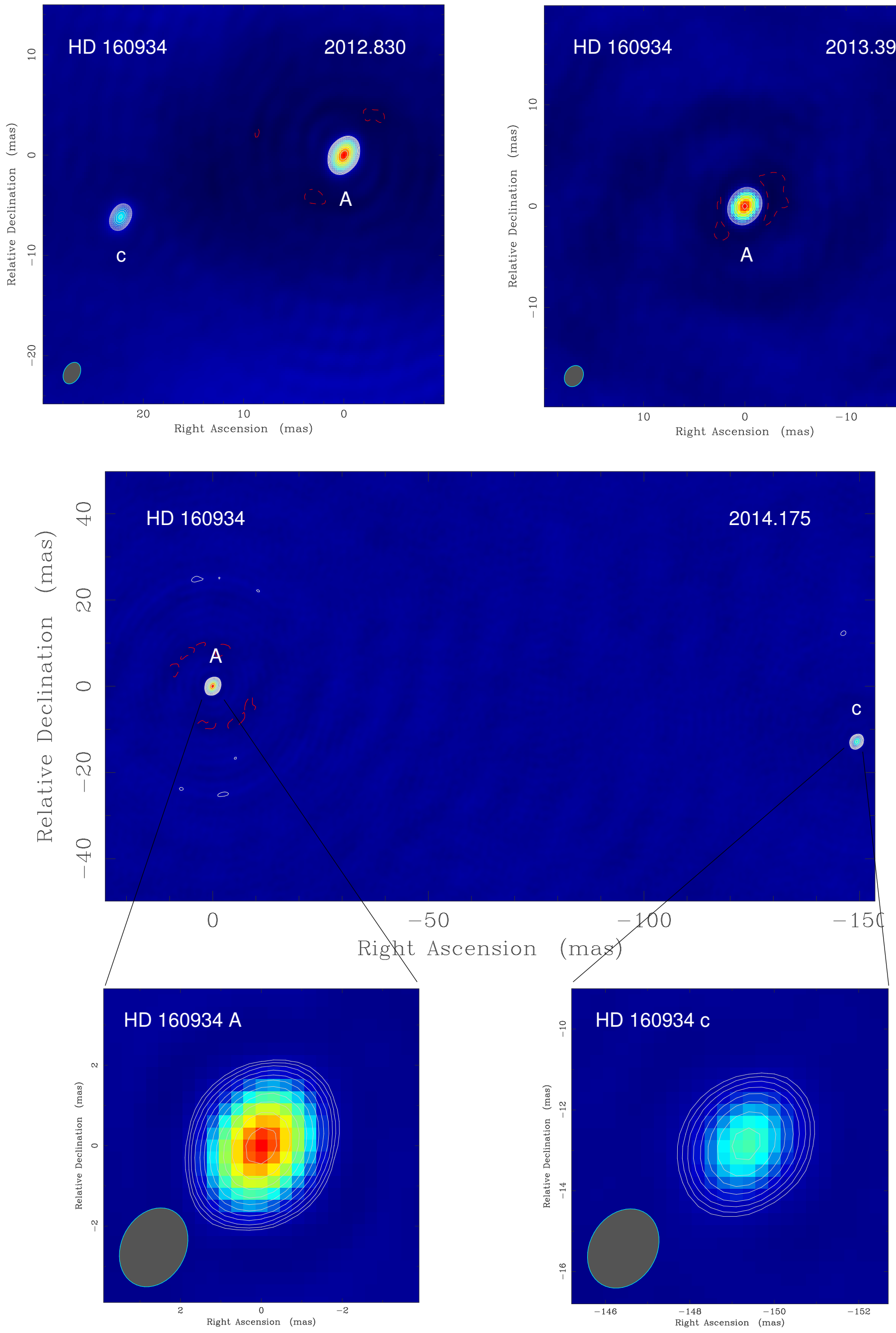

Fig. 6.4 Clean maps of the binary HD 160934 at the three EVN epochs. The lowest contour levels corresponds to 3 times the statistical root-mean-square noise (0.04, 0.02, and 0.04 mJy beam^{-1}) with a scale factor between contiguous contours of $\sqrt{2}$. The peak flux densities in the images are, respectively, 0.15, 0.04, 0.12 mJy beam^{-1}. For image parameters see Table 7.1. In all the maps we have centered at the origin the position of peak of brightness of HD 160934 A. Component c is not detected at epoch 2013.392. Orbital motion of c around A is evident from epochs 2012.830 and 2014.175.

6.3 Results

6.3.1 Radio emission of HD 160934

Our images reveal that HD 160934 is a strong radio emitter. In Chapter 7, its radio luminosity (0.27×10^{15} ergs $\mathrm{Hz}^{-1}\,\mathrm{s}^{-1}$) is compared with other radio star members of the AB Dor-MG, which suggest that gyrosynchrotron emission is acting in this star. We notice that the large discrepancy between the VLA and VLBI flux densities (see Figs. 6.2 and 6.4) could be explained by the presence of low-brightness emission from HD 160934, possibly combined with the expected flux variability of the star, which is resolved out by the EVN baselines.

The detection of the lower-brightness component in our VLBI map (Fig. 6.4) is fortuitous; our original plan was to monitor only the reflex motion of HD 160934 A. This shows that radio activity is not a rare phenomenon in stars belonging to the AB Dor-MG, and, indeed, this is not the first radio binary (i.e., both members of the binary are radio emitters) in this association (i.e., AB Dor Ba/Bb with masses down to 0.25 $M_\odot$, Azulay et al. 2015; Chapter 5). Since all radio stars detected in the AB Dor-MG are fast rotators in the X-ray saturated regime, we could predict a similar scenario for HD 160934 c. We notice that the rotation period could be even longer than the 1.8 days for component A since, as reported by Pizzolato et al. (2003), the smaller the mass of the star, the shorter the rotation period needed to reach the saturation levels.

6.3.2 Orbital parameters

The detection of HD 160934 c in our VLBI images has an obvious astrometric interest, since it provides precise data points of both the relative and the absolute orbits of the binary. The relative position of the pair A−c was measured directly on the maps shown in Fig. 6.4 (except for epoch 2013.39), as well as the absolute position of the main component A, in turn referenced to the position of the external quasar (Table 6.5). We have augmented our data set with previous orbital measurements reported by Evans et al. (2012), who compiled data from aperture masking and earlier infrared relative positions from Hormuth et al. (2007) and Lafrenière et al. (2007). Table 6.5 shows all the archive positions available for the system HD 160934.

As made in Chapter 5 for AB Dor B, we estimated the Keplerian parameters of this binary via a weighted least-squares fit that combined the absolute positions of component A and all the relative positions constructed as A−c, that is, taking c as reference. We followed a similar approach to that used in Chapter 5 for AB Dor B, that is, solving simultaneously for the absolute and relative orbits using the Thiele-Innes elements and the Levenberg-Marquardt

Table 6.5 Compilation of astrometric measurements for the HD 160934 system

Relative positions HD 160934 A – HD 160934 c				
Epoch	Instrument	$\Delta\alpha$ (mas)	$\Delta\delta$ (mas)	Reference
1998.496	AstraLux (IR)	154.3 ± 0.9	−14.8 ± 0.5	(1)
2005.296	Gemini (IR)	212.9 ± 2.0	5.6 ± 2.6	(2)
2006.518	AstraLux (IR)	214.9 ± 1.0	−3.4 ± 1.0	(1)
2006.712	Gemini (IR)	217.9 ± 2.0	−4.9 ± 2.6	(2)
2008.477	Palomar (IR)	−169.1 ± 0.3	−9.7 ± 0.3	(3)
2010.318	Keck (IR)	64.6 ± 0.3	−18.9 ± 0.3	(3)
2011.310	Keck (IR)	−6.3 ± 0.3	−18.9 ± 0.3	(3)
2012.830	EVN (radio)	−22.3±0.1	6.2±0.2	(4)
2014.175	"	149.3±0.1	12.9±0.2	(4)
Absolute positions HD 160934 (EVN)				
Epoch	Component	RA (h m s)	Dec (° ′ ″)	
2012.830	A	17 38 39.59830 ± 0.00014	61 14 16.6077 ± 0.0005	(4)
	c	17 38 39.60138 ± 0.00014	61 14 16.6015 ± 0.0005	(4)
2013.392	A	17 38 39.60667 ± 0.00016	61 14 16.6865 ± 0.0007	(4)
2014.175	A	17 38 39.61159 ± 0.00013	61 14 16.6882 ± 0.0005	(4)
	c	17 38 39.59090 ± 0.00013	61 14 16.6753 ± 0.0005	(4)

Notes. (1) Hormuth et al. (2007); (2) Lafrenière et al. (2007); (3) Evans et al. (2012); (4) This work. The standard deviation of the relative position corresponds to the SNR-based uncertainty of the peaks of brightness of HD 160934 A and c. The absolute position were obtained with reference to the IERS coordinate of the external quasar J1746+6226 ($\alpha = 17^{\mathrm{h}}46^{\mathrm{m}}14^{\mathrm{s}}.034, \delta = 62^{\circ}\,26'\,54''.738$). The standard deviation of the absolute position includes, in addition to their uncertainty of their respective peak of brightness, the contribution of the propagation media and the reference source structure.

algorithm. In practice, we proceed in two steps:

1. We obtained *a priori* values of the orbital elements from a previous least-squares fit to the, more numerous, differential data; in particular we estimated values for the period P (10.33 yr), semimajor axis of the relative orbit $a_{\rm rel}$ ($0.''152$), the eccentricity e (0.63), the three orientation angles i ($82.^\circ4$), ω ($85.^\circ9$), Ω (35°), and the time of periastron T_0 (2002.32).

2. We used the values above as (otherwise excellent) *a priori* to favor the convergence of the L-M algorithm in the combined fit of the absolute (A component) and relative positions (A−c). In this analysis, the proper motion and parallax of the system were also estimated. The resulting set of astrometric and orbital parameters is shown in Table 6.6, meanwhile plots of the relative and absolute orbits can be seen in Fig. 6.5 and 6.6.

We notice that the secular accelerations Q_α and Q_δ (used in the analysis of AB Dor B) were not included in the fit: although there is also a third object in this system, HD 160934 B (located at $8''$ separation from A and c), it does not include an appreciable acceleration in our three-year time baseline of VLBI monitoring (the estimated period of the corresponding reflex orbital motion is of the order of 10^3 years in the most favorable case).

Our fit yields a new value of the parallax (31.4±0.5 mas), which is within the uncertainties, but more precise than the previous *Hipparcos* estimate (30.2±2 mas; van Leeuwen 2007). This new parallax allows us to determine the sum of the masses of both components of HD 160934 using Kepler's third law

$$\frac{(a''_{rel}/\pi'')^3}{P^2} = (m_{\rm A} + m_{\rm c})_\odot. \tag{6.1}$$

We obtain a value of $m_{\rm A} + m_{\rm c}$ of 1.15±0.10 $M_\odot$, coincident with previous estimates made by other authors (Evans et al. 2012 and references therein). Similarly, using the semimajor axis of the absolute orbit of component A, $a_{\rm A}$, we can estimate the mass of component c, $m_{\rm c}$, using $m_{\rm c}^3/(m_{\rm A} + m_{\rm c})^2) = a_A^3/P^2$, which yields a value of 0.45±0.04 $M_\odot$. A value of the $m_{\rm A}$ (= 0.70±0.07 $M_\odot$) follows from a simple substraction of the values above. In principle, the latter value for $m_{\rm A}$ may seem highly correlated with c; however, a similar, but coarser, estimate of $a_{\rm c}$ can be obtained by repeating the combined fit using the absolute positions of component c (see Table 6.5), from which another value of $m_{\rm A}$ can be calculated. The coincidence of both estimates of $m_{\rm A}$ indicates the robustness of our mass determinations.

Table 6.6 Estimates of the astrometric and orbital parameters of HD 160934[a,b]

Parameter	Value
α_0 (h m s):	17 38 39.6349 ± 0.0002
δ_0 (° ′ ″):	+61 14 16.0238 ± 0.0015
μ_α (s yr^{-1}):	−0.0025 ± 0.0002
μ_δ (arcsec yr^{-1}):	0.0469 ± 0.0002
π (arcsec)[c]:	0.0314 ± 0.0005
P (yr):	10.26 ± 0.08
$a_{\rm rel}$ (″):	0.1554 ± 0.0008
$a_{\rm A}$ (″):	0.0603 ± 0.0014
$a_{\rm c}$ (″):	0.0952 ± 0.0014
e:	0.64 ± 0.03
i (°):	82.72 ± 0.12
$\omega_{\rm c}$ (°)[d]:	37.7 ± 0.5
Ω (°):	266.74 ± 0.12
T_0:	2002.4 ± 0.1
$m_{\rm A}$ (M$_\odot$):	0.70 ± 0.07
$m_{\rm c}$ (M$_\odot$):	0.45 ± 0.04

Notes. [a] The reference epoch is 2000.0. [b] The number of degrees of freedom of the fit is 14; the minimum value found for the reduced χ^2 is 1.2. [c] We note that our parallax estimate is more accurate than the *Hipparcos* value given for AB Dor A and still compatible. [d] For the absolute orbit of HD 160934 A $\omega_{\rm A} = \omega_{\rm c} + \pi$.

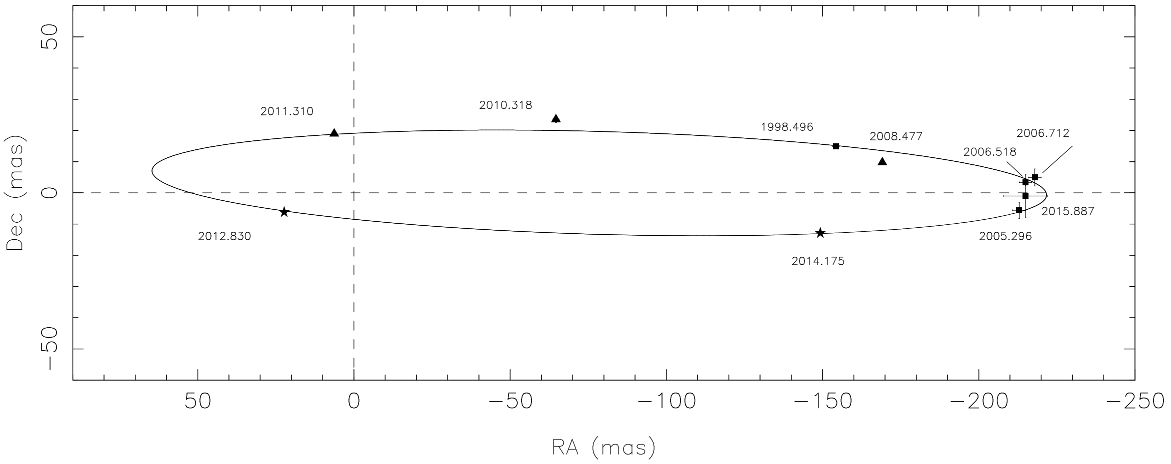

Fig. 6.5 Relative orbit of the binary star HD 160934 c using the orbital elements in Table 6.6 (with $a_{\rm rel}$). HD 160934 A component is located at the origin. Each type of symbol corresponds to a different technique to measure the relative position of HD 160934 c, namely, infrared relative astrometry (squares; Hormuth et al. 2007; Lafrenière et al. 2007), masking interferometry (triangles; Evans et al. 2012), and VLBI (star symbol; this work). Error bars are plotted but hardly visible because of the size of the orbit. For clarity, they are displayed in Fig. 6.7.

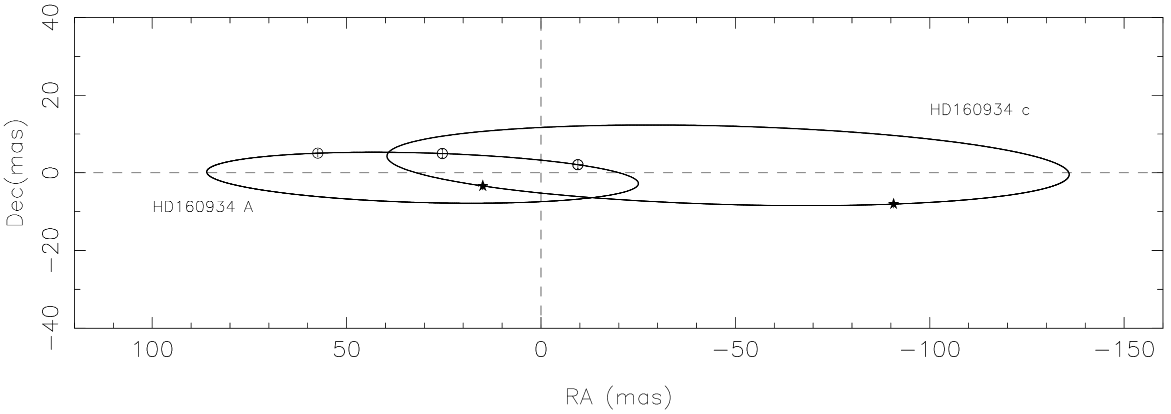

Fig. 6.6 Absolute orbits of the components HD 160934 A and HD 160934 c using the orbital elements in Table 6.6 (with a_A and a_c, respectively). The positions of the component A (circles) and c (star symbols) are marked. The center of mass of the system is placed at the origin.

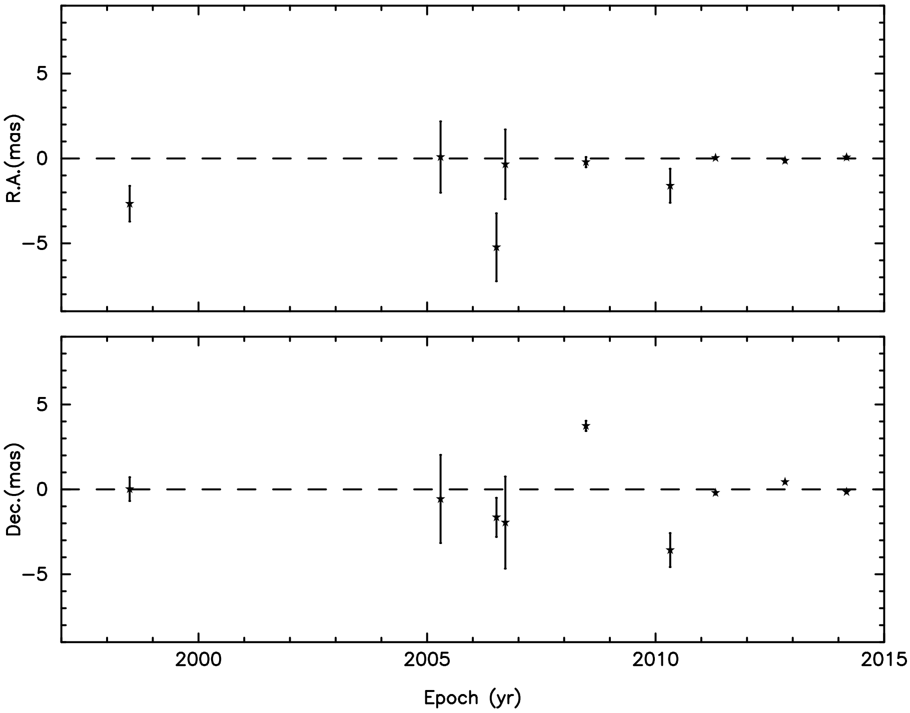

Fig. 6.7 Postfit residuals in right ascension (*upper panel*) and declination (*lower panel*). The weighted rms of the plotted residuals is 3.2 mas.

The weighted rms of the postfit residuals (plotted in Fig. 6.7) is 3.2 mas, meaning that some unmodeled effects are still present in the data. The residuals show no evidence of another companion within the errors. Instead, the possible departure of some of the points from the fitted orbit might indicate instrumental effects that have not been considered. Accordingly, we have scaled the statistical errors of the orbital parameters to take this contribution into account (see Table 6.6).

6.4 Comparison with models

In order to calibrate the stellar evolution models for PMS stars we have considered, in this case, isochrones and isomasses corresponding to the models of BCAH98, S00, TDP12, and BHAC15. In the same way we did with AB Dor B, we adopted a metallicity value of [Fe/H]= 0.0 and a mixing length parameter $\alpha_{\rm ML} = 1.0$, except for the S00 models, where the only value available for the mixing length is 1.61. The different models can be shown in Fig. 6.8. HD 160934 A and HD 160934 c are placed in the H-R diagrams in Fig. 6.8 using the values explained in Section 6.2.1.

The theoretical masses predicted from the models agree with our dynamical estimates, again, just at the extreme of their uncertainties. All four models predict masses for the component A ~10% lower than our dynamical values, while predictions for the component c vary according to the model: BCAH98 and BHAC15 predict masses ~20% lower, S00, ~40% lower, and TDP12, ~30% lower. These results are consistent with previously published works, which conclude that PMS stellar evolution models for low-mass stars underestimate the dynamical values between 10−30%. According to the values above, predictions are better for component A than for component c, that is, the larger the dynamical mass, the smaller the difference between the theoretical and the dynamical estimates. In terms of age, TDP12 and BAHC15 models suggest that both stars are younger than 50 Myr, BCAH98 models favor slightly older ages but younger than 65 Myr, meanwhile S00 models predict younger ages, below 40 Myr.

6.5 Conclusions

In this chapter we have shown the results of a VLBI program dedicated to monitor the absolute reflex motion of HD 160934, a member of the AB Dor-MG. The unexpected detection of compact radio emission of the low mass companion c allowed us to sample not only the absolute orbit of component A (with respect to the external quasar J1746+6226) but also the relative orbit, both of which are necessary to determine model-independent dynamical

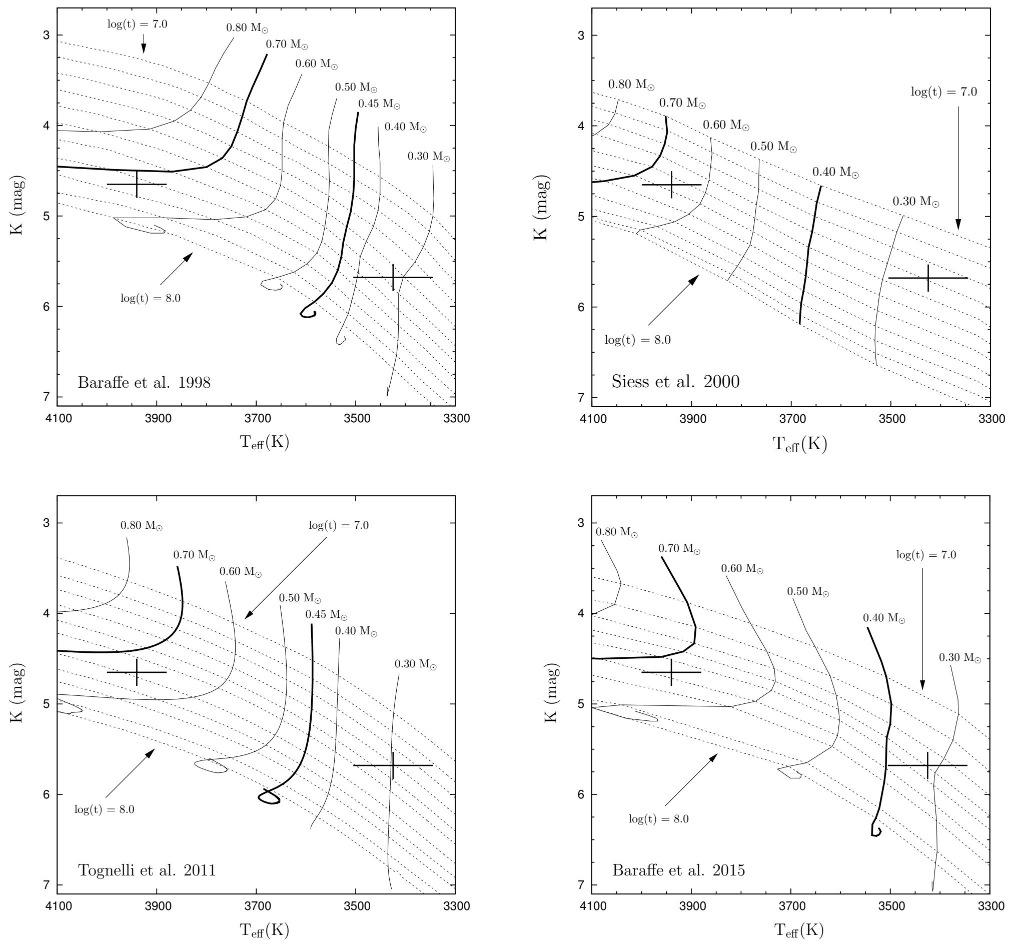

Fig. 6.8 Comparison of HD 160934 components with some PMS theoretical models (Baraffe et al. 1998, *top left*; Siess et al. 2000, *top right*; Tognelli et al. 2011, *bottom left*; Baraffe et al. 2015; *bottom right*). For each model isomasses (solid lines) and isochrones (dashed lines) are plotted. We highlight the nearest tracks available corresponding to our dynamical mass values. The theoretical masses are consistent with our dynamical estimates just at the extreme of their uncertainties.

masses of the components of this system. We note that the proximity of the two stars near periastron (~20−40 mas in the last four years) has prevented an appropriate sampling of the relative orbit until the recent use of more precise interferometric techniques: aperture-masking (Evans et al. 2012) and VLBI (this work). The results of our orbital analysis yields values of 0.70±0.07 $M_{\odot}$ and 0.45±0.04 $M_{\odot}$ for components A and c, respectively, which are larger than the theoretical values predicted by PMS evolutionary tracks. The amount of this disagreement is ∼10% for component A, and 20−40% for component c, contributing to the observational evidence that PMS models underpredict the masses of systems with masses below 1.2 $M_{\odot}$. Remarkably, our study allowed us to obtain a revised and more precise value of the parallax (31.4±0.5 mas), solving a long-standing discussion about the distance to this system.

Out of the six radio stars detected in the AB Dor-MG (Table 3.3), HD 160934 A/c is the second pair whose two components are radio emitters (after AB Dor Ba/Bb; see Chapter 5); in addition, other two stars with radio emission are binaries (AB Dor A and EK Dra; see Chapters 5 and 7, respectively). This poses some questions about a possible relationship between radio emission (i.e., activity levels) and binarity in young late-type stars. Since the radio emission of our stars mostly originates from a fast rotation in presence of a strong magnetic field, a possible scenario for a radio binary would imply that both components originated from the fragmentation of a collapsing highly-magnetized, fast-rotating cloud. If fragmentation has to occur to form the binary star (according to Boss 2002, high magnetic fields do not hamper fragmentation, instead, they seem to contribute to the formation of binary or multiple systems) the angular momentum should be distributed in such a way that both components retain high levels of rotation; likewise, they also should retain a strong magnetic field. This guarantees that the two members of the binary maintain high levels of radio emission. Finally, we note that an improvement in the sensitivity of the radio interferometric arrays will be essential to increase significantly the statistics of radio binaries.

Chapter 7

Other young, active radio stars in the AB Doradus moving group

As reported in Section 2.3, six stars of our sample of the AB Dor-MG presented detectable levels of radio emission. Three of those stars (AB Dor A, AB Dor B, and HD 160934) have been treated in the past chapters; we present here the results of the rest of our sample, i.e., EK Dra, LO Peg, and PW And. Aside of the reanalysis of the existing VLA data corresponding to these stars (published in the case of EK Dra; Güdel et al. 1995), our main contribution consists on the study of the compact radio emission using VLBI observations. For the known binary EK Dra, our intention is to revise the orbital elements to estimate the dynamical masses of the system, in the same manner we have done for AB Dor A, AB Dor B, and HD 160934. For the single stars PW And and LO Peg, our goal is to search for unseen companions to within a few milliarcseconds from the central objects; if any of these stars is a close binary, they will become prime targets for further astrometric monitoring.

We anticipate that not all the stars are detected in all VLBI observing epochs, so the determination of the dynamical masses is out of hand in these cases. Nevertheless, when the stars have been detected, we have been able to set bounds to their kinematics. Some important conclusions about the radio emission in the AB Dor-MG are also drawn at the end of the chapter.

Table 7.1 Journal of observations

Source	Date (Epoch)	VLA configuration	UT Range	Beam size [arcsec]	P.A. [°]
EK Dra	29 January 1993	AB	01:25 - 12:00	0.74×0.33	−72.8
LO Peg	5 May 1996	CD	12:50 - 18:10	7.63×3.44	82.0
PW And	16 Sep 1993	CD	06:00 - 16:00	10.90×3.28	80.5
Source	Date (Epoch)	VLBI array[a]	UT Range	Beam size [mas]	P.A. [°]
EK Dra	29 Oct 2012	Ef, Wb, Jb, On, Mc, Nt, Tr, Ys, Sv, Zc, Bd, Ur, Sh	07:30 - 17:30	2.19×1.71	−34.1
"	27 May 2013	"	17:45 - 03:45	1.30×1.02	−30.5
"	5 Mar 2014	"	16:30 - 02:30	1.79×0.96	−13.0
LO Peg	23 Oct 2014	Ef, Wb, Jb, On, Nt, Tr, Ys, Sv, Zc, Bd, Sh, Hh	13:00 - 23:00	1.21×0.89	−84.4
Pw And	26 Oct 2014	Ef, Wb, Jb, On, Nt, Tr, Ys, Sv, Zc, Bd, Sh	16:30 - 02:30	4.63×2.84	0.4

Notes. [a]: Ef: Effelsberg, Wb: Westerbork, Jb: Jodrell Bank, On: Onsala, Mc: Medicina, Nt: Noto, Tr: Torun, Ys: Yebes, Sv: Svetloe, Zc: Zelenchukskaya, Bd: Badary, Ur: Urumqi, Sh: Shanghai, Hh: Hartebeesthoek.

7.1 Observations and data reduction

7.1.1 VLA observations

We analyzed archival VLA data[1] of the stars EK Dra, LO Peg, and PW And observed at 8.4 GHz in AB (EK Dra) and CD (LO Peg and PW And) configurations on 1993 January 29, 1996 May 5, and 1993 September 16, respectively (see Table 7.1). In all cases, the effective bandwidth was 50 MHz and left and right circular polarizations were collected. For EK Dra the observation lasted 10.5 h, the source 3C48 was used as primary flux calibrator, and the source 1435+638 was selected as phase calibrator. For LO Peg, the observation lasted 5.5 h, the source 0137+331 was used as primary flux calibrator, and the source 2115+295 was selected as phase calibrator. For PW And, the observation lasted 10 h, and the flux and phase calibrators were 0137+331 and 0029+349, respectively.

To reduce all three experiments, we used standard routines of the Astronomical Image Processing System (AIPS) program, of the National Radio Astronomy Observatory (NRAO). We flagged bad data, we determined the flux density of the flux calibrator, we calculated the flux density of the phase calibrator from the primary flux calibrator, and we used the solutions derived from the calibrators to calibrate the amplitudes and phases of the target through linear interpolation. These calibrated data were imported to the *DIFMAP* software-package (Shepherd 1994) to obtain the images of the stars. These resulting images are shown in Fig. 7.1, 7.10, and 7.7 and are discussed in Section 7.2.

---

[1] Projects AG0377, ADA000, and ABO691 available at the VLA data archive https://archive.nrao.edu/archive/advquery.jsp

7.1.2 VLBI observations

The previous VLA observations certified the presence of radio emission on our set of stars; to study their compact structures, we carried out follow-up VLBI observations of EK Dra, LO Peg, and PW And at 5 GHz between 2013 and 2014 with the EVN (see Table 7.1). Each experiment recorded an overall time of 10 h with a rate of 1024 Mbps (two polarizations, eight subbands per polarization, 16 MHz per subband, two bits per sample). After the observation, the data were correlated with the EVN MkIV data processor at the Joint Institute for VLBI in Europe (JIVE), Dwingeloo, The Netherlands.

As we are studying weak sources, we used the phase-referencing technique to facilitate its detection; for that, we interleaved scans of the target sources with ICRF quasars. The quasars selected were J1441+6318, J2125+2442, and J0015+3216 for EK Dra, LO Peg, and PW And, respectively (separated by 1.04°, 1.87°, and 1.48°, respectively). The cycles target-calibrator-target lasted about six minutes in all cases.

We reduced each experiment using AIPS in a standard procedure. The initial reduction included amplitude calibration using system temperatures and antenna gains, corrections of parallactic angle, and ionosphere. We applied fringe-fitting on the calibrator to determine phase offsets and applied the solutions to the target source. Later, we imported the resulting data to *DIFMAP* to obtain uniformly-weighted maps of the calibrator (Fig. 7.2, 7.11, and 7.8). We obtain the image through a process of self-calibration iterations of the amplitude and phase with deconvolutions using the CLEAN algorithm, that allowed us to determine both the amplitude scaling corrections and self-calibrated phase for each antenna. Back to AIPS, we applied these corrections to the target source to obtain the phase-referenced naturally-weighted images (Fig. 7.3 and 7.9). We analyze the details in the next section.

7.2 Discussion on individual sources

7.2.1 EK Draconis

EK Dra (=HD 129333) is an active, G1.5 V star with a rapid rotation (2.6 days) (Järvinen et al. 2005). The binarity of this star (which components are EK Dra A/B, separated $0.''74$) was discovered for the first time through radial velocity variations by Duquennoy & Mayor (1991). Metchev & Hillenbrand (2004) confirmed the existence of these components from IR imaging. Several radial velocity studies of this star have been carried out (Duquennoy & Mayor 1991, Dorren & Guinan 1994, Montes et al. 2001, König et al. 2005). In particular, Köning et al. (2005) combined these radial velocity data with his data of speckle interferometry to

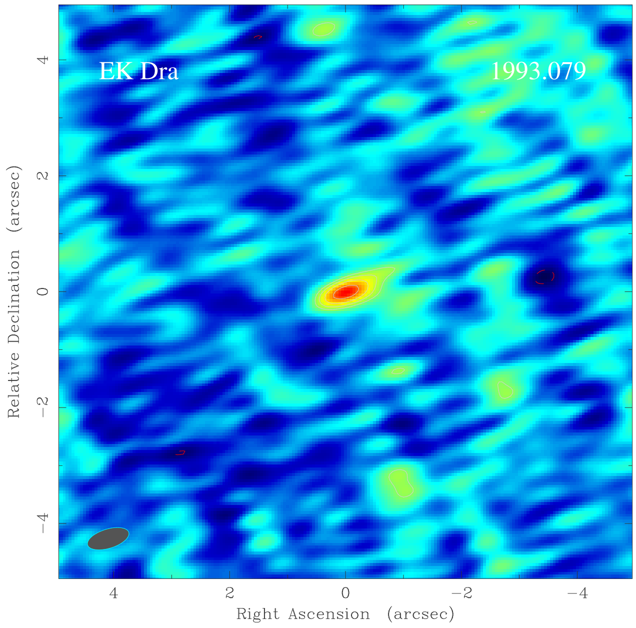

Fig. 7.1 VLA 8.4 GHz image of EK Dra taken on 1993.079. The lowest contour level corresponds to twice the statistical root-mean-square noise (0.02 mJy beam^{-1}) with a scale factor between contiguous contours of $\sqrt{2}$. The peak flux density in the image is 0.18 mJy/beam. The restoring beam (shown in the bottom-left corner) is an elliptical Gaussian of 0.74 × 0.33 arcsec (PA −72.°8).

derive masses of 0.9±0.1 $M_\odot$ and 0.5±0.1 $M_\odot$, for the primary and secondary, respectively, a period of 45±5 yr, and a semimajor axis of 14.0±0.5 AU.

The VLA image (Fig. 7.1) shows EK Dra as an unresolved radio emitter with an integrated flux of 0.21 mJy (the radio emission of EK Dra A at radio wavelengths is known and reported in Güdel et al. 1995). Because of the small separation of both components of the binary at the epoch of observation, the components A and B appear to be blended on the map. Besides this, we could only detect the component A in the first of our three VLBI epochs of observations (2012.827). The image yields a flux density of 0.06 mJy, with an upper bound to the radio emission of the component B of 0.02 mJy (Fig. 7.3). The upper bounds to the radio emissions of the star in the second and third epochs are 0.01 and 0.02 mJy, respectively. The non detection of EK Dra in the last two VLBI epochs can be a consequence of the variable behavior of the radio emission.

Direct imaging with AstraLux at the Calar Alto Observatory

We also carried out observations of EK Dra with the Lucky Imaging camera AstraLux at the Calar Alto 2. 2m telescope. As explained in Chapter 6 (Section 6.2.1), the lucky imaging

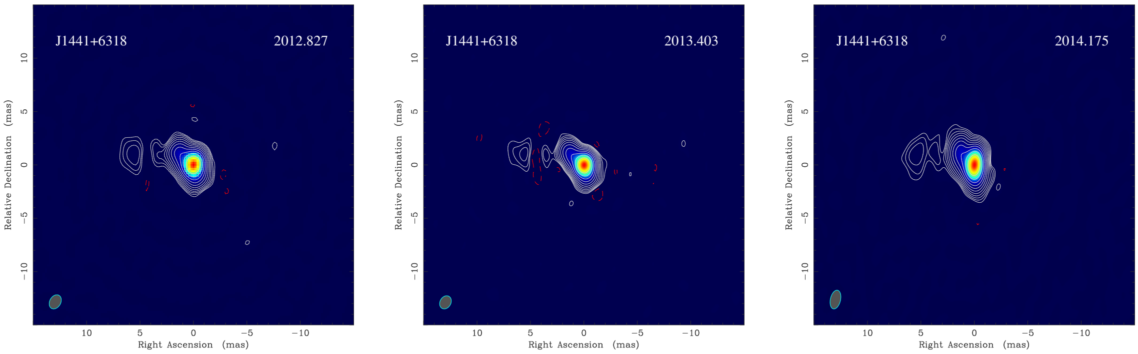

Fig. 7.2 EVN 5 GHz images of J1441+6318 (calibrator of EK Dra) taken on 2012.827, 2013.403, and 2014.175, respectively. In each map, the lowest contour level corresponds to 5 times the statistical root-mean-square noise (0.3, 0.4, and 0.4 mJy beam^{-1}) with a scale factor between contiguous contours of $\sqrt{3}$. The peak flux densities in the images are, respectively, 0.17, 0.17, and 0.19 mJy beam^{-1}.

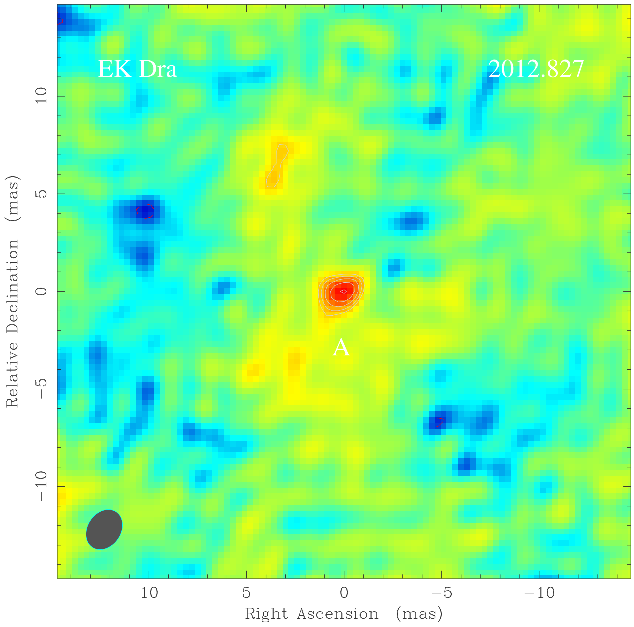

Fig. 7.3 EVN 5 GHz image of EK Dra taken on 2012.827. The lowest contour level corresponds to 3 times the statistical root-mean-square noise (0.02 mJy beam^{-1}) with a scale factor between contiguous contours of $\sqrt{2}$. The peak flux density in the image is 0.06 mJy beam^{-1}. The restoring beam (shown in the bottom-left corner) is an elliptical Gaussian of 2.19 × 1.71 mas (PA −34.°1).

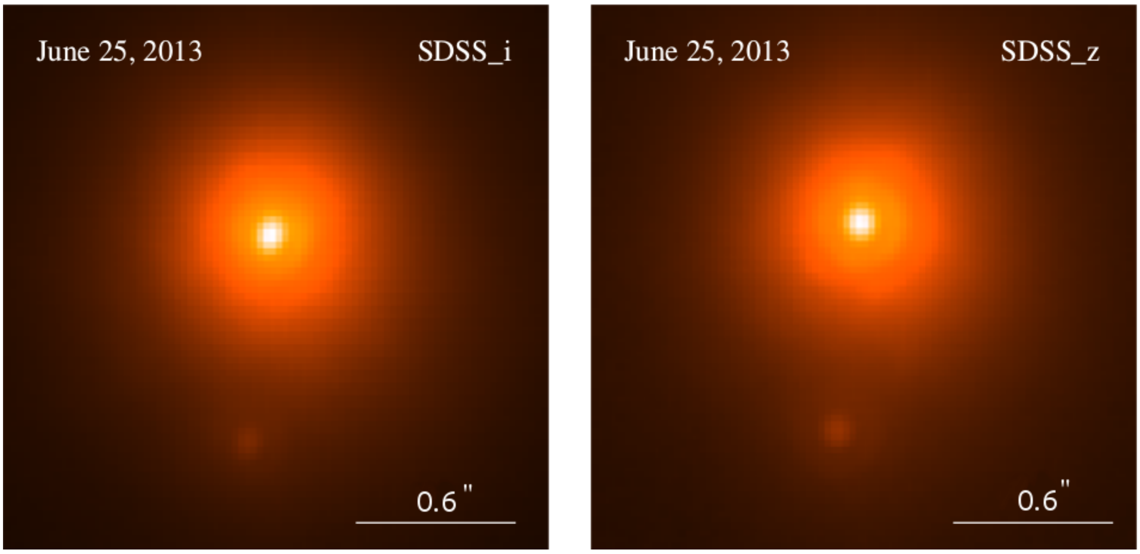

Fig. 7.4 AstraLux SDSS_i and SDSS_z images of the binary star EK Dra in 2013; North is up and East is to the left. Both components of the star, component A (north) and B (south), are clearly detectable.

technique permits to obtain an image relatively unaffected by atmospheric turbulences. We observed the star on June 24, 2013 with the SDSS_i and SDSS_z filters. The data consisted of 10000 individual frames with 30 ms exposure time each and we used 512×512 pixel frame. For each one of the filters, the final images, constructed by combining the best quality images, are shown in Fig. 7.4, where we could detect both components of the star.

Kinematics of EK Dra

We have used our AstraLux relative position of EK Dra to revisit the orbital motion between components A and B. This position is shown in Table 7.2 along with already published relative positions of EK Dra A/B, mostly resulting from speckle interferometry observations (König et al. 2005). We performed a weighted least-squares analysis similar to those presented in Chapters 5 and 6, simplified in this case to deal with only relative positions. Table 7.3 shows the resulting orbital elements and the estimate of the combined mass of the system (m_A+m_B = 1.38±0.08 $M_\odot$, using the *Hipparcos* distance 33.94±0.72 pc). Plots of the relative orbit can be seen in Fig. 7.5 and Fig. 7.6. Both the orbital elements and the mass estimates coincide with those reported by König et al. (2005) within uncertainties. We note that although our new position extends twofold the time baseline of the orbital monitoring, the motion of B around the main star is very slow, indicating that the components are near the apoastron.

Table 7.2 Compilation of astrometric measurements for the EK Dra system

	Relative positions EK Dra B − EK Dra A			
Epoch	Instrument	$\Delta\alpha$ (mas)	$\Delta\delta$ (mas)	Reference
1991.2135	1D	+0.030±0.020	−0.280±0.015	(1)
1992.1232	1D	+0.045±0.022	−0.310±0.015	(1)
1993.7611	MAGIC	+0.050±0.010	−0.453±0.015	(1)
1994.0712	MAGIC	+0.051±0.004	−0.483±0.010	(1)
1994.9501	MAGIC	+0.040±0.004	−0.499±0.005	(1)
1997.8926	MAGIC	+0.059±0.008	−0.644±0.012	(1)
2001.1123	OMEGA Cass	+0.085±0.007	−0.674±0.005	(1)
2001.8406	OMEGA Cass	+0.074±0.013	−0.705±0.012	(1)
2002.8049	OMEGA Cass	+0.102±0.012	−0.718±0.009	(1)
2013.4820	AstraLux	+0.081±0.008	−0.773±0.008	(2)

Notes. (1) König et al. (2005) using the 3.5 m-telescope on Calar Alto; (2) This work.

Table 7.3 Estimates of the orbital parameters of EK Dra

Parameter	Value
P (yr):	47.9 ± 0.9
a_{rel} ($''$):	0.434 ± 0.003
e:	0.812 ± 0.009
i (°):	89 ± 1
ω (°):	180 ± 1
Ω (°):	−186 ± 1
T_0:	1986.2 ± 0.1

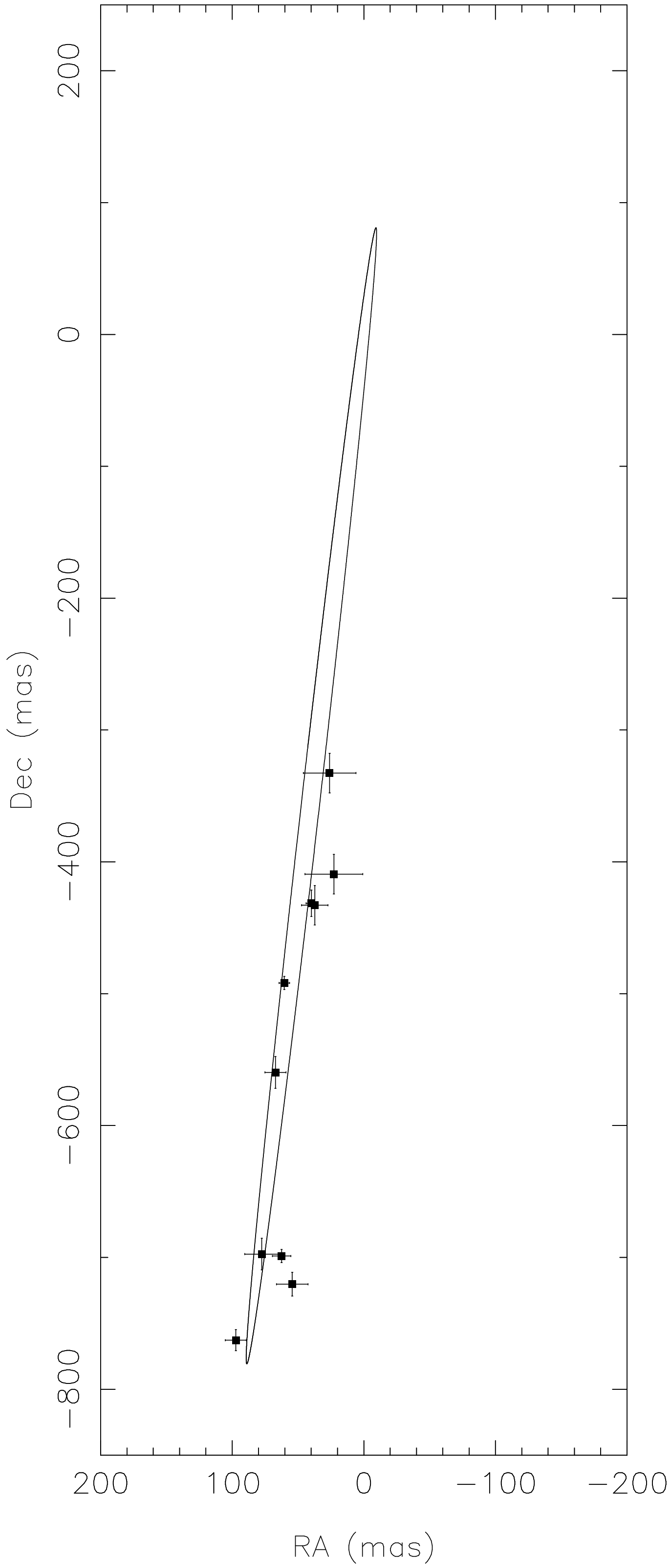

Fig. 7.5 Relative orbit for the binary EK Dra using the orbital elements in Table 7.3. EK Dra A component is located at the origin.

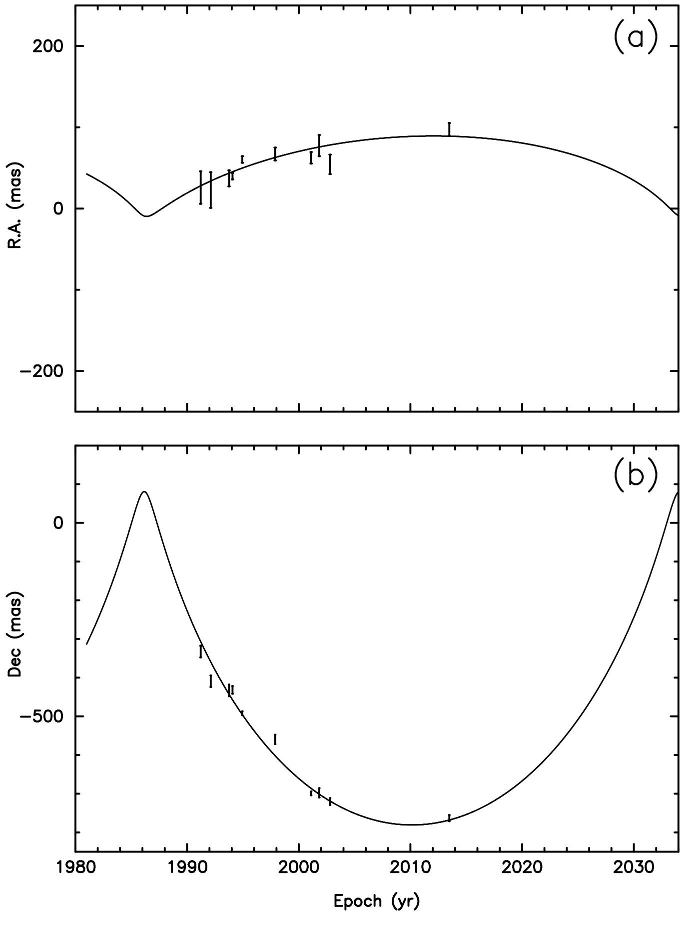

Fig. 7.6 Orbital motion of the binary EK Dra in right ascension (a) and declination (b). The line corresponds to the least-square fitted values of Table 7.3.

7.2.2 PW Andromedae

PW And (=HD 1405) is a chomospherically very active star, with a spectral type K2V, that displays a fast rotation (1.75 days) (Montes et al. 2001). Strassmeier et al. (1988) included this star as a possible binary, however, radial velocity studies (Griffin 1992, López-Santiago et al. 2003) discard the presence of a close, interacting companion, showing that the chomospheric activity is due to PW And itself. Moreover, Evans et al. (2012) explored the inner region of the star with speckle interferometry excluding the presence of companions at separations larger than 20 mas.

Regarding the radio observations of this star, a VLA image (Fig. 7.7) reveals a flux density of 0.34 mJy. Our EVN image, meanwhile, shows an unresolved source that should correspond to PW And, with a flux density of 0.17 mJy. Since our EVN observation does not show any companion to PW And, we can extend the absence of companions down to the resolution of our array, ~5 mas, at a flux density limit level of 0.01 mJy. Given the apparent single character of the star, we did not propose further EVN observations of this source in the frame of this work (dedicated to monitor binary/multiple systems). Still, once confirmed the presence of compact emission, the determination of a precise, VLBI-based parallax value, which supersedes that of *Hipparcos*, might be certainly of interest.

7.2.3 LO Pegasus

LO Peg (=BD+224402) is a young, active star with spectral type in the range K3V-K8V (Zuckerman & Song 2004, Pandey et al. 2005). It is also a rapidly rotating star with a rotation period of 0.42 days (Barnes et al. 2005). The first study of LO Peg was done by Jeffries et al. (1994), who concluded that there was no circumstellar matter around the star. Since then, Doppler images and studies of radial velocity have been carried out (Barnes et al. 2005, Piluso et al. 2008) and all of them consider LO Peg as a single star.

We can confirm the radio emission of this source with a VLA image (Fig. 7.10) that reveals a flux density of 0.45 mJy. In the VLBI image, nevertheless, the star could not be detected. The upper bound to radio emission of LO Peg in this observation is 0.08 mJy/beam. The reason of this non-detection could reflect the high variability of these active stars.

7.3 Conclusions

With the stars presented in this chapter, we have completed our high-resolution study of the six stars with radio emission introduced in Chapter 3. The main properties of these stars are shown in Table 7.4, including our calculated values of the absolute radio luminosity (obtained

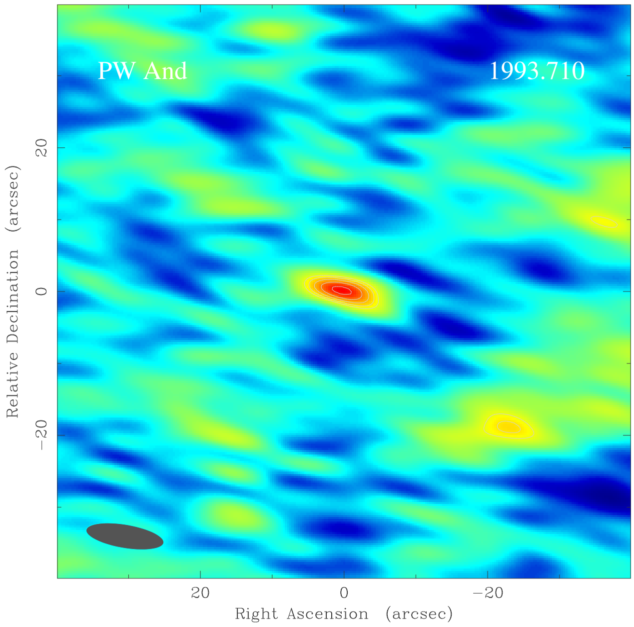

Fig. 7.7 VLA 8.4 GHz image of PW And taken on 1993.710. The lowest contour level corresponds to 3 times the statistical root-mean-square noise (0.02 mJy beam^{-1}) with a scale factor between contiguous contours of $\sqrt{2}$. The peak flux density in the image is 0.29 mJy/beam. The restoring beam (shown in the bottom-left corner of the map) is an elliptical Gaussian of 10.90 × 3.28 arcsec (PA 80.°5).

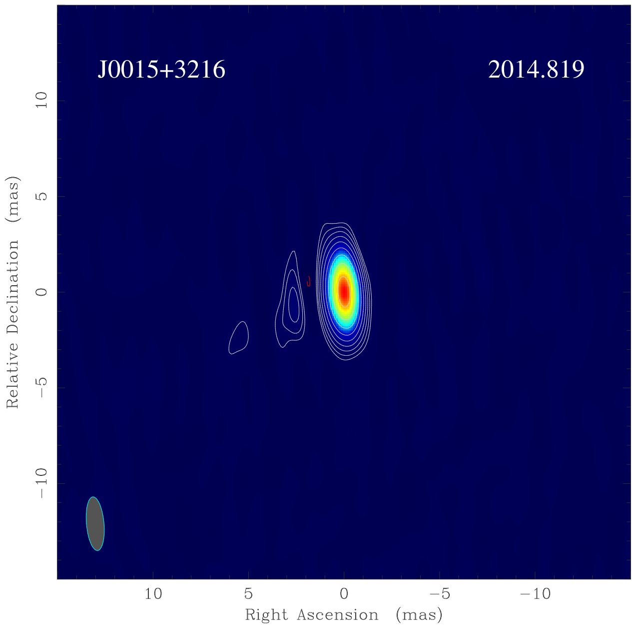

Fig. 7.8 EVN 5 GHz image of J0015+3216 (calibrator of PW And) taken on 2014.819. The lowest contour level corresponds to 3 times the statistical root-mean-square noise (0.3 mJy beam^{-1}) with a scale factor between contiguous contours of $\sqrt{3}$. The peak flux density in the image is 0.21 mJy/beam.

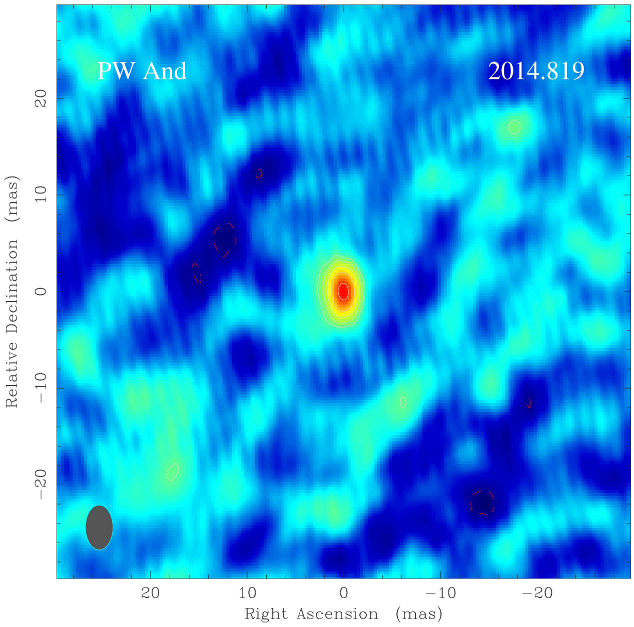

Fig. 7.9 EVN 5 GHz image of PW And taken on 2014.819. The lowest contour level corresponds to 3 times the statistical root-mean-square noise (0.01 mJy beam^{-1}) with a scale factor between contiguous contours of $\sqrt{2}$. The peak flux density in the image is 0.16 mJy beam^{-1}. The restoring beam (shown in the bottom-left corner of the map) is an elliptical Gaussian of 4.63 × 2.84 mas (PA 0.°40).

Table 7.4 Radio stars from the AB Doradus moving group

Name	T_b (K)	$v \sin i$ (km/s)	P_{rot} (d)	$\log L_X$ (erg/s)	$\log L_R$ (erg/s/Hz)	References
PW And	0.81×10^6	24	1.75	30.5	14.5	1,14,15
AB Dor Ba/Bb	2.25×10^6 / 2.60×10^6	9	0.33	–	14.6	2,5,6,7
AB Dor A/C	2.25×10^6 / –	44	0.514	30.2 - 32	15 - 16	2,3,4
EK Dra A/B	0.73×10^6 / –	16.5	2.78	29.92	14.6	1,8,9
HD 160934 A/c	0.72×10^6 / 1.4×10^6	17	1.8	29.39	14.4	2,10,11,12
LO Peg	–	60	0.42	30.2	14.7	13,14,15

Notes. (1) Montes el al. (2001); (2) Zuckerman & Song (2004); (3) Guirado et al. (2006); (4) Lim & White (1995); (5) Lim (1993); (6) Janson et al. (2007); (7) Azulay et al. (2015); (8) Güdel et al. (1995); (9) König et al. (2005); (10) Hormuth et al. (2007); (11) Evans et al. (2012); (12) Azulay et al. (2014); (13) Jeffries et al. (1994); (14) Wichmann et al. (2003); (15) VLA data archive.

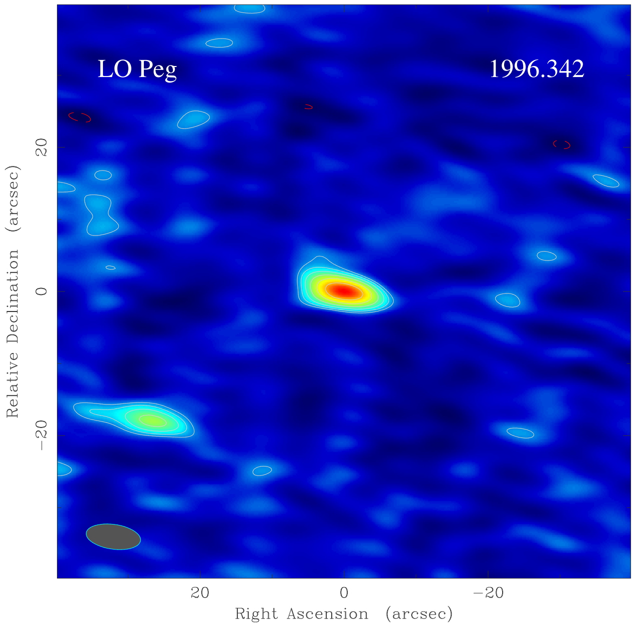

Fig. 7.10 VLA 8.4 GHz image of LO Peg taken on 1996.342. The lowest contour level corresponds to twice the statistical root-mean-square noise (0.02 mJy beam^{-1}) with a scale factor between contiguous contours of $\sqrt{2}$. The peak flux density in the image is 0.42 mJy/beam. The restoring beam (shown in the bottom-left corner of the map) is an elliptical Gaussian of 7.63 × 3.44 arcsec (PA 82.°0).

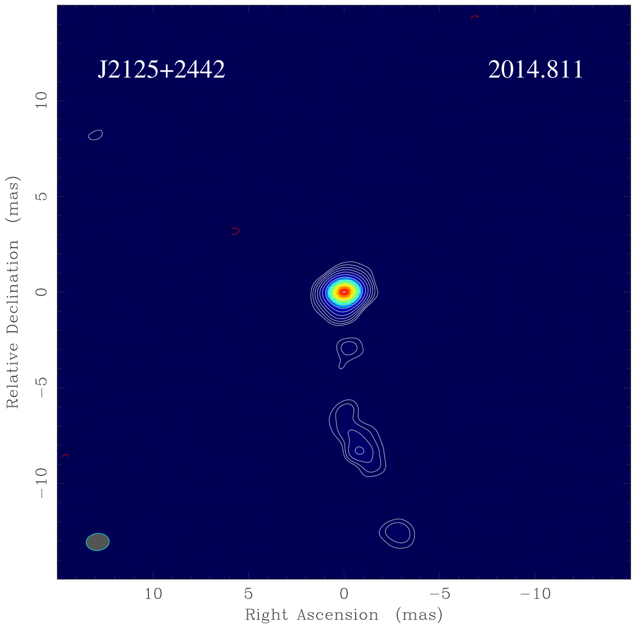

Fig. 7.11 EVN 5 GHz image of J2125+2442 (calibrator of LO Peg) taken on 2014.811. The lowest contour level corresponds to 3 times the statistical root-mean-square noise (0.2 mJy beam^{-1}) with a scale factor between contiguous contours of $\sqrt{3}$. The peak flux density in the image is 0.11 mJy/beam.

from the VLA flux and the *Hipparcos* distance) and the brightness temperature (obtained from the VLBI angular size when the source is detected). While AB Dor A, AB Dor B, and HD 160934 resulted to be intense radio emitters, detected at all observing epochs (and so it is PW And, also detected in our unique VLBI epoch of observation), we have found that EK Dra (in 2 out 3 epochs) and LO Peg did not display detectable levels of radio emission. These non-detections might be just the reflect of the variability of the radio emission, since, as seen in Table 7.4, neither the distance, rotation period nor X-ray luminosity are significantly different in these two stars with respect to the other radio emitter systems. Therefore, further monitoring of these non-detected stars would not be as efficient, in terms of kinematical studies, as in the cases presented in Chapters 5 and 6. The same conclusion applies to PW And, given its apparent non-binarity (even counting with a clear VLBI detection).

On the other hand, from the brightness temperatures displayed in Table 7.4, we can conclude that the radio emission has a non-thermal origin (see Appendix 1). This fact, along with the rapid rotation values and saturated levels of X-ray luminosity L_X displayed also in the table, favor the existence of an intense magnetic activity of the stellar corona, in turn responsible of the presence of this radio emission, apparently generated by gyrosynchrotron emission from non-thermal, accelerated electrons (Lim 1994; Güdel et al. 1995).

Chapter 8

Summary and outlook

8.1 Summary

Throughout this thesis, we have presented the results of our study of several PMS stars belonging to the AB Dor-MG. We have used radio and infrared observations with a special focus in the use of advanced VLBI techniques. The analysis included data calibration, imaging, and astrometry, the latter based on phase-referencing techniques. When it was possible, we determined the stellar masses and discussed these results and their impact in theoretical models of stellar evolution. The main results obtained are summarized below:

1. **We have observed, for the first time, the compact radio emission originated from each component of the PMS binary systems AB Dor Ba/Bb and HD 160934 A/c** by means of a series of VLBI observations with the EVN/LBA. So far, this radio emission had only been detected with connected interferometers, whose resolution was not enough to discriminate both components. Additionally, compact radio emission has been also detected in the PMS radio stars EK Dra and PW And. As indicated by its rapid rotation and saturated levels of X-ray luminosity, our stars must share an intense coronal magnetic activity. From this evidence, along with the brightness temperatures associated to our VLBI observations, we can reasonably infer that the origin of the radio emission must be similar in all the observed stars, that is, extreme magnetic activity of the stellar corona that triggers gyrosynchrotron emission from nonthermal, accelerated electrons (Lim 1994; Güdel et al. 1995).

2. **We have estimated the dynamical masses of AB Dor Ba/Bb, AB Dor A/C, and HD 160934 A/c**. The values obtained are 0.28±0.05 $M_\odot$ and 0.25±0.05 $M_\odot$, for the pair AB Dor Ba/Bb, 0.894±0.040 $M_\odot$ and 0.090±0.005 $M_\odot$, for AB Dor A/C, and 0.70±0.07 $M_\odot$ and 0.45±0.04 $M_\odot$ for HD 160934 A/c. The previous results are the

consequence of a combined analysis of our VLBI data and previously-published NIR relative positions. The combination of both techniques provided precise values of the orbital elements of both the absolute and relative orbits, from which the dynamical masses were estimated.

3. **We have found observational evidence that PMS evolutionary models underpredict the mass of PMS stars by a 10–40%.** We have used NIR photometry to locate our stars in H-R diagrams to facilitate the comparisons with evolutionary tracks. We have considered the PMS models of Baraffe et al. (1998), Siess et al. (2000), Chabrier et al. (2000), Montalbán & D'Antona (2006), and Tognelli et al. (2011, 2012). According to our work, this disagreement between theoretical and dynamical masses holds for masses from ~0.9 $M_\odot$ (AB Dor A) down to 0.25 $M_\odot$ (AB Dor Bb). For all cases, the reported disagreements are less than twice the standard deviation of our measurements, whose largest contribution comes from the errors in the determination of the effective temperature and absolute magnitude.

4. **We have found evidence of a possible relationship between radio emission and binarity.** A significant fraction of the AB Dor-MG stars detected in our sample (4 out of 6) resides in binary systems. Considering that a similar result has been found at least for other stellar association (the Pleiades cluster; Melis et al. 2013), this suggests a possible relationship between radio emission and binarity in young late-type stars. Fast rotation and strong magnetic field appear to be the key parameters to explain such a relationship as they favor both the triggering of radio emission and the fragmentation of the original rotation cloud in the earlier stages of the star formation. This is the likely scenario for AB Dor B and HD 160934, the systems whose two components are radio emitters. It would imply that the angular momentum of the rotating cloud should be distributed in such a way to maintain high rotation rates in the two members of the binary form after fragmentation, so that they can display compact radio emission. For AB Dor B in particular, we speculate that the components Ba and Bb were earlier close binaries forced to shrink and merge via mutually induced dynamical perturbations, keeping part of the angular momentum as a very rapid rotation, responsible in turn for the radio activity.

8.2 Future work

The inclusion of new large telescopes in present arrays, such as Tianma or Sardinia, the improvements in data bit rate and, therefore, in sensitivity and image fidelity, and the arrival of new radio telescopes, namely the Square Kilometre Array (SKA) and the Atacama Large Millimeter/submillimeter Array (ALMA), will increase dramatically the amount and quality achieved with present instruments. Combined with dedicated calibration techniques, these new arrays will allow the access of radio astronomy to new astrophysical scenarios. This progress in the instrumentation together with the increasing number of objects belonging to young associations (5−100 Myr) in the vicinity of the Sun (15−50 pc) where the presence of radio emission is favored, will allow us to study in more detail young and low-mass objects helping to increase our knowledge about the earliest stages of stellar evolution.

Astrometry with SKA

The SKA is a global radio telescope project that is being built in Australia and South Africa. This instrument will have a total collecting area up to one million square metres and stations extending a maximum baseline of at least 3000 km from a central core. It will operate over a a frequency range of approximately 0.1 to 25 GHz, it will have a wide field of view (tens of square degrees, frequency dependent), and its size will make it 50 times more sensitive than any other radio instrument. The main science objectives that are going to carry out cover a wide range of fields from star formation until cosmology, including tests of general relativity.

From an astrometric point of view, that is what concerns us, the combination of sensitivity and wide field-of-view of the SKA will make possible μarc-second precision astrometry of thousands of stars. However, as stressed in Guirado et al. (2015), the application of Multiview techniques (Rioja et al. 2009; Dodson et al. 2013) appears essential to achieve such a high accuracies. According to the Multiview techniques, by observing simultaneously multiple calibrator sources with separation smaller than the antenna beam size, it is possible to correct the atmospheric distortions around the target, thereby providing significantly improved calibrations and enabling astrometric measurements.

Following to the planned configurations, the SKA Phase 1 (SKA1), with baseline length up to 200 km, will have the capability for carrying out Multiview observations with an expected accuracy slightly below the milliarcsecond. To approach the μas accuracy, the resolution of SKA1 needs to be enhanced with the addition of VLBI stations to form longer baselines. The full development of the astrometric performances will have to wait until completion of SKA2 realization, which will extend SKA1 to baselines up to 3000 km.

The role of the SKA in terms of calibration of the stellar mass-luminosity relation for PMS objects will be very relevant. Since SKA astrometry will determine or refine measurements of the distance and/or orbital motion of hundreds of stars belonging to nearby moving groups and taking into account that the age of these objects is precisely determined, the dynamical masses obtained by successive SKA observations would impose strong constraints to stellar evolutionary models, in a similar way that we have done in this work. Additionally, the μas-accuracy provided by SKA1+VLBI or SKA2 would reveal low-mass objects, brown dwarfs or planets, around the sampled stars, whose mass could be measured with high precision.

Substellar objects with ALMA

ALMA is an astronomical interferometer of radio telescopes built in the Atacama desert, in northern Chile. It is composed by 66 high-precision antennas (of 12 m and 7 m diameter) operating at wavelengths of 0.32 to 3.6 mm, with a maximum distance between antennas that can vary from 150 m to 16 km. ALMA will allow us to study some of the coldest objects in the Universe, such as dusty molecular clouds where stars are born, formation and early evolution of planets in circumstellar disks, and some of the earliest and most distant galaxies.

In terms of the work developed in this thesis, stars members of nearby moving groups (ages 5−120 Myr) are excellent laboratories to study the late stage of the protoplanetary disk dissipation, the origin of debris disks, and the planet-building processes within environments that are likely similar to that of the early solar system. There are 100 or more known dusty debris disks around young nearby stars with various systems spanning the range from intermediate-mass to the stellar/substellar boundary. These systems, mostly placed in the southern hemisphere, are all suitable targets for ALMA and would complement nicely the GHz-observations projected with sensitive interferometers, like VLA and/or ATCA, and with VLBI/VLTI.

Actually, we have already made the first observations towards this research topic. At the time of writing, the VLA and the EVN have granted us time to observe the system VHS1256−1257 (Gauza et al. 2015), consisting in an 11.2 $M_{\rm Jup}$ exoplanet orbiting a radio-emitting 73 $M_{\rm Jup}$ brown dwarf (see Fig. 8.1). The VLA observations are directed to 1) the detection of radio emission in the known position of the exoplanet (through deep cm-observations), and 2) investigate the presence of thermal dust emission of a possible debris disk around the brown dwarf (using mm-observations). Complementarily, the EVN observations will serve to prove the compact radio emission of the host brown dwarf and to monitor its orbital motion. Even more, very recently the main star has been discovered to be a double system (Stone et al. 2016); the EVN observations will serve to obtain a precise orbit and, therefore, a dynamical mass determination of both substellar companions.

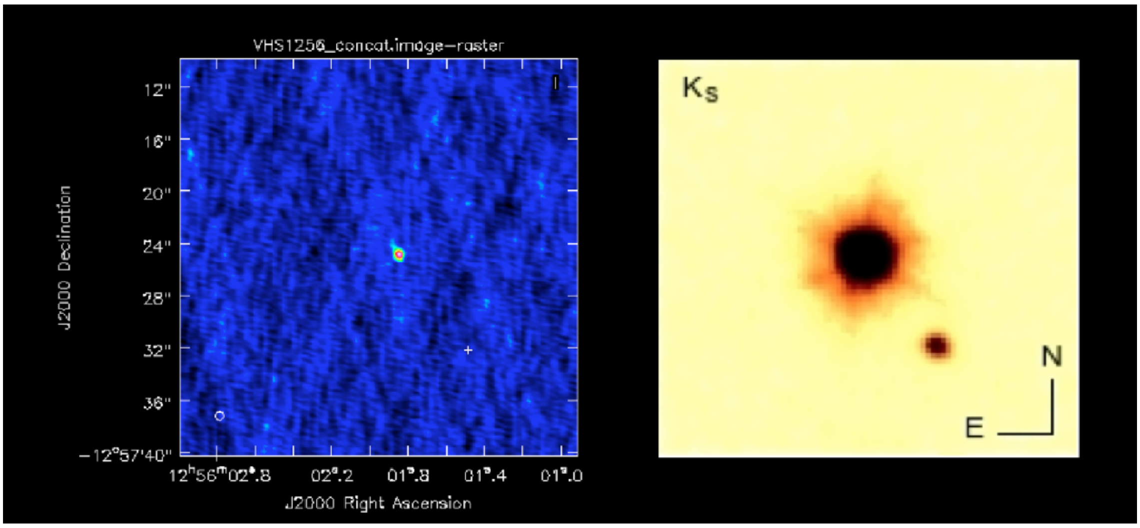

Fig. 8.1 VLA (8.4 GHz) image and VISTA image (Gauza et al. 2015) of the VHS1256-1257 system. The planetary companion is located at a projected angular distance of 8″ (102 AU). This location is marked with a ‘+’ symbol in the VLA map.

Appendix A

Stellar radio emission

Since the middle of the last century stellar radio astronomy has experienced a great progress with the observation of important astronomical phenomena thanks to improvements in instrumental sensitivity and angular resolution. The study of the radio emission processes that take place in some types of stars has an important incidence in our understanding of stellar evolution and the astrophysical mechanisms involved. Although the fraction of stars that emits at radio wavelengths is small, these studies provide an important complement to the observations obtained with other wavebands, all of which are indispensable for the stellar knowledge.

A.1 Radiative transfer

The propagation of radio waves is governed, as in other parts of the electromagnetic spectrum, by the laws of radiative transfer. This propagation of radiation across a medium can be described mathematically by the *equation of radiative transfer*, that is given by

$$\frac{dI_\nu}{d\tau_\nu} = -I_\nu + S_\nu, \tag{A.1}$$

where I_ν is the specific intensity, S_ν is the *source function*, given by $S_\nu \equiv \frac{j_\nu}{\alpha_\nu}$, where j_ν and α_ν the coefficients of emission and absorption, respectively, and τ_ν is the optical depth, defined by $d\tau_\nu = \alpha_\nu ds$, where ds is a differential element of length. If we take S_ν constant throughout the region under consideration and suppose that the flux incident on the region is no significant ($I_\nu(\tau_0) \approx 0$), the equation of radiative transfer has a simpler solution

$$I_\nu = S_\nu(1 - e^{-\tau_\nu}). \tag{A.2}$$

The medium is said to be optically thin when $\tau_\nu \ll 1$ and optically thick when $\tau_\nu \gg 1$. Being l an average column length along our line of sight through the region, we can distinguish two extreme cases, depending on the optical depth. For the optically thin regime we have that

$$I_\nu(\tau_\nu \ll 1) = S_\nu(1 - e^{-\tau_\nu}) \approx S_\nu \tau_\nu = \frac{j_\nu}{\alpha_\nu} \alpha_\nu l = j_\nu l \tag{A.3}$$

and for the optically thick regime, that

$$I_\nu(\tau_\nu \gg 1) = S_\nu(1 - e^{-\tau_\nu}) \approx S_\nu. \tag{A.4}$$

The emission and absorption coefficients, j_ν and α_ν, will vary according to the dominant physical processes, the energy distribution of radiating particles, and other parameters characterizing the emission region, like the magnetic field.

The *flux density* F_ν, that is one of the most interesting observational magnitudes, is the result of integrating the specific intensity over all solid angles

$$F_\nu = \int_{4\pi} I_\nu \cos(\theta) d\Omega. \tag{A.5}$$

The dimensions of the flux density are $\mathrm{erg\,s^{-1}\,cm^{-2}\,Hz^{-1}}$, although the usual unit in radio astronomy is the *Jansky* (Jy) (as well as its submultiples mJy and μJy), equivalent to $10^{-23}\,\mathrm{erg\,s^{-1}\,cm^{-2}\,Hz^{-1}}$.

The interior of the star behaves, for the purposes of radiation, like a black body. This radiation is known as *blackbody radiation* and depends only on the temperature T of the body. In this case, the equation of radiative transfer takes a specific form and its intensity, denoted by $B_\nu(T)$, is given by the Planck function

$$B_\nu(T) = \frac{2h\nu^3}{c^2} \frac{1}{e^{h\nu/kT} - 1}, \tag{A.6}$$

where ν is the frequency, k is the Boltzmann constant, h is the Planck constant, and c is the speed of light.

In case of radio waves, where $h\nu << kT$, the Planck function $B_\nu(T)$ adopts the simple form (*Rayleigh-Jeans approximation*)

$$B_\nu(T) = \frac{2k\nu^2}{c^2} T. \tag{A.7}$$

Integrating this specific intensity over the extension of a celestial object that subtends and angular radius of θ, we obtain the radio flux density F_ν at a frequency ν

$$F_\nu = 0.82 \times 10^{-12} \left(\frac{\nu}{[\mathrm{GHz}]} \right)^2 \left(\frac{\theta}{[mas]} \right)^2 T_B \qquad [\mathrm{Jy}], \tag{A.8}$$

where T_B is the brightness temperature of the radio source.

According to Eq. A.8, and for the usual angular size and temperature of normal stars, clearly they do not emit a significant fraction of its energy at radio wavelengths as a black body.

In general, the dependence of F_ν with the frequency is characterized over a limited spectral region by a power law of the form $F_\nu \propto \nu^\alpha$, where α is called the *spectral index* of the radiation. As we have seen in Eq. A.8, $\alpha = 2$ for blackbody radiation but it will take other values for different radiation mechanisms.

Continuum radiation mechanism

Considering only continuum emission (we will not consider line emission here), radiation mechanisms can be divided in two groups: *thermal and non-thermal.*

- Thermal emission, where the emitting particles have a thermal equilibrium distribution of energies. The most common mechanism is the "bremsstrahlung" or free-free (FF) emission, produced by the random encounters of electrons with ions in a plasma. The plasma temperature is found to be typically near 10^4 K. Other thermal mechanism is the gyroresonance emission or cyclotron (see next section).

- Non-thermal emission, where the particles have a non-thermal equilibrium distribution of energies. Non-thermal process includes gyrosynchotron and synchrotron emission (see next section) and plasma (coherent) emission, produced by collective motions in a plasma.

Table A.1 summarizes the spectral behaviour of the most common thermal and non-thermal processes in radio stars. A complete discussion of thermal and non-thermal radiation can be found in Rybicki & Lightman (1979); here we will focus on non-thermal radiation, concretely, in gyrosynchrotron radiation, which seems to be the main responsible of the radio emission detected in the stellar systems studied in this work.

Table A.1 Main characteristics of the emission mechanisms acting in radio emission (continuum)

Mechanism	Type	Spectral power (thick)	Spectral power (thin)	γ
Bremsstrahlung (free-free)	Thermal	$\propto \nu^2$	$\propto \nu^{0.1}$	
Cyclotron (thermal plasma)	Thermal	$\propto \nu^2$	$\propto \nu^{-8}$	
Gyrosynchrotron (power-law electron distribution)	Non-thermal	$\propto \nu^{5/2}$	$\propto \nu^{1.22-0.9p}$	$2-3$
Synchrotron (power-law electron distribution)	Non-thermal	$\propto \nu^{5/2}$	$\propto \nu^{(1-p)/2}$	$\gg 1$

A.2 Gyrosinchrotron emission

In presence of magnetic fields, the electrons of the plasma are forced to draw circles or spirals around the field lines. Therefore, the particle undergoes an angular acceleration that induces emission of radiation. For non-relativistic electrons, the gyrofrequency ν_e in terms of a magnetic field B is given by

$$\nu_e \equiv \frac{\omega_e}{2\pi} = \frac{eB}{2\pi m_e c} \approx 2.8 \times 10^6 B \quad \text{[Hz]}, \tag{A.9}$$

where c is the speed of light, e is the electron charge, m_e is the electron rest mass, and B is given in Gauss. The relativistic gyrofrequency is $\nu_{e,rel} = \nu_e/\gamma$, where $\gamma = 1/\sqrt{1-(v^2/c^2)}$ is the Lorentz factor.

Depending on the value of γ, the emission is divided into:

- *Cyclotron emission:* $\gamma \approx 1$, for non-relativistic electrons, tipically thermal electrons (T$_B$ up to 10^{20} K).

- *Gyrosynchrotron emission:* $\gamma \lesssim 2-3$, for midly relativistic electrons (T$_B$ up to 10^{10} K).

- *Synchrotron emission:* $\gamma \gg 1$, for ultrarelativistic electrons (T$_B$ up to 10^{12} K).

The gyrosynchrotron emission has an important role in the production of the radio emission of stellar objects. General expression for the emission and absorption coefficients are given in Ramaty (1969) and they are difficult to derive, since the simplifications of the non-relativistic and ultrarelativistic limits are no valid in this case. Approximate formulae have been given by some authors (Takakura & Scalise 1970; Dulk & Marsh 1982; Dulk 1985; Klein 1987), but all these approximations are highly restricted in their application.

Güdel (2002) provided simplified expressions for the emission and absorption coefficients derived from Dulk (1985) for the angle θ between the line of sight and the magnetic field equal to $\pi/3$: assuming a gas in which the emitting electrons have an isotropic pitch angle distribution and a power-law distribution in energy given by $N(E)dE = CE^{-p}dE$, where p is the *electron power-law index* and C is a quantity that varies with pitch angle, and considering

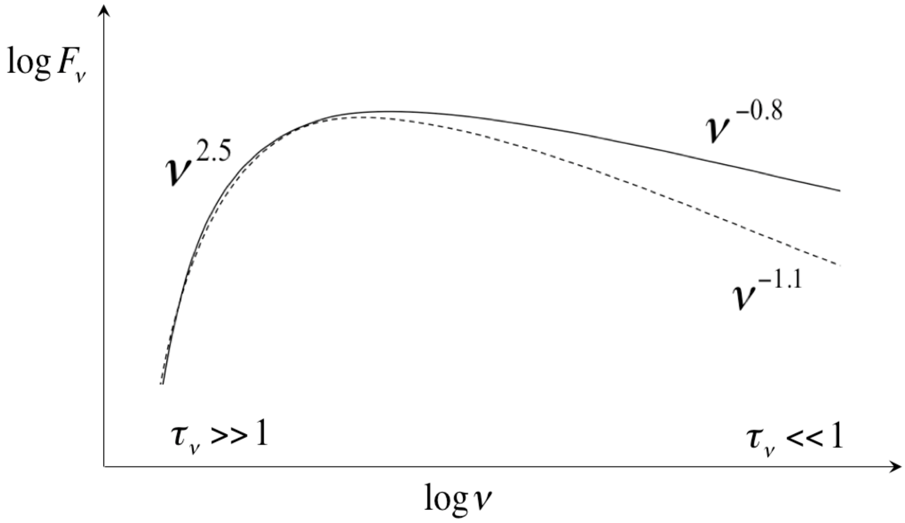

Fig. A.1 Comparison of the spectrum of synchrotron (continuous line) and gyrosynchrotron radiation (dashed line) showing the behaviour for optically-thick and optically-thin regimes. We adopted a typical value of $p = 2.6$ (see Table A.1).

the ranges $2 \lesssim p \lesssim 7$ and $10 \lesssim \nu/\nu_e \lesssim 100$, Güdel's expressions give accurate results and are given by

$$j_\nu \approx 10^{-31.32+5.24p} N B^{-0.22+0.90p} \nu^{1.22-0.90p}, \tag{A.10}$$

$$\alpha_\nu \approx 10^{-0.47+6.06p} N B^{0.30+0.98p} \nu^{-1.30-0.98p}, \tag{A.11}$$

where N is the total non-thermal electron number density above the low-energy cutoff $E_0 = 10\,\mathrm{keV} = 1.6 \times 10^{-8}$ ergs.

From these expressions, we can derive that the spectral index α is approximately $5/2$ at the optically-thick regime, meanwhile, α is $\sim 1.22 - 0.9p$ at the optically-thin regime. The gyrosynchrotron spectrum of a source with a power-law distribution can be obtained combining the two spectral limits and is shown in Fig. A.1. In practice, the maximum brightness temperature in objects emitting gyrosynchrotron is $\approx 10^{10}$ K.

A.3 H-R diagram for radio stars

The features of the radio emission from stars are nearly associated with their structure and evolutionary phase. In turn, the structure and evolutionary phase of a star is nearly associated

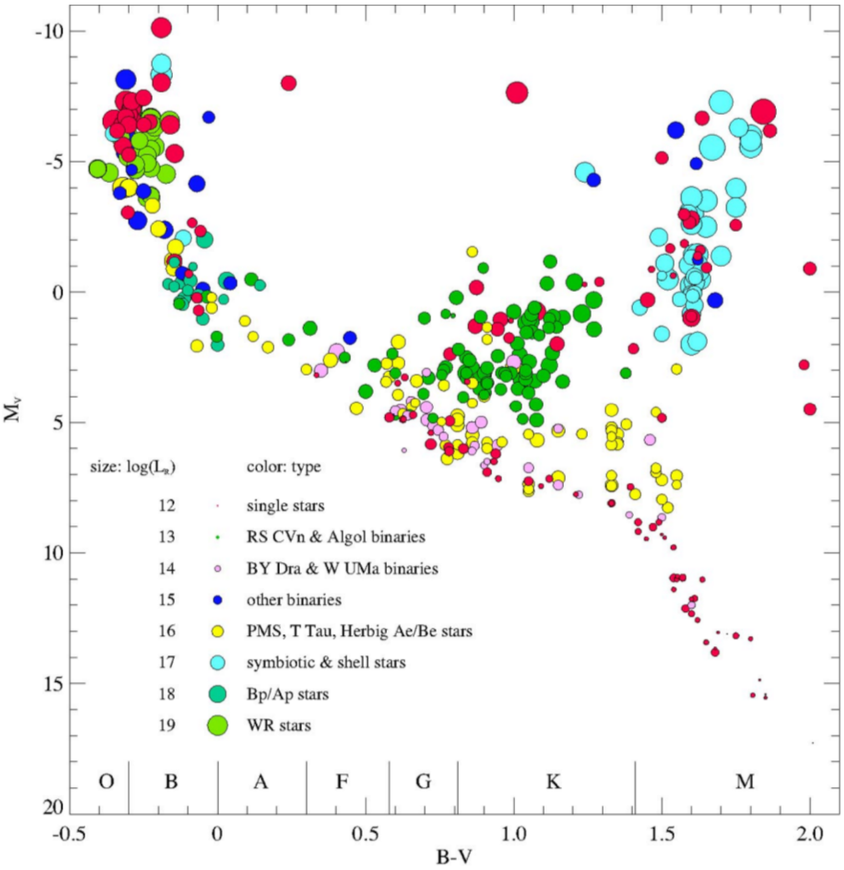

Fig. A.2 H-R diagram showing 440 radio-detected stars (Güdel 1995).

with its position in the H-R diagram. An H-R diagram taken from Güdel (1995) and based on stellar radio detections between 1 and 10 GHz obtained by Wendker (1995) is shown in Fig. A.2. The placement of the symbols is according to classical visual magnitude versus color (B-V) H-R diagram for stars, but the symbols themselves carry the information about the radio emission.

In the upper left part of the H-R diagram we find the massive and young O-B stars and the Wolf Rayet (WR) stars. In these stars, thermal FF emission is the responsible of the radio emission, due to ionized mass loss. Some of them also have non-thermal synchrotron emission produced by ultra-relativistic electrons and magnetic fields formed in the wind (Abbott et al. 1984, 1985; Leitherer & Robert 1991).

A small fraction of main sequence stars with spectral types B-F are sources of non-thermal emission. They posses a strong magnetic field and radio emission is detected from the interaction of this magnetic field with stellar winds. Other stars of the main sequence with spectral types B and A, known as peculiar stars or Bp-Ap stars, are also radio emitters. This stars are characterized by overabundances of some metals, such as strontium, chromium, and europium. They also have strong magnetic fields that might be the responsible of non-thermal radio emission.

At the coolest part of subgiant and giant area, radio emission of close binaries takes place. In this case, non-thermal gyrosynchrotron emission results from the collision of winds because both components experiment intense mass loss due to tidal influence. This occurs in detached binaries called RS Canun Venaticorum (RS CVn) stars, semi-detached binaries called Algol binaries, and contact binaries called W Ursae Majoris stars. Symbiotic stars (binaries with compact companion) are also in this region; these binaries present thermal FF radio emission produced because the hot star ionizes the wind of the cool companion.

At the lower end of the main sequence are located the called flare stars, namely, stars with intense flares emitting in all regions of the electromagnetic spectrum, typically of spectral class M. The mechanism of radio emission that they have is gyrosynchrotron emission produced in the intense flares.

Regarding the PMS stars, T Tauri stars are very young variable PMS stars of spectral types F, G, K, M. These stars are usually found in molecular clouds where star formation takes place. Most of T Tauri stars have circumstellar disks and appear to be sources of FF radio emission from ionized gas. Analogs of T Tauri stars in the higher mass range (A and B spectral type PMS stars) are called Herbig Ae/Be stars and are also sources of thermal FF emission due to the presence of circumstellar material.

Finally, and also within the PMS but more evolved than T Tauri stars, we find low-mass stars of spectral types K and M that emit at radio wavelengths too. These stars are the ones of interest for our study. They show evidence for the presence of mildly relativistic electrons radiating gyrosynchrotron emission in strong magnetic fields, which are triggered by a dynamo mechanism induced by fast rotation.

Appendix B

Orbital elements and dynamical masses in a binary system

A *binary star* is a stellar system composed by two stars orbiting around its mass center, since they are close enough that their movement is dominated by their mutual gravitational attraction. Studies of these systems are important, because allow to determine the dynamical stellar mass of their components. Among the methods used to calculate the dynamical masses of a binary system, those based on spectroscopy and/or astrometry are the most popular. Throughout this work, we have used techniques based on the radio emission of the observed stars to monitor with high precision the orbital position of the components of the binary.

B.1 Orbital elements in a binary system

The orbit of a binary system can be uniquely defined by seven parameters, called *orbital elements*. It describes the motion of one star relative to the other, that usually are denoted as *secondary or companion* and *primary*, respectively. The choice of the stars is arbitrary, although usually the brighter is assigned to the primary and the weakest, to the secondary. Observations of a binary star provide the projected separation between both components and the position angle (P.A.) of the secondary with respect to the primary, that defines the apparent orbit. Meanwhile, the orbit in which the main component is located at one focus is the true orbit. If we consider the plane through the primary star perpendicular to the line of sight of the observer, known as *reference plane*, the apparent orbit is the projection of the true orbit on to the reference plane (see Fig. B.1).

The orbital plane intersects the reference plane in a line called *line of nodes*. An orbit has two nodes in this line, the ascending and the descending, that are the points where the

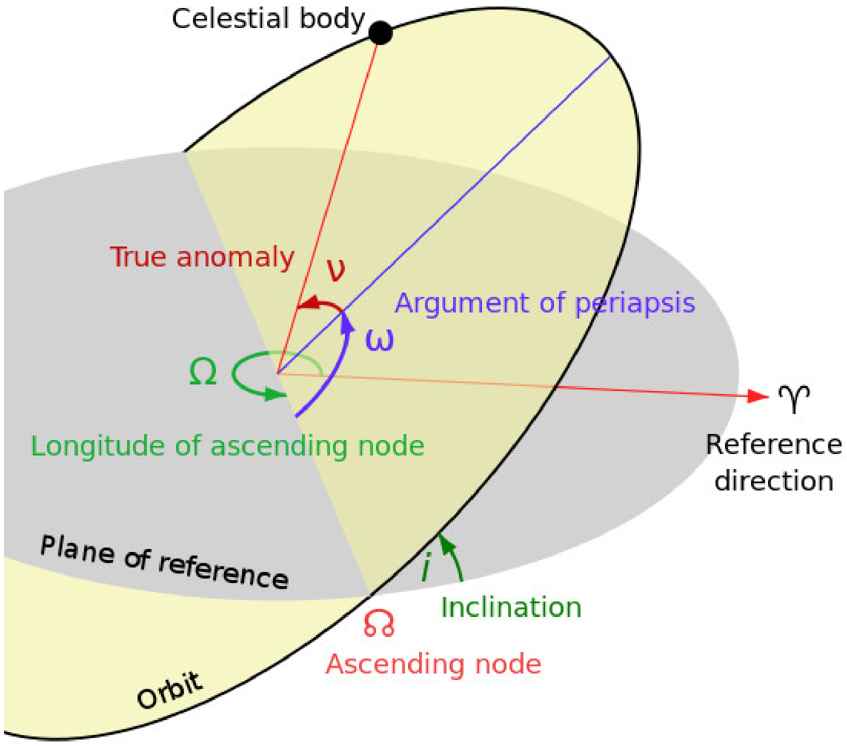

Fig. B.1 Orbital elements of a binary system. Credit: public domain.

secondary star crosses the reference plane. The orientation of the orbital plane is given by three orbital parameters:

- **Inclination** i, ($0 \leq i \leq 180°$): is the angle between the orbital plane and the reference plane, measured at the ascending node. When $0 \leq i \leq 90°$ the orbit is called *direct*, while if $90 \leq i \leq 180°$, is called *retrograde*.
- **Longitude of the ascending node,** Ω, ($0 \leq \Omega \leq 360°$): is the angle measured in the plane of the sky between the vernal point and the ascending node of the orbit.
- **Argument of periastron,** ω, ($0 \leq \Omega \leq 360°$): is the angle measured in the orbital plane from the ascending node to the periastron (point of the closest approach between the components during an orbit).

The shape and size of the orbit, meanwhile, is given by two orbital parameters:

- **Eccentricity** e, ($e = 0-1$): defines how much the orbit is elongated in comparison to a circle. The value $e = 0$ corresponds to a circle while the value $e = 1$ corresponds to a parabola.

- **Semimajor axis** a, ($a > 0$): is the longest diameter divided by two.

Moreover, the properties corresponding to time are given by two parameters:

- **Period** P, ($P > 0$): defines the time taken for an object to make one complete orbit around another object.

- **Time of periastron,** T_0: is the reference time that relates the periastron passage with a specific epoch.

In this case, the orbital elements have been defined for the relative orbit of the secondary respect to the primary. If the positions of each star can be measured with respect to the stellar background, the elements of the absolute orbits of both stars (orbits around the centre of mass) can be determined. The absolute orbits of each component has, respectively, semimajor axes a_1 and a_2 satisfying the relationship $a = a_1 + a_2$; each component also has their own argument of periastron, ω_1 and ω_2, respectively, satisfying the relationship $\omega_1 = \omega_2 + 180°$. The rest of the orbital elements of the absolute orbits are the same as those of the relative orbit.

B.1.1 The Thiele-Innes method

From the observation of the apparent orbit we have to estimate the orbital elements of the true orbit. A least-squares analysis of the observed orbital positions is usually done for this task, however, this procedure is highly non-linear. To overcome this inconvenient, one of the most common approaches is that based on the ***Thiele-Innes method*** (Hartkopf, McAlister, & Franz 1989; Wright & Howard 2009).

According to this method, given (P, T_0, e), the sky coordinates (x, y) of the secondary with respect to the primary (resulting from applying a sequence of rotations to transform the observer frame to the orbit plane frame, see e.g., Green 1985) at time t are defined by

$$\begin{aligned} x(t) &= AX(E) + FY(E) \\ y(t) &= BX(E) + GY(E), \end{aligned} \tag{B.1}$$

where

$$\begin{aligned} X(E) &= \cos(E) - e \\ Y(E) &= \sqrt{1-e^2}\sin(E), \end{aligned} \tag{B.2}$$

with $E(t)$ the eccentric anomaly, given by $\mu(t-T) = E(t) - e\sin(E)$, where $\mu = \frac{2\pi}{P}$, and A,B,F,G the four Thiele-Innes constants, defined as

$$\begin{aligned} A &= a(\cos(\Omega)\cos(\omega) - \sin(\Omega)\sin(\omega)\cos(i)) \\ B &= a(\sin(\Omega)\cos(\omega) + \cos(\Omega)\sin(\omega)\cos(i)) \\ F &= a(-\cos(\Omega)\sin(\omega) - \sin(\Omega)\cos(\omega)\cos(i)) \\ G &= a(-\sin(\Omega)\sin(\omega) + \cos(\Omega)\cos(\omega)\cos(i)). \end{aligned} \tag{B.3}$$

As seen in B.3, the Thiele-Innes constants behave linearly with respect to (x,y), so that they can be easily estimated through a least-squares fit. The elements (a,i,Ω,ω) can be calculated from (A,B,F,G), as we will explain below.

Being (x'_n, y'_n) the observed orbital position at t_n and (x_n, y_n) the theoretical position given by Eq. B.1, estimates of A,B,F,G can be obtained by minimizing the corresponding χ^2, defined as

$$\chi^2 = \sum_n \frac{(x_n - x'_n)^2}{\sigma^2_{x_n}} + \sum_n \frac{(y_n - y'_n)^2}{\sigma^2_{y_n}}, \tag{B.4}$$

where σ_{x_n} and σ_{y_n} the corresponding standard errors of each measurement.

Four linear equations follows to the derivative of χ^2 with respect to A,B,F,G (even more, two independent pairs of linear equations, since A,F only depends on x and B,G of y, so the problem have an analytical solution. Following the notation given in Lucy (2014), the estimates of the Thiele-Innes constants are

$$\begin{aligned} \hat{A} &= \frac{b_1 r_{11} - c_1 r_{12}}{\Delta_1} & \hat{F} &= \frac{-c_1 r_{11} + a_1 r_{12}}{\Delta_1} \\ \hat{B} &= \frac{b_2 r_{21} - c_2 r_{22}}{\Delta_2} & \hat{G} &= \frac{-c_2 r_{21} + a_2 r_{22}}{\Delta_2}, \end{aligned} \tag{B.5}$$

where

$$
\begin{aligned}
a_1 &= \sum_n \frac{X_n^2}{\sigma_{x_n}^2} \quad b_1 = \sum_n \frac{Y_n^2}{\sigma_{x_n}^2} \quad c_1 = \sum_n \frac{X_n Y_n}{\sigma_{x_n}^2} \quad \Delta_1 = a_1 b_1 - c_1^2 \\
a_2 &= \sum_n \frac{X_n^2}{\sigma_{y_n}^2} \quad b_2 = \sum_n \frac{Y_n^2}{\sigma_{y_n}^2} \quad c_2 = \sum_n \frac{X_n Y_n}{\sigma_{y_n}^2} \quad \Delta_2 = a_2 b_2 - c_2^2 \\
r_{11} &= \sum_n \frac{x'_n X_n}{\sigma_{x_n}^2} \quad r_{12} = \sum_n \frac{x'_n Y_n}{\sigma_{x_n}^2} \\
r_{21} &= \sum_n \frac{y'_n X_n}{\sigma_{y_n}^2} \quad r_{12} = \sum_n \frac{y'_n Y_n}{\sigma_{y_n}^2}.
\end{aligned}
\tag{B.6}
$$

Finally, to derive the orbital elements, we should invert Eqs. B.3. We have that

$$\omega + \Omega = \arctan\left(\frac{B-F}{A+G}\right) \tag{B.7}$$

and

$$\omega - \Omega = \arctan\left(\frac{-B-F}{A-G}\right). \tag{B.8}$$

Solving this pair of equations, we obtain ω and Ω. As a convention, if $\Omega < 0$, we set $\Omega = \Omega + \pi$ and $\omega = \omega + \pi$; if $\Omega > 0$, we set $\Omega = \Omega - \pi$ and $\omega = \omega - \pi$.

The rest of the orbital parameters, i and a, can be calculated unambiguously as follows

$$i = 2\arctan\left(\sqrt{\frac{A-G}{\cos\omega - \Omega} \cdot \frac{\cos\omega + \Omega}{A+G}}\right) \tag{B.9}$$

and

$$a = \frac{1}{2}\left(\frac{A+G}{\cos\omega + \Omega} + \frac{A-G}{\cos\omega - \Omega}\right). \tag{B.10}$$

The measurements (x'_n, y'_n) from which we derive the orbital elements above consisted in the relative position of both components of the binary, that is, direct measurements of the relative orbital motion. However, in our observations, the absolute position (i.e., with respect to an external quasar) of the individual components (or at least one of them, the primary) is known. These positions are sampling the (absolute) orbit of the primary coupled with its proper motion and parallax; the corresponding orbital parameters are determined through a least-square fit similar to that previously explained but, in these case, with theoretical positions defined by

$$\begin{aligned} x(t) &= x(t_0) + \mu_x(t - t_0) + \pi P_x + (AX(E) + FY(E)) \\ y(t) &= y(t_0) + \mu_y(t - t_0) + \pi P_y + (BX(E) + GY(E)), \end{aligned} \quad \text{(B.11)}$$

where where t_0 is the reference epoch, μ_x and μ_y the proper motions, π the parallax, and P_x and P_y the parallax factors. We notice that the reference position, the proper motion and the parallax behaves linearly in the least-squares analysis, leaving P, e, and T_0 as the only non-linear parameters.

References

Abbott, D. C., Bieging, J. H., & Churchwell, E. 1984, ApJ, 280, 671

Allard, F., Homeier, D., & Freytag, B. 2011, 16th Cambridge Workshop on Cool Stars, Stellar Systems, and the Sun, 448, 91

Azulay, R., Guirado, J. C., Marcaide, J. M., Martí-Vidal, I., & Arroyo-Torres, B. 2014, A&A, 561, A38

Azulay, R., Guirado, J. C., Marcaide, J. M., et al. 2015, A&A, 578, A16

Baraffe, I., Chabrier, G., Allard, F., & Hauschildt, P. H. 1998, A&A, 337, 403

Baraffe, I., Chabrier, G., Allard, F., & Hauschildt, P. H. 2002, A&A, 382, 563

Baraffe, I., Homeier, D., Allard, F., & Chabrier, G. 2015, A&A, 577, A42

Barenfeld, S. A., Bubar, E. J., Mamajek, E. E., & Young, P. A. 2013, ApJ, 766, 6

Barnes, J. R., Collier Cameron, A., Lister, T. A., Pointer, G. R., & Still, M. D. 2005, MNRAS, 356, 1501

Beasley, A. J., & Conway, J. E. 1995, Very Long Baseline Interferometry and the VLBA, 82, 327

Boccaletti, A., Chauvin, G., Baudoz, P., & Beuzit, J.-L. 2008, A&A, 482, 939

Boden, A. F., Torres, G., Sargent, A. I., et al. 2007, ApJ, 670, 1214

Bondi, M., Mantovani, F., Sherwood, W., Tzioumis, A., & Venturi, T. 1994, A&AS, 103, 365-373

Bowler, B. P., Liu, M. C., Shkolnik, E. L., et al. 2012, ApJ, 753, 142

Brott, I., & Hauschildt, P. H. 2005, The Three-Dimensional Universe with Gaia, 576, 565

Cagaš, P., & Pejcha, O. 2012, A&A, 544, L3

Campbell, R. 2004, European VLBI Network on New Developments in VLBI Science and Technology, 245

Canuto, V. M., & Mazzitelli, I. 1991, ApJ, 370, 295

Canuto, V. M., Goldman, I., & Mazzitelli, I. 1996, ApJ, 473, 550

Casse, J. L. 1999, NewAR, 43, 503

Castelli, F., & Kurucz, R. L. 2003, Modelling of Stellar Atmospheres, 210, A20

Chabrier, G., & Baraffe, I. 1997, A&A, 327, 1039

Chabrier, G., Baraffe, I., Allard, F., & Hauschildt, P. 2000, ApJ, 542, 464

Close, L. M., Lenzen, R., Guirado, J. C., et al. 2005, Nature, 433, 286

Close, L. M., Thatte, N., Nielsen, E. L., et al. 2007, ApJ, 665, 736

Cohen, M. H. 1973, IEEE Proceedings, 61, 1192

Cohen, M. H., Moffet, A. T., Schilizzi, R. T., et al. 1975, ApJ, 201, 249

D'Antona, F., & Mazzitelli, I. 1994, ApJS, 90, 467

D'Antona, F., & Mazzitelli, I. 1997, Mem. Soc. Astron. Italiana, 68, 807

de la Reza, R., Torres, C. A. O., Quast, G., Castilho, B. V., & Vieira, G. L. 1989, ApJ, 343, L61

Deller, A. T., Tingay, S. J., Bailes, M., & West, C. 2007, PASP, 119, 318

Delorme, P., Gagné, J., Malo, L., et al. 2012, A&A, 548, A26

Dodson, R., Rioja, M., Asaki, Y., et al. 2013, AJ, 145, 147

Dorren, J. D., & Guinan, E. F. 1994, ApJ, 428, 805

Dulk, G. A., & Marsh, K. A. 1982, ApJ, 259, 350

Dulk, G. A. 1985, ARA&A, 23, 169

Duquennoy, A., & Mayor, M. 1991, A&A, 248, 485

Dutrey, A., Guilloteau, S., & Simon, M. 2003, A&A, 402, 1003

Evans, T. M., Ireland, M. J., Kraus, A. L., et al. 2012, ApJ, 744, 120

Fabrycky, D., & Tremaine, S. 2007, ApJ, 669, 1298

Fekel, F. C. 1997, PASP, 109, 514

Ferguson, J. W., Alexander, D. R., Allard, F., et al. 2005, ApJ, 623, 585

Fomalont, E. B., & Kopeikin, S. M. 2003, ApJ, 598, 704

Freytag, B., Allard, F., Ludwig, H.-G., Homeier, D., & Steffen, M. 2010, A&A, 513, A19

Freytag, B., Steffen, M., Ludwig, H.-G., et al. 2012, Journal of Computational Physics, 231, 919

Gagné, J., Lafrenière, D., Doyon, R., Malo, L., & Artigau, É. 2014, ApJ, 783, 121

Galli, P. A. B., Teixeira, R., Ducourant, C., Bertout, C., & Benevides-Soares, P. 2012, A&A, 538, A23

Gálvez, M. C., Montes, D., Fernández-Figueroa, M. J., & López-Santiago, J. 2006, Ap&SS, 304, 59

Gauza, B., Béjar, V. J. S., Pérez-Garrido, A., et al. 2015, ApJ, 804, 96

Green, R. M. 1985, Cambridge and New York, Cambridge University Press, 1985, 533 p.

Gregorio-Hetem, J., Lepine, J. R. D., Quast, G. R., Torres, C. A. O., & de La Reza, R. 1992, AJ, 103, 549

Gudel, M., Schmitt, J. H. M. M., Bookbinder, J. A., & Fleming, T. A. 1993, ApJ, 415, 236

Guedel, M., Schmitt, J. H. M. M., Benz, A. O., & Elias, N. M., II 1995, A&A, 301, 201

Güdel, M. 2002, ARA&A, 40, 217

Ghez, A. M., Neugebauer, G., & Matthews, K. 1993, AJ, 106, 2005

Girart, J. M., Curiel, S., Rodríguez, L. F., et al. 2004, AJ, 127, 2969

Griffin, R. F. 1992, The Observatory, 112, 41

Guirado, J. C., Reynolds, J. E., Lestrade, J.-F., et al. 1997, ApJ, 490, 835

Guirado, J. C., Martí-Vidal, I., Marcaide, J. M., et al. 2006, A&A, 446, 733

Guirado, J. C., Marcaide, J. M., Martí-Vidal, I., et al. 2011, A&A, 533, A106

Guirado, J.C., Alberdi, A., Agudo, I. et al., 'SKA Astrometry' in The Spanish Square Kilometre Array White Book, 2015, edited by M.A. Perez-Torres, L. Verdes-Montenegro, J.C. Guirado et al., published by Sociedad Española de Astronomía.

Gustafsson, B., Edvardsson, B., Eriksson, K., et al. 2008, A&A, 486, 951

Hartigan, P., Strom, K. M., & Strom, S. E. 1994, ApJ, 427, 961

Hartkopf, W. I., McAlister, H. A., & Franz, O. G. 1989, AJ, 98, 1014

Hauschildt, P. H., Allard, F., & Baron, E. 1999, ApJ, 512, 377

Heiter, U., Kupka, F., van't Veer-Menneret, C., et al. 2002, A&A, 392, 619

Hillenbrand, L. A., & White, R. J. 2004, ApJ, 604, 741

Høg, E., Fabricius, C., Makarov, V. V., et al. 2000, A&A, 355, L27

Hormuth, F., Brandner, W., Hippler, S., Janson, M., & Henning, T. 2007, A&A, 463, 707

Iglesias, C. A., & Rogers, F. J. 1996, ApJ, 464, 943

Janson, M., Brandner, W., Lenzen, R., et al. 2007, A&A, 462, 615

Järvinen, S. P., Berdyugina, S. V., & Strassmeier, K. G. 2005, A&A, 440, 735

Jeffries, R. D., Byrne, P. B., Doyle, J. G., et al. 1994, MNRAS, 270, 153

Johnson, D. R. H., & Soderblom, D. R. 1987, AJ, 93, 864

Klein, K.-L. 1987, A&A, 183, 341

König, B., Guenther, E. W., Woitas, J., & Hatzes, A. P. 2005, A&A, 435, 215

Lafrenière, D., Doyon, R., Marois, C., et al. 2007, ApJ, 670, 1367

Leitherer, C., & Robert, C. 1991, ApJ, 377, 629

Lestrade, J.-F., Jones, D. L., Preston, R. A., et al. 1995, A&A, 304, 182

Lim, J., Nelson, G. J., Castro, C., Kilkenny, D., & van Wyk, F. 1992, ApJ, 388, L27

Lim, J. 1993, ApJ, 405, L33

Lim, J., White, S. M., Nelson, G. J., & Benz, A. O. 1994, ApJ, 430, 332

Lim, J., & White, S. M. 1995, ApJ, 453, 207

Lindegren, L., & Kovalevsky, J. 1995, A&A, 304, 189

Loinard, L., Torres, R. M., Mioduszewski, A. J., et al. 2007, ApJ, 671, 546

López-Santiago, J., Montes, D., Fernández-Figueroa, M. J., & Ramsey, L. W. 2003, A&A, 411, 489

López-Santiago, J., Montes, D., Crespo-Chacón, I., & Fernández-Figueroa, M. J. 2006, ApJ, 643, 1160

Lowrance, P. J., Becklin, E. E., Schneider, G., et al. 2005, AJ, 130, 1845

Lucy, L. B. 2014, A&A, 563, A126

Luhman, K. L., Stauffer, J. R., & Mamajek, E. E. 2005, ApJ, 628, L69

Makarov, V. V., & Urban, S. 2000, MNRAS, 317, 289

Makarov, V. V., & Eggleton, P. P. 2009, ApJ, 703, 1760

Malo, L., Doyon, R., Lafrenière, D., et al. 2013, ApJ, 762, 88

Mamajek, E. E. 2005, ApJ, 634, 1385

Mathieu, R. D., Baraffe, I., Simon, M., Stassun, K. G., & White, R. 2007, Protostars and Planets V, 411

Mazeh, T., & Shaham, J. 1979, A&A, 77, 145

McCarthy, K., & White, R. J. 2012, AJ, 143, 134

Melis, C., Reid, M. J., Mioduszewski, A. J., Stauffer, J. R., & Bower, G. C. 2013, Advancing the Physics of Cosmic Distances, 289, 60

Metchev, S. A., & Hillenbrand, L. A. 2004, ApJ, 617, 1330

Montalbán, J., D'Antona, F., & Mazzitelli, I. 2000, A&A, 360, 935

Montalbán, J., D'Antona, F., Kupka, F., & Heiter, U. 2004, A&A, 416, 1081

Montalbán, J., & D'Antona, F. 2006, MNRAS, 370, 1823

Montes, D., López-Santiago, J., Fernández-Figueroa, M. J., & Gálvez, M. C. 2001, A&A, 379, 976

Moran, J. M., & Dhawan, V. 1995, Very Long Baseline Interferometry and the VLBA, 82, 161

Murphy, T., Sadler, E. M., Ekers, R. D., et al. 2010, MNRAS, 402, 2403

Nakajima, T., & Morino, J.-I. 2012, AJ, 143, 2

Naud, M.-E., Artigau, É., Malo, L., et al. 2014, ApJ, 787, 5

Nielsen, E. L., Close, L. M., Guirado, J. C., et al. 2005, Astronomische Nachrichten, 326, 1033

Ortega, V. G., Jilinski, E., de La Reza, R., & Bazzanella, B. 2007, MNRAS, 377, 441

Palla, F., & Stahler, S. W. 1999, ApJ, 525, 772

Pandey, J. C., Singh, K. P., Sagar, R., & Drake, S. A. 2002, Journal of Astrophysics and Astronomy, 23, 9

Pandey, J. C., Singh, K. P., Drake, S. A., & Sagar, R. 2005, AJ, 130, 1231

Perryman, M. A. C., Lindegren, L., Kovalevsky, J., et al. 1997, A&A, 323, 49

Piluso, N., Lanza, A. F., Pagano, I., Lanzafame, A. C., & Donati, J.-F. 2008, MNRAS, 387, 237

Pizzolato, N., Maggio, A., Micela, G., Sciortino, S., & Ventura, P. 2003, A&A, 397, 147

Plavchan, P., Werner, M. W., Chen, C. H., et al. 2009, ApJ, 698, 1068

Plez, B. 1992, A&AS, 94, 527

Pols, O. R., Tout, C. A., Eggleton, P. P., & Han, Z. 1995, MNRAS, 274, 964

Press, W. H., Teukolsky, S. A., Vetterling, W. T., & Flannery, B. P. 1992, Cambridge: University Press, |c1992, 2nd ed.

Ramaty, R. 1969, ApJ, 158, 753

Rioja, M., Dodson, R., Porcas, R. W., et al. 2009, 8th International e-VLBI Workshop, 14

Rodríguez, L. F., Curiel, S., Cantó, J., et al. 2003, ApJ, 583, 330

Rybicki, G. B., & Lightman, A. P. 1979, New York, Wiley-Interscience, 1979. 393 p.,

Sadler, E. M., Ricci, R., Ekers, R. D., et al. 2006, MNRAS, 371, 898

Saumon, D., Chabrier, G., & van Horn, H. M. 1995, ApJS, 99, 713

Schlieder, J. E., Lépine, S., & Simon, M. 2010, AJ, 140, 119

Schlieder, J. E., Lépine, S., & Simon, M. 2012, AJ, 143, 80

Schwab, F. R., & Cotton, W. D. 1983, AJ, 88, 688

Shepherd, M. C., Pearson, T. J., & Taylor, G. B. 1994, BAAS, 26, 987

Siess, L., Dufour, E., & Forestini, M. 2000, A&A, 358, 593

Siess, L. 2001, From Darkness to Light: Origin and Evolution of Young Stellar Clusters, 243, 581

Simon, M., Dutrey, A., & Guilloteau, S. 2000, ApJ, 545, 1034

Skrutskie, M. F., Cutri, R. M., Stiening, R., et al. 2006, AJ, 131, 1163

Song, I., Zuckerman, B., & Bessell, M. S. 2003, ApJ, 599, 342

Stassun, K. G., Mathieu, R. D., Vaz, L. P. R., Stroud, N., & Vrba, F. J. 2004, ApJS, 151, 357

Steffen, A. T., Mathieu, R. D., Lattanzi, M. G., et al. 2001, AJ, 122, 997

Stone, J. M., Skemer, A. J., Kratter, K. M., et al. 2016, ApJL, 818, L12

Strassmeier, K. G., Hall, D. S., Zeilik, M., et al. 1988, A&AS, 72, 291

Swenson, F. J., Faulkner, J., Rogers, F. J., & Iglesias, C. A. 1994, ApJ, 425, 286

Takakura, T., & Scalise, E. 1970, Solar Phys., 11, 434

Taylor, G. B., Carilli, C. L., & Perley, R. A. 1999, Synthesis Imaging in Radio Astronomy II, 180

Thatte, N., Abuter, R., Tecza, M., et al. 2007, MNRAS, 378, 1229

Tognelli, E., Prada Moroni, P. G., & Degl'Innocenti, S. 2011, A&A, 533, A109

Tognelli, E., Degl'Innocenti, S., & Prada Moroni, P. G. 2012, A&A, 548, A41

Torres, C. A. O., da Silva, L., Quast, G. R., de la Reza, R., & Jilinski, E. 2000, AJ, 120, 1410

Torres, C. A. O., Quast, G. R., Melo, C. H. F., & Sterzik, M. F. 2008, Handbook of Star Forming Regions, Volume II, 757

Torres, R. M., Loinard, L., Mioduszewski, A. J., et al. 2012, ApJ, 747, 18

Tremblay, P.-E., Gianninas, A., Kilic, M., et al. 2015, ApJ, 809, 148

van Langevelde, H. J., Phillips, C., & Evn/Jive Staff 2002, Cosmic Masers: From Proto-Stars to Black Holes, 206, 497

van Leeuwen, F. 2007, A&A, 474, 653

Ventura, P., Zeppieri, A., Mazzitelli, I., & D'Antona, F. 1998, A&A, 331, 1011

Wahhaj, Z., Liu, M. C., Biller, B. A., et al. 2011, ApJ, 729, 139

Walker, R. C. 1989, Synthesis Imaging in Radio Astronomy, 6, 355

Wendker, H. J. 1995, A&AS, 109, 177

Wichmann, R., Schmitt, J. H. M. M., & Hubrig, S. 2003, A&A, 399, 983

Wolter, U., Czesla, S., Fuhrmeister, B., et al. 2014, A&A, 570, A95

Wright, J. T., & Howard, A. W. 2009, ApJS, 182, 205-215

Zuckerman, B., & Webb, R. A. 2000, ApJ, 535, 959

Zuckerman, B., Song, I., Bessell, M. S., & Webb, R. A. 2001, ApJ, 562, L87

Zuckerman, B., & Song, I. 2004, ARA&A, 42, 685

Zuckerman, B., Song, I., & Bessell, M. S. 2004, ApJ, 613, L65